CENTRO DE INVESTIGACION Y DE
ESTUDIOS AVANZADOS DEL IPN

Estudio de la reacción

$$pCu \longrightarrow \mu^+\mu^- X$$

con protones de 800 $GeV/$c

TESIS

que para obtener el grado académico de

Doctor en Ciencias

p r e s e n t a

Gerardo Moreno López

México, D. F.

1989

a

Elisa

Abstract

Two measurements of dimuon production in proton-Copper collisions are presented and the results are interpreted within the context of the parton model and Quantum Chromodynamics (QCD). The dimuon mass spectrum observed in this experiment covers the region from 6.5 to 18 GeV. The first three Upsilon states (Υ , Υ' , Υ'') are clearly seen and no other resonances are detected. The p_t and x_F distributions of the Upsilons are compared with those of the continuum, and the scaling form of the continuum cross-section is compared with other experiments. A brief description of dimuon production in hadronic reactions is given in Chapter 1. The experimental apparatus is described in Chapter 2 and the data acquisition system in Chapter 3. Data analysis and results are presented in Chapters 4 and 5, respectively.

Contents

List of Figures

List of Tables

Acknowledgements

I arrived at Fermilab on a cold January morning. Little did I know what it was really going to be like working on E605. I knew what I was going to do, but knowing and doing are two different things. E605 turned out to be one of the most significant experiences in my life. Sometimes my worst enemy... othertimes my friend, companion, and only link to life. Yes, these years were tough, but they were also bearable and even enjoyable.

All the work that went into the experiment involved so many people that to mention them all at this moment seems impossible. Nevertheless, I thank all those persons that at one time or another collaborated in the experiment.

I am very grateful to Leon Lederman for giving me the opportunity to join the E605 collaboration under very unusual circumstances. I wish to express my most profound respect and admiration for Charles Brown, my thesis advisor, from whom I learned the many details involved in the experiment.

I specially thank Kam Biu Luk and Bruce Straub for showing me the way through the analysis program. I would like to thank Mark Adams, Carlos Hojvat, David Jaffe, Daniel Kaplan, Antonio Morelos, and John Rutherfoord for many useful discussions.

I also want to thank my friends and teachers in Mexico, specially, Augusto García, José Luis Lucio, Miguel Angel Pérez, and Arnulfo Zepeda, from whom I have received encouragement and constant support ever since I became a student at CINVESTAV.

Finally, my thesis is dedicated to my dear friend Elisa Herrera for the many things she did for me while I was at Fermilab.

Chapter 1

Introduction

This Chapter describes the dominant processes for hadroproduction of massive muon pairs at energies relevant to our experiment, $\sqrt{s} = 38.8\,GeV$. These are:

1. Quark-antiquark annihilation into a virtual photon state which couples to a $\mu^+\mu^-$ pair, as described by the Drell-Yan model; and

2. The production of resonant states which can decay into a lepton pair.

1.1 The Drell-Yan Process

Ever since the famous Rutherford experiment[1] showed that atoms are made of a nucleus surrounded by electrons, scattering experiments have been a valuable tool in understanding the internal structure of matter.

The study of lepton pairs produced in hadronic collisions,

$$h_A + h_B \longrightarrow l^+l^- + X \ ,$$

can be used to determine the structure of hadrons, in a way complementary to inelastic lepton-nucleon scattering, $l + N \rightarrow l' + X$. After the first such experiment[2] showed a steeply falling dimuon mass spectrum, Drell and Yan[3] suggested that the underlying process might be the production of a lepton pair by the electromagnetic annihilation of a parton-antiparton pair, as shown in Figure 1.1. This description is now usually known as 'the naive Drell-Yan model' because of its simplicity, and the hadronic partons are identified with the quarks of QCD.

---

[1] E. Rutherford, Phil. Mag. **11** (1906) 166; **12** (1906) 134.
[2] J. H. Christenson *et al.*, Phys. Rev. Lett. **25** (1970) 1523.
[3] S. D. Drell and T-M. Yan, Phys. Rev. Lett. **25** (1970) 316.
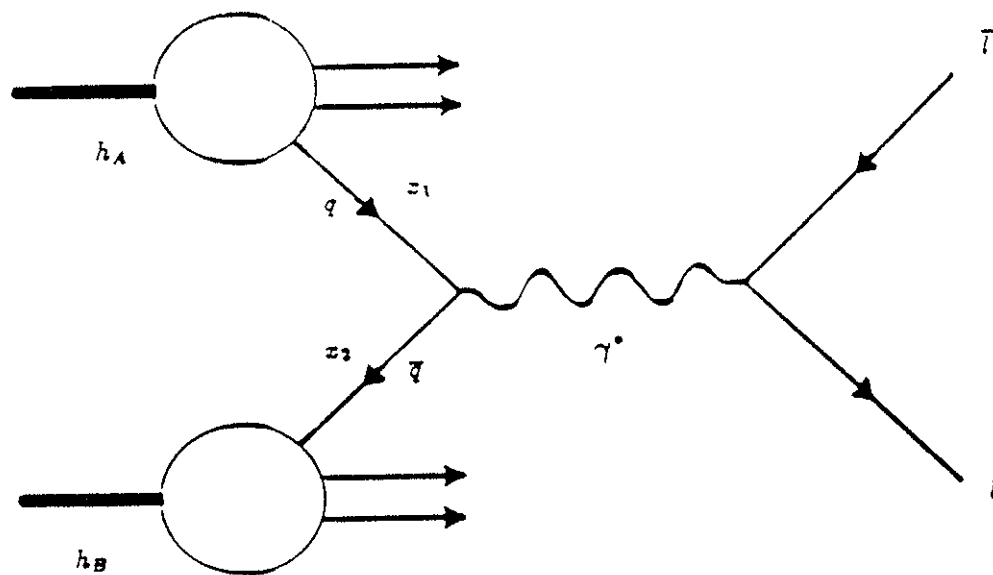
Figure 1.1: The Drell-Yan process. A quark with momentum fraction x_1 in hadron A annihilates with an antiquark of momentum fraction x_2 in hadron B. The resulting virtual photon of mass $m = \sqrt{x_1 x_2 s}$ then decays into a lepton pair.

Drell and Yan suggested that in the hadronic production of dimuons the electromagnetic annihilation of quarks might dominate. They considered the quarks as instantaneously free during the interaction, in order to neglect their binding effects, and then treated the dynamics of the collision as free fermions annihilating into a lepton pair. These two requirements can be understood in terms of the asymptotic freedom of QCD and the Heisenberg uncertainty principle. Asymptotic freedom[4] is based on the behavior of the color force at short distances, this color force decreases as the separation goes to zero. Since short distances also imply, by the uncertainty principle, high energies and small time scales, the point-like electromagnetic annihilation might dominate the strong interaction if the dilepton mass is larger than typical hadron masses.

1.1.1 Kinematic Variables

Dilepton production is usually described in the center of mass (CM) frame of the colliding hadrons. Since the momenta $\vec{p}_+^{\,lab}$ and $\vec{p}_-^{\,lab}$ of the outgoing leptons are measured in the 'laboratory system', a Lorentz transformation to the CM frame will change them to $\vec{p}_+$ and $\vec{p}_-$. In terms of these quantities the invariant mass m and momentum $\vec{p}$ of the dilepton are

$$m = 2\sqrt{p_+ p_-}\,\sin\!\left(\frac{\theta_{open}}{2}\right)$$

$$\vec{p} = \vec{p}_+ + \vec{p}_-$$

where θ_{open} is the opening angle between the leptons and their masses have been neglected. The dilepton energy is then $E = \sqrt{m^2 + p^2}$. The momentum is usually written in cylindrical coordinates as (p_t, ϕ, p_l), where p_l is along the direction z of the incoming hadrons, and p_t forms an angle ϕ with respect to the arbitrary x axis. Two more variables are needed to complete the description. These are the angles θ_{CS} and ϕ_{CS} that specify the l^+ direction in the dilepton rest frame. The Collins-Soper[5] convention (CS) is used to define the axis in the dilepton rest frame with respect to which θ_{CS} and ϕ_{CS} are measured: In general, the momenta $\vec{p}_A^{\,CS}$ and $\vec{p}_B^{\,CS}$ of the colliding hadrons in the CS frame are not collinear, the z axis of that frame is chosen such

[4]H. D. Politzer, Phys. Rev. Lett **30** (1973) 1346; F. Wilczek, *ibid*, 1343.

[5]J. C. Collins and D. E. Soper, Phys. Rev. **D16** (1977) 2219.

that it bisects the angle between $\vec{p}_A^{CS}$ and $-\vec{p}_B^{CS}$. Then, θ_{CS} is defined as the angle between the l^+ and this z axis; and ϕ_{CS} is measured with respect to the direction away from the transverse component of the vector sum $\vec{p}_A^{CS} + \vec{p}_B^{CS}$.

There are two alternate longitudinal variables commonly used to describe the dynamics of the process. These are the longitudinal scaling variables, the Feynman x variable x_F and the rapidity variable y,

$$ x_F = \frac{2\,p_l}{\sqrt{s}} \quad \text{and} \quad y = \frac{1}{2} \ln\left(\frac{E + p_l}{E - p_l}\right), $$

where $\sqrt{s}$ is the center of mass energy of the hadron-hadron system. It is also a custom to define the 'scaled mass' $\sqrt{\tau}$ as $\sqrt{\tau} = m/\sqrt{s}$.

1.1.2 Dynamics

As the elementary process for Drell-Yan production is $q\bar{q} \rightarrow \gamma^* \rightarrow l\bar{l}$, it is then formally equivalent to the well known reaction $e^+e^- \rightarrow \gamma^* \rightarrow \mu^+\mu^-$. Thus the unpolarized cross section of the subprocess $q_i\bar{q}_i \rightarrow \gamma^* \rightarrow l\bar{l}$ is given by

$$ \frac{d\hat{\sigma}_i}{d\Omega} = \frac{\alpha^2 e_i^2}{4m^2}(1 + \cos^2\theta), $$

where α is the fine structure constant, e_i is the charge of the quark of flavor i, m is the photon energy, and θ is the angle between the incoming quark and the outgoing lepton. Integrating over the lepton angles gives

$$ \hat{\sigma}_i = \frac{4\pi\alpha^2 e_i^2}{3m^2} . $$

To relate $\hat{\sigma}_i$ to the hadron-hadron cross section $\sigma(AB \rightarrow l\bar{l}X)$, the quark distribution functions inside the hadrons must be known. The Drell-Yan formulation assumes that these distributions are the same as those measured in deep-inelastic scattering experiments. If $q_i^A(x_1)\,dx_1$ $[\bar{q}_i^B(x_2)\,dx_2]$ is the probability of finding a quark [antiquark] i carrying a momentum fraction x_1 $[x_2]$ of the parent hadron A $[B]$, then

$$ d^2\sigma_i = \hat{\sigma}_i\,q_i^A(x_1)\,\bar{q}_i^B(x_2)\,dx_1 dx_2 . $$

The quark may originate in hadron B and the antiquark in hadron A, thus a $\bar{q}_i^A\,q_i^B$ term should be added to the cross section. Furthermore, as each quark

type can contribute, a sum over flavors must be performed. Finally, since only quark-antiquark pairs of the same color can annihilate, the average over colors reduces the cross section by a factor of 3. Therefore the hadron-hadron cross section for dilepton production is given by

$$\frac{d^2\sigma}{dx_1\,dx_2} = \left(\frac{4\pi\alpha^2}{9m^2}\right) \sum_i e_i^2 \left[q_i^A(x_1)\bar{q}_i^B(x_2) + \bar{q}_i^A(x_1)q_i^B(x_2)\right] .$$

If p_t is small with respect to m and p_l, and the hadron masses are neglected with respect to $\sqrt{s}$, x_1 and x_2 are related to τ and x_F through

$$x_1 \simeq \frac{1}{2}(\sqrt{4\tau + x_F^2} + x_F) \text{ and } x_2 \simeq \frac{1}{2}(\sqrt{4\tau + x_F^2} - x_F) ,$$

or in terms of y and τ

$$x_1 \simeq \sqrt{\tau}e^y \text{ and } x_2 \simeq \sqrt{\tau}e^{-y} .$$

The cross section can then be written in terms of dimensionless quantities. The expressions

$$m^3 \frac{d^2\sigma}{dm\,dx_F} = \left(\frac{4\pi\alpha^2}{9}\right) \left(\frac{x_1 x_2}{x_1 + x_2}\right) \sum_i e_i^2 \left[q_i^A(x_1)\bar{q}_i^B(x_2) + \bar{q}_i^A(x_1)q_i^B(x_2)\right]$$

and

$$s \frac{d^2\sigma}{d\sqrt{\tau}\,dy} = \left(\frac{4\pi\alpha^2}{9}\right) \sum_i e_i^2 \left[q_i^A(x_1)\bar{q}_i^B(x_2) + \bar{q}_i^A(x_1)q_i^B(x_2)\right]$$

are known as *scaling* forms of the cross section.

1.1.3 Experimental Tests and Improvements

The assumptions and predictions of the model have been compared with experimental results[6]. Some important consequences of the model are:

Electromagnetic Effect. The Drell-Yan process is of electromagnetic origin and exactly calculable within the quark-parton model for hadrons using structure functions measured in deep-inelastic scattering. (The measured cross-section typically lies above the predicted value by a factor of about 2, which is known as the K-factor.)

---

[6]For a review, see I. R. Kenyon, Rep. Prog. Phys. **45** (1982) 1261; J. P. Rutherfoord, Proceedings of the 1985 International Symposium on Lepton and Photon Interactions at High Energies, Kyoto, Japan, 1985.

Nuclear Dependence Since the cross-section per nucleon is the incoherent sum of the cross-section of the component quarks and antiquarks, it is expected that the cross-section per nucleus is proportional to A, the atomic number. Experiments using different targets have confirmed this expectation at about the $\pm 10\%$ level.

Angular Distribution. Because the process involves massless unpolarized fermions at high energies, the angular distribution of the leptons should be $1 + \cos^2\theta$, where θ is the angle between the outgoing lepton and the incoming quark in the dilepton CM frame. This assumption has been experimentally confirmed within the uncertainties of defining the incoming quark-antiquark momenta in the dilepton center-of-mass system.

p_t **Distribution.** The model neglects completely any transverse momentum in the process, which it assumes can only arise from the intrinsic transverse momentum, k_t, of the annihilating quarks. One might expect p_t to be small and not change rapidly with either $\sqrt{s}$ or the total energy of the annihilation. Assuming exponentially falling k_t distributions, with mean value $\sim 0.35\,GeV$, as observed at low energies, the mean p_t would be[6] $\langle p_t \rangle = \sqrt{2} \times \langle k_t \rangle \simeq 0.5\,GeV$. The experimental evidence shows that $\langle p_t \rangle$ is larger than $1\,GeV$, approximately independent of m, and grows linearly with $\sqrt{s}$.

Scaling. The model predicts that, for a given x_F (or y), the cross-section in the scaling form should depend on $\sqrt{\tau}$ only. This means that experiments performed at different CM energies can be compared directly. The scaling property has been confirmed using proton as well as pion beams on different targets.

Even though the K-factor is not unity and $\langle p_t \rangle$ is larger than expected, the model has received much attention because of its simplicity and striking predictions. Moreover, QCD calculations have shown that order α_s corrections reproduce the K-factor and the rising of $\langle p_t \rangle$ with $\sqrt{s}$. Theorists now agree on how to compute order α_s QCD contributions[7] and experiments can test the more complete predictions. One such contribution is that the parton distribution functions not only depend on the fractional momentum but also

---

[7]For a review, see G. Altarelli, Phys. Rep. **81C** (1982) 1.

depend on the momentum transfer. This effect becomes important at high $\sqrt{\tau}$ in the Drell-Yan Model, and is thus called a 'scale violation effect' as the scaling form of the cross-section will vary with $\sqrt{s}$ at fixed $\sqrt{\tau}$.

In this thesis, the results of our experiment at $\sqrt{s} = 38.8\,GeV$ will be compared with previous experiments at different energies.

1.2 The Upsilon Family

The upsilon, Υ , was discovered in 1977 by the CFS (Columbia-Fermilab-Stony Brook) group in an experiment observing dimuons produced by $400\,GeV$ protons on a Platinum target. The first data[8] gave evidence for a resonance, called the Υ , at $m \sim 9.5\,GeV$. More data indicated additional resonances, the Υ' at $10\,GeV$ and possibly the Υ'' at $10.4\,GeV$. Further experiments at e^+e^- colliders confirmed the three Υ states, followed by the discovery of more states at other energies. The Υ family is now interpreted as a bound state of the heavy b quark and its antiquark partner $\bar{b}$, having the same quantum numbers as the photon, $J^{PC} = 1^{--}$.

The Υ family together with the J/Ψ family form the 'positronium atoms' of QCD, called quarkonia. Potential models have been used to describe the $q\bar{q}$ binding. For example, Figure 1.2 shows the predictions of one such model[9] for the $b\bar{b}$ system. The states which have been observed are indicated with solid lines, the remaining ones with dashed lines. Most of the Υ spectroscopy[10] has come from e^+e^- annihilation experiments, where the virtual photon in the annihilation couples to the quarkonium system (Figure 1.3a).

Different production mechanisms[11] are expected to dominate in hadronic reactions. In this case, the lowest order QCD cross-sections are initiated by gluons and light quarks. To order α_s^2, only the gluon fusion process, depicted in Figure 1.3b, contributes and populates the low p_t region with a mean p_t determined by the primordial transverse motion of the gluons. To order α_s^3, there are more contributions (Figures 1.3c-h) in which a gluon or a quark recoils against the heavy resonance, thus leading to a large transverse

---

[8]S. W. Herb *et al.*, Phys. Rev. Lett. **39** (1977) 252.

[9]W. Buchmüller, Phys. Lett **112B** (1982) 479.

[10]For a review on Υ spectroscopy, see W. Buchmüller and S. Cooper, MIT Technical Report MIT-LNS-159 of March 1987.

[11]R. Baier and R. Rückl, Z. Phys. **C19** (1983) 251.
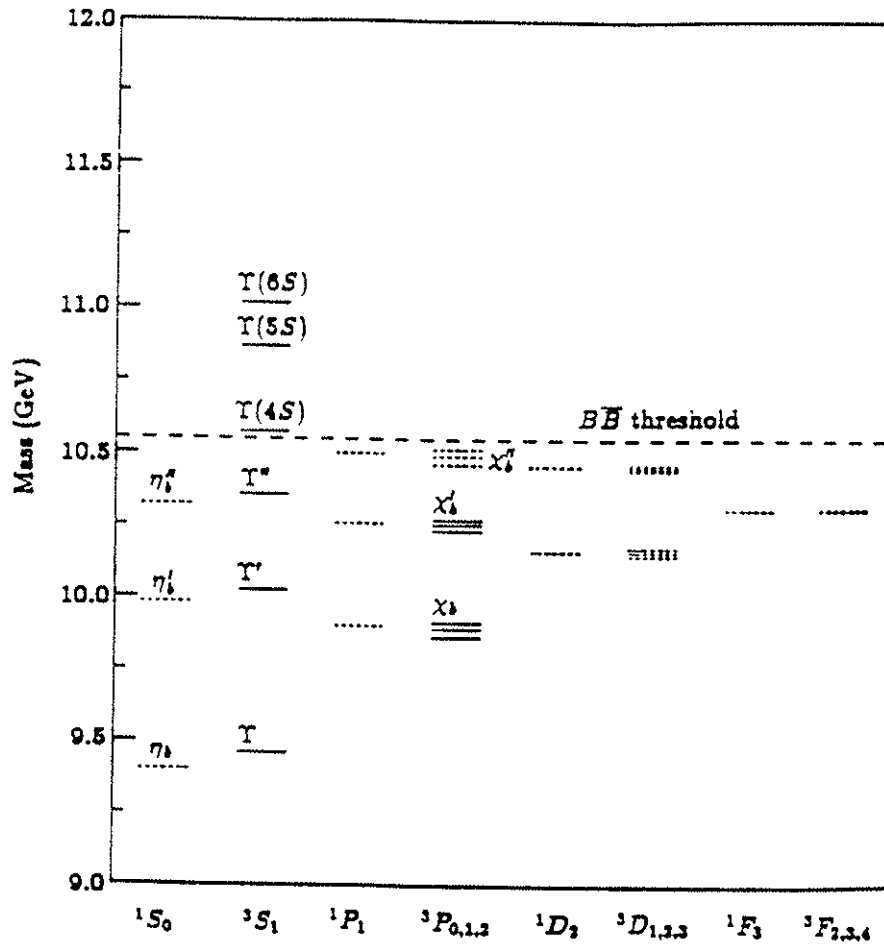
Figure 1.2: Predicted bottomonium spectrum. The solid lines indicate states that have been observed. The threshold for producing open bottom states (B$\bar{\text{B}}$) is shown as a long-dashed line.
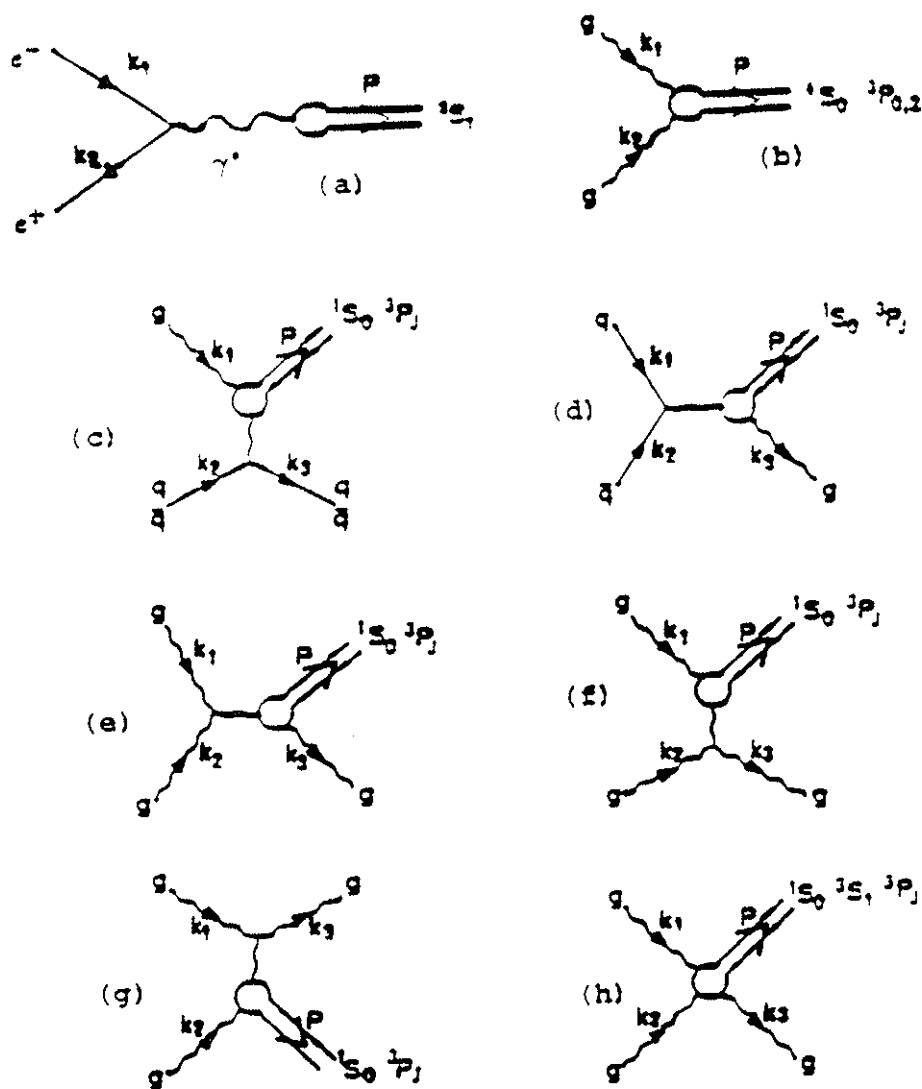
Figure 1.3: Quarkonium production. a) e^+e^- annihilation. b) gg scattering to $O(\alpha_s^2)$. c) gq or g$\bar{q}$ scattering. d) q$\bar{q}$ annihilation.

momenta. It should be noted that diagram 1.3h provides the only direct Υ (denoted $^3S_1$) production. The other diagrams imply a preference for χ_b (^3P_J) production. Thus, it might be expected that in hadronic reactions, Υ production is realized through radiative decays of the χ_b states (for example, the branching ratio[12] of $\chi_b(9895)$ to $\gamma\,\Upsilon(9460)$ is 47%).

Thus, in the measurements described in the following pages, the prediction is that the continuum of Drell-Yan dimuon production depends on the quark distributions in hadrons while the production of Upsilon resonant states could depend on a different gluonic mechanism. Therefore, the difference in the measured physical distributions of the dimuons from the Drell-Yan continuum and the Upsilon resonances may be a direct measure of the differences in the underlying quark-antiquark and gluon distributions. In this thesis, it will be shown that the observed distributions are indeed different for Upsilon and Drell-Yan events.

---

[12]Particle Data Group, Phys. Lett. **170B** (1986) 228.

Chapter 2

Experimental Setup

The goals of the experiment and the means to achieve them are discussed in the first Section. A description of the FNAL proton beam is found in Section 2. Targets are described in Section 3. Analysis Magnets are presented in Section 4. Finally, electronic detectors are described in Section 5.

2.1 Apparatus Overview

Fermilab experiment E605 was originally designed to perform a precision measurement of the production of high p_t single hadrons and to measure the 10–20 GeV mass spectrum of dileptons and dihadrons in high energy proton-nucleon collisions[1]. To accomplish these goals, E605 required a high incident beam flux as well as good momentum resolution and background rejection. A high incident flux is needed because the cross-sections for these processes are very small. Good momentum resolution is important because most physical quantities are obtained from momentum measurements. The main problem was in reducing the tremendous background of particles coming from the interaction, since no tracking device can handle the charged particle fluxes near the target. To solve this problem, a strong open-aperture magnet was used to focus high momentum charged particles onto the downstream detector and to sweep away the low momentum particles. A beam dump, inside the magnet, intercepted the non-interacted beam and the huge flux of low p_t particles. Since the first magnet reduced the downstream counting rates, momentum measurements could then be made with a second

---

[1] FNAL-605, in Major Detectors in Elementary Particle Physics, Particle Data Group, LBL-91 Supplement, revised (1985).
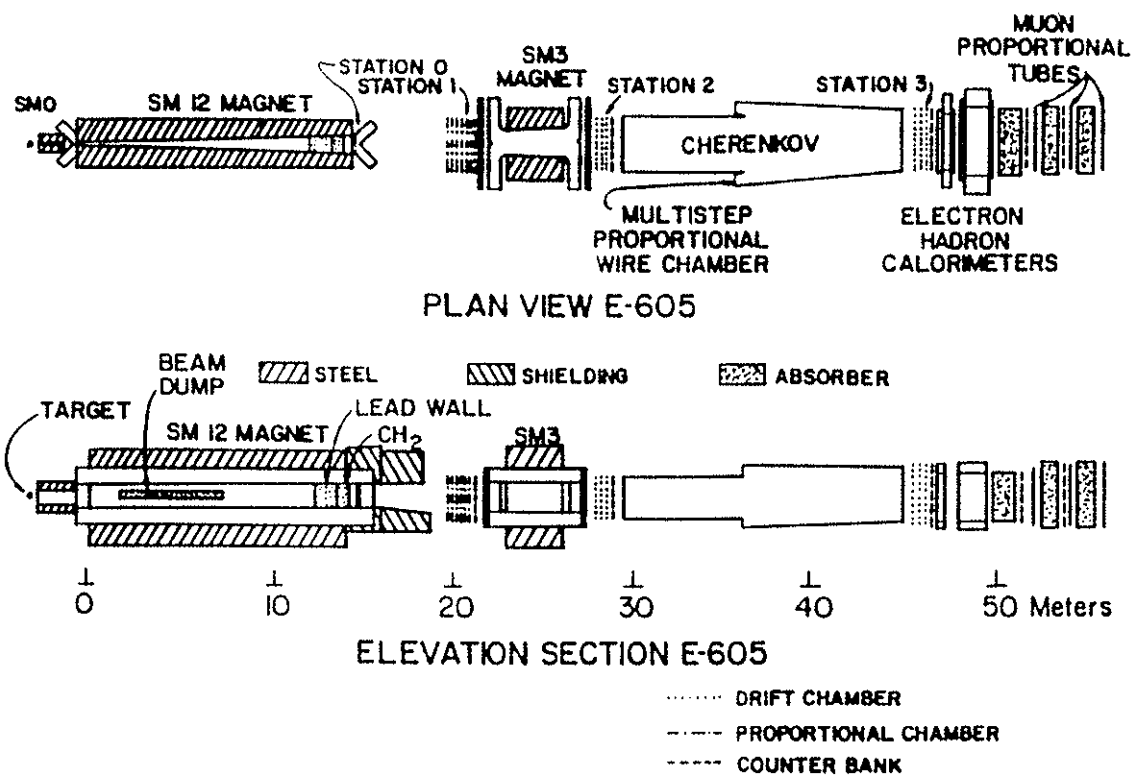
Figure 2.1: The E605 spectrometer.

open-aperture magnet and tracking chambers. Particle identification was done with the aid of a Čerenkov counter, hadron and electron calorimeters, and muon counters.

E605 concentrated on detecting only dimuons during the 1985 run. A careful Monte Carlo study[2] had shown that a thick absorber blocking the aperture would allow the apparatus to be exposed at even higher incident intensities and still maintain excellent mass resolution. Thus, a lead wall was placed at the downstream end of the first magnet, followed by a wire chamber to allow a precise determination of momentum using the downstream magnet only. With this modification , the apparatus was transformed into a closed-aperture focusing magnetic spectrometer for muon pairs. It covered approximately one steradian near 90° in the proton-nucleon center of mass system.

The apparatus thus consisted of (as shown in Figure 2.1): a huge closed-aperture magnet, a beam dump, a lead wall, a large open-aperture magnet, 25 planes of wire chambers, 7 planes of scintillation counters, and various radiation shielding (the Čerenkov and calorimeters remained in place but were not used for this present measurement). The experiment was located in the Meson East Experimental Area of the Fermi National Accelerator Laboratory, in Batavia, Illinois, U.S.A.

2.2   Beam and Monitors

2.2.1   Beam

The proton beam at Fermilab involves several production stages. First, molecular hydrogen (H_2) is transformed into negative hydrogen ions (H^-) in the ion source. Accelerating H^- and stripping the electrons off during injection into a circular accelerator increases beam intensity. The ion source feeds a $750\,KeV$ Cockcroft-Walton accelerator. Next, the ion beam passes through a 'prebuncher' where it is modulated according to the Linac rf to prevent particle loses when it enters the $200\,MeV$ Linac. At the end of the Linac is a 'chopper' which selects the almost-equal-momentum part of the beam, and a 'debuncher' that eliminates the previous rf structure.

---

[2]J. P. Rutherfoord, Resolution Predictions for E605 Pb Wall Running, E605 Internal Report of Oct. 6, 1984.

The beam is then injected into an 8 GeV proton-synchrotron (Booster) using the Multiturn Charge Exchange Injection System[3], which provides a very reliable way of increasing the beam intensity. At the injection point, negative ions coming from the Linac are brought together with protons already in the Booster. They then pass through a thin carbon foil, where the negative ions lose the unwanted electrons, leaving only protons of the same momentum and very close spatial position. This is done between one to ten times until the Booster synchrotron has enough protons to begin the acceleration cycle.

When the Booster has accelerated the protons to 8 GeV/c, they are extracted and injected into another proton-synchrotron (Main Ring). It has a 6.28 Km circumference and 13 'Booster batches' are needed to fill it up. Since the acceleration rf frequency is 53 MHz, there are 1113 rf buckets[4] available in the Main Ring. Once it is full, it accelerates the beam to 150 GeV/c. The final stage of acceleration occurs in a third proton-synchrotron (Tevatron), where they acquire the peak energy of 800 GeV. The Main Ring and Tevatron accelerators share the same tunnel. The former one contains conventional magnets (*i.e.* Fe magnets with Cu coils), while the later one uses Ni_3Ti superconducting magnets.

Slow extraction is accomplished by resonantly exciting the beam until it crosses an electrostatic extraction septum. This is adjusted to give approximately constant intensity in the extracted beam for about 20 sec. This period of time is known as the 'spill'. The period between spills is 40 sec. Once the beam exits the extraction septum, it is split into three beam lines: *Meson*, *Proton* and *Neutrino* lines. Each beam is further divided supplying beam to many experiments simultaneously. From a typical 10^{13} protons per spill in the accelerator, E605 received 2×10^{12}, which is about 2000 protons per bunch or 10^{11} protons/sec average intensity.

2.2.2 Monitors

A movable segmented wire ion chamber (SWIC) monitored the beam transverse position near the target during beam tuning. The SWIC had wires

---

[3] C. Hojvat *et al.*, IEEE Trans. Nucl. Sci. **Ns 26** (1979) 3149.

[4] The regions of stable orbits in phase space are known as 'rf buckets'. Particles that travel in each rf bucket are said to form a 'bunch'. There are about 10^{10} protons per bunch, under normal operation conditions, in the Fermilab accelerator.

spaced .5 mm in the vertical direction and 2 mm in the horizontal direction. For most of the data taking, the SWIC was removed from the beam because its presence was a source of background events.

Beam intensity per spill was measured with a secondary emission monitor (SEM) located approximately 100 m upstream of the target. δ-rays produced by the beam in the monitor are collected by a charge integrator. The integrator has a digital output (counter) of 1 pulse per 3 picocoulombs of collected charge. To calibrate the counter, a copper foil was put into the beam and the number of SEM counts was recorded. Later, the decay-rate of ^{24}Na in the foil was measured. Knowing the cross-section for the ^{24}Na production by protons in Copper[5] and the time elapsed between calibration and decay-rate measurements, the number of protons which produce 1 SEM count can be obtained. The calibration gave[6] 1 SEM $= (.80 \pm .04) \times 10^8$ protons.

A four-fold scintillation telescope (AMON), viewing the target at 90° in the lab, was used to monitor the number of protons hitting the target (targeting efficiency). Assuming that AMON is operated below saturation, it will respond linearly to the number of protons interacting in the target. Let $P(x,y)\,dx\,dy$ be the fraction of beam protons that cross perpendicularly an area $dx\,dy$ at (x,y). Let SEM be a measure of beam protons and AMON be the number of AMON counts for a given SEM, then

$$\text{SEM} \times \int_{A_\perp} P(x,y)\,dx\,dy = K \times \text{AMON} ,$$

where $A_\perp$ is the target area perpendicular to the beam, and K is a constant that depends only on target properties. By definition, $\int_{A_\perp} P(x,y)\,dx\,dy$ gives the targeting efficiency. The constant K can also be obtained by moving the target across the beam in increments of exactly one target thickness and measuring AMON/SEM at each position i. Therefore the targeting efficiency at position i is given by

$$\int_{A_{\perp i}} P(x,y)\,dx\,dy = \frac{\left(\frac{\text{AMON}}{\text{SEM}}\right)_i}{\sum_{\text{all } j}\left(\frac{\text{AMON}}{\text{SEM}}\right)_j} .$$

Figure 2.2 shows the targeting efficiency *versus* the relative beam-to-target vertical position for the targets used in the experiment.

---

[5]The value of this cross-section currently used at Fermilab is $3.90 \pm .11\,mbarn$, as reported by S. I. Baker *et al.*, Nucl. Instr. & Meth. **222** (1984) 467.

[6]C. N. Brown, Summary of SEM calibrations, E605 Internal Report of Oct. 16, 1985.
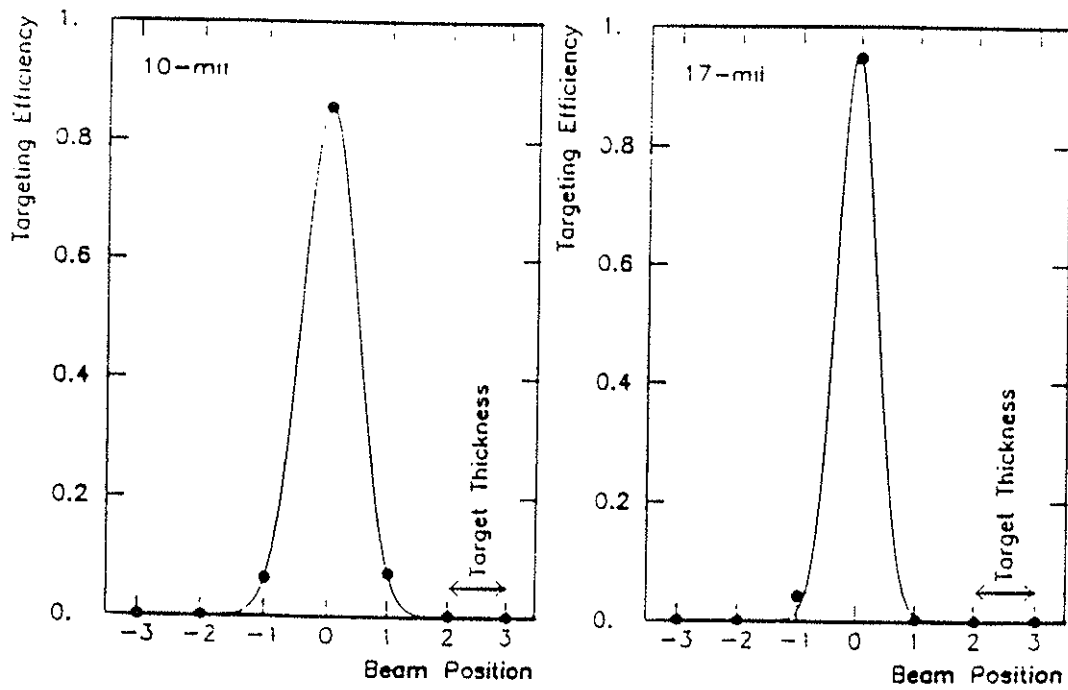
Figure 2.2: Beam profile. The vertical shape of the beam as seen with different targets, normalized to give the targeting efficiency as explained in Section 2.2.2. The continuous line is a gaussian fit to the data points.

2.3 Targets

Table 2.1 lists some properties of the two targets (referred to as the 10-*mil* and 17-*mil* targets) used in the experiment. Both targets were thin sheets of copper with a vertical thickness given in the table, and a horizontal width of 3.8 *cm*. Since the targets were vertically slightly thinner (see Figure 2.2) than the beam, the vertical interaction position was very well defined. On the other hand, the horizontal size of the interaction region was determined by the width of the beam[7] (5 *mm*). The targets were mounted 2.54 *cm*

	10-*mil*	17-*mil*
Thickness (*mm*)	0.254	0.432
Length (*mm*)	50.8	38.1
Width (*mm*)	38.0	38.0
Density (g/cm^3)	8.96	8.96
A	63.54	63.54
Z	29	29
λ_I (g/cm^2)	134.9	134.9

Table 2.1: Size and properties[8] of the targets.

apart vertically on a movable holder in a vacuum target box. A precision motor-driven platform supported the target holder such that the vertical and horizontal position of the target could be remotely controlled. By moving the target across the beam vertically and reading out the number of AMON and SEM counts, we could monitor the targeting efficiency as a function of the target position. One spill was needed to record AMON and SEM at each point. Thus, the targeting efficiency would resemble the vertical beam profile if 1) the beam was stable from one spill to another, and 2) the target thickness was much smaller than the beam size. It is under these conditions that we call Figure 2.2, the beam profile. Note that the beam profile as seen with the 17 *mil* target does not quite satisfy condition 2.

---

[7]D. E. Jaffe, Ph. D. thesis, SUNY at Stony Brook, 1987.

[8]The nuclear absorption length is defined as $\lambda_I = A/(N_0 \times \sigma_I)$, where σ_I is the the nuclear inelastic cross-section and N_0 is Avogadro's number.

2.4   Magnets

Three dipole magnets (called SM0, SM12, and SM3 in order of increasing distance from the target) were used in our experiment. SM0 was attached to the target box, but it was never turned on during the 1985 run. The SM12 and SM3 magnetic fields were oriented horizontally but in opposite directions. SM12 was used to focus high p_t particles while SM3 defocused them and was used to measure their momenta.

2.4.1   SM12

The upstream face of the SM12 yoke was chosen to be the $z = 0$ plane in the E605 reference frame: we defined the z axis along the beam direction, the y axis to point upwards, and the x axis horizontally consistent with a right-handed system. The x and y coordinates were measured from the beam line. Thus, the nominal target position was $(0.\,m,\ 0.\,m,\ -3.3\,m)$.

The outside dimensions of SM12[9] were $14.4\,m$ long, $2.7\,m$ wide, and $5.2\,m$ high, while the aperture was $.93\,m$ wide and $1.22\,m$ high. It was made of $1200\,tons$ of iron blocks and two conventional water-cooled aluminum coils. It was run at two different current settings, giving an average kick of $7.5\,GeV/c$ when run at $4000\,Amps$ and $5.6\,GeV/c$ at $2750\,Amps$.

Seven iron poleface modules were put inside SM12 to increase the field intensity, the magnetic volume tapered horizontally from $15.24\,cm$ at the entrance to $93.0\,cm$ at the exit. Each module held lead and tungsten absorbers on its upper and lower surfaces to protect the coils from radiation damage and absorb low energy tertiary particles. The second and third upstream modules supported the beam dump that covered the horizontal aperture from $y = -15.2\,cm$ to $y = +15.2\,cm$. The beam dump was a $4.27\,m$ long copper block, slightly tapered from a vertical thickness of $y = \pm12.7\,cm$ at $z = 1.73\,m$ to $y = \pm15.2\,cm$ at $z = 2.64\,m$, and then remaining at a constant thickness of $y = \pm15.2\,cm$ until it ended at $z = 6.00\,m$. It was followed by another $1.53\,m$ of lead and borated polyethylene absorbers also covering $y = \pm15.2\,cm$.

At $z = 12.71\,m$, there was a $1.22\,m$ thick lead wall that fully blocked the magnet aperture, absorbing all hadrons, photons and electrons. A borated polyethylene wall, $0.61\,m$ thick, downstream of the lead wall absorbed neutrons generated in the lead.

---

[9]R. W. Fast *et al.*, IEEE Trans. Magnetics **MAG-17** (1981) 1903.

2.4.2 SM3

SM3 was a second conventional analyzing magnet, with water-cooled aluminum coils. It was $3.23\,m$ long, $5.40\,m$ high, and $2.59\,m$ wide, located between two Stations of detectors used to measure the muons' momenta. An excitation current of $4200\,Amps$ gave an average kick of $.91\,GeV/c$. Its magnetic volume was also tapered such that the horizontal aperture was $1.35\,m$ at the upstream end and $1.50\,m$ at the downstream one, while the vertical aperture was $1.68\,m$. A polyethylene bag containing helium was used in the gap of the magnet to reduce multiple scattering. Two iron plates (with aperture cut-outs) $5\,cm$ thick were mounted on both ends to reduce the fringe field at the nearby detectors.

2.4.3 Field Measurement

The usual procedure to determine the momentum of a charged particle is by measuring the deflection of its trajectory when it traverses a magnetic field. The angle of deflection is a function of the momentum and the magnetic field, hence the momentum can be inferred if the magnetic field is known. As an example, consider the case when a particle of charge q passes through a region R where there exists a magnetic field $\vec{B}$ in the x direction. In a small angle approximation, the momentum P in the y-z plane is given by

$$P = q\,\frac{P_{Tkick}}{\theta_2 - \theta_1}$$

where $P_{Tkick} = \int_R B_x dz$ (called the kick of the magnet) and θ_1 and θ_2 are the trajectory initial and final angles (in the y-z plane) respectively measured from the z direction.

The magnetic field of each magnet was measured[10] with a device called 'ZIPTRACK' in the spring of 1982. The ZIPTRACK was a long aluminum beam on which a belt-driven cart supported three orthogonal pickup coils. As the coils moved through the magnetic field, the induced current (proportional to the change in flux) was measured at regularly spaced points. The magnitude of the field was checked using a nuclear magnetic resonance probe in its central region and a hall probe in the fringe field. Field maps were produced[11] by interpolating and regularizing the data. It was expected to

---

[10]J. Rothberg, E605 Internal Reports of March 26 and May 13, 1982.

[11]R. Gray, J. Rothberg, and J. Rutherfoord, E605 Internal Report of March 8, 1983.

get at least 1 % accuracy on the field integral and .2 % accuracy on the shape of the major field component. The position and width of the Upsilon resonances observed in this experiment confirm these expectations.

2.5 Tracking Detectors[12]

The principle of detection of charged particles is their electromagnetic interaction with matter. Ionization in gases is used in wire chambers. Luminescence in crystals and plastics is the basis for scintillation counters.

Several wire chambers and scintillation counters were grouped together to form a detector Station. Five Stations provided tracking information along the spectrometer. They were numbered from 0 to 4 according to their z position. Station 0 was attached to the downstream end of the SM12 yoke. Stations 1 and 2 were just upstream and downstream of SM3. A Čerenkov counter was located between Stations 2 and 3. Calorimeters were located behind Station 3, followed by a hadron absorber wall and Station 4. Table 2.2 lists the detectors and some specifications. Dimensions are to be read *horizontal* × *vertical* sizes.

2.5.1 Hodoscopes

Hodoscope planes were included at each Station, except for Station 0. They were made of horizontally segmented (X) and vertically segmented (Y) plastic scintillator. Each plane was divided into two halves: *left* (YL) and *right* (YR) for the y view; and *up* (XU) and *down* (XD) for the x view. The number of counters is displayed in Table 2.2, where the notation is X × Y. The size in parenthesis corresponds to the end counters only.

The hodoscopes had the fastest time response of the various electronic detectors. They were used to eliminate out-of-time chamber hits, form 'roads' of probable tracks, and, most important of all, define the fast trigger logic, which is described in the next chapter.

2.5.2 Wire Chambers

Four types of wire chambers were used in our experiment: proportional tube counters (PT), proportional drift tubes (PDT), multiwire proportional chambers (MWPC), and drift chambers (DC). A proportional counter consists of a long hollow conductor, filled with gas, and a very thin wire strung along its center line. Wire and conductor are kept insulated and a

---

[12]An excellent textbook on detectors is W. R. Leo, *Techniques for Nuclear and Particle Physics Experiments*, Springer-Verlag, Berlin-Heidelberg, 1987.

high voltage is applied such that the wire becomes the anode. If a charged particle traverses the gas, ionization can occur along its path. Electrons coming from the ionization will drift toward the anode wire, and, near the wire, will gain enough energy to produce more ionization, creating an avalanche very close to the wire. MWPC's and DC's are based on the same principle. The structures of these chambers are very similar. They consist of a set of thin, parallel, and equally spaced wires sandwiched between two cathode planes. They differ in wire spacing and in wire size. DC wire spacing is much larger than that of MWPC. While in a MWPC all wires are anode wires; in a DC, anode wires are alternated with 'field-shaping' wires. Because of the larger wire spacing in a DC, field-shaping wires are used to increase the electric field in the region far from the anode wires.

A high-rate PDT chamber measured the y position at Station 0. It had 4 planes of cylindrical aluminum tubes of $1\,cm$ diameter. It was the key to improve the measurement of the vertical position of the possible scattering point in the lead wall. Once the momentum of a particle had been determined with the aid of Stations 1, 2, and 3, Station 0 information was added to give a more precise measurement of its momentum.

The central part of the tracking used the information from Stations 1, 2, and 3. The y, u, and v coordinates of the particle trajectories were measured at each Station, where u and v were oriented at angles of $\pm \arctan 1/4$ with respect to the y axis. Station 1 consisted of six MWPC's of $2\,mm$ wire spacing. Stations 2 and 3 each had six drift chambers — one pair for each coordinate. Each chamber pair had one plane shifted by half a cell with respect to the other one. The cell size was approximately $10\,mm$ in Station 2 and $20\,mm$ in Station 3. The dimensions and measured resolution of the chambers are presented in Table 2.2.

Three planes of proportional tubes (PTY1,PTX, and PTY2), measuring either the x or y coordinate, were used at Station 4 to help in muon recognition. A $81\,cm$ thick concrete wall, a $92\,cm$ thick zinc wall, and a $10\,cm$ thick lead plate, placed just downstream the calorimeter, shielded against hadron shower leakage. Behind it, Y4 and PTY1 were followed by $92\,cm$ of concrete absorber, X4 and PTX, another $92\,cm$ of concrete, and finally, PTY2.

Detector name	type	z position (m)	Dimensions x(m)×y(m)	Channels	Cell width (mm)	Resolution μm
Y0A	PDT	14.69	1.00×1.22	120	10.16	406
Y0B	PDT	14.70	1.00×1.22	120	10.16	305
Y0C	PDT	14.71	1.00×1.22	120	10.16	356
Y0D	PDT	14.72	1.00×1.22	120	10.16	356
U1A	MWPC	18.97	1.28×1.51	896	1.97	635
Y1A	MWPC	19.22	1.28×1.50	736	2.03	635
V1A	MWPC	19.48	1.28×1.51	896	1.97	635
U1B	MWPC	19.73	1.28×1.51	896	1.97	635
Y1B	MWPC	19.98	1.28×1.50	736	2.03	635
V1B	MWPC	20.24	1.28×1.51	896	1.97	635
Y1	hodo	20.47	1.22×1.52	2×12	127(127)	
X1	hodo	20.51	1.22×1.52	12×2	102(102)	
U2	DC	27.52	1.68×1.83	208	9.86	254
U2'	DC	27.58	1.68×1.83	208	9.86	254
Y2	DC	27.77	1.68×1.79	176	10.16	254
Y2'	DC	27.82	1.68×1.79	176	10.16	254
V2	DC	28.02	1.68×1.83	208	9.86	254
V2'	DC	28.08	1.68×1.83	208	9.86	254
Y2	hodo	28.32	1.63×1.73	2×17	102(102)	
C	Čerenkov					
U3	DC	45.76	2.69×2.43	144	20.21	229
U3'	DC	45.83	2.69×2.43	144	20.21	229
Y3	DC	46.01	2.69×2.33	112	20.83	229
Y3'	DC	46.09	2.69×2.33	112	20.83	229
V3	DC	46.26	2.69×2.43	144	20.21	229
V3'	DC	46.33	2.69×2.43	144	20.21	229
X3	hodo	46.66	2.64×2.34	13×2	220(110)	
Y3	hodo	46.92	2.64×2.34	2×13	178(191)	
E	cal					
H	cal					
Y4	hodo	51.70	2.95×2.54	14×2	178(203)	
PTY1	PT	51.86	2.97×3.05	120	25.40	
X4	hodo	54.13	3.20×2.90	14×2	203(181)	
PTX	PT	54.25	3.43×3.09	135	25.40	
PTY2	PT	55.90	3.59×3.64	143	25.42	

Table 2.2: Detector characteristics.

Chapter 3

Data Acquisition

The Data Acquisition System consisted of a Triggering System, a Readout System, a cache MegaMemory, and the On-line Computer, as shown in Figure 3.1. Relevant elements of the dimuon trigger are discussed in the first Sections. The Readout System is described in Section 3.7. Finally, a summary of collected data is presented in Section 3.8.

3.1 Triggering Philosophy

With 2000 protons/bucket incident on our $.25\lambda_I$ Cu target, about 500 interactions of potential interest were produced every $19\,nsec$[1]. Only very rarely, did those 500 interactions include an opposite-sign muon pair (dimuon) that could completely traverse the apparatus. Most of the time, uninteresting particles, resulting from tertiary lower energy collisions at the absorbers and magnet walls or muons from the beam dump, traversed the detectors. Hence, the task of the electronic trigger was to reject as many as possible of the background charged particles while retaining as many as possible of the dimuon events which came through the active area of the spectrometer. Three levels of triggers were employed to decide whether or not a set of tracks in the apparatus was interesting enough to be recorded. The first level triggers (Fast Triggers) made their decision with a time resolution of less than $19\,nsec$, rejecting tracks associated with different rf buckets. The first level triggers reduced the rate to a level where the second level triggers (DC Logic) and third level trigger (Trigger Processor) could make a more detailed decision, based on tracking information, with a small deadtime. Block

---

[1]The accelerator rf bucket of extracted protons is less than $2\,nsec$ long every $18.8\,nsec$ ($1\,nsec = 10^{-9}\,seconds$).

23
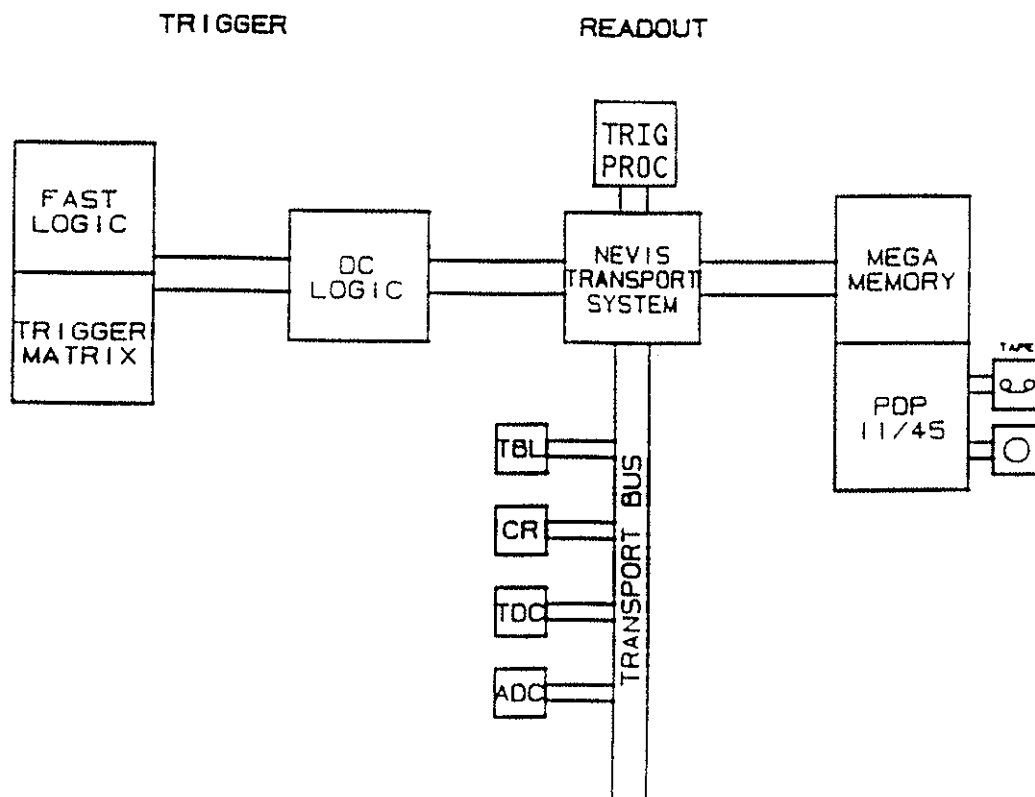
Figure 3.1: Block diagram of the Data Acquisition System

diagrams of the Fast Triggers and the DC Logic are shown in Figures 3.2 and 3.3 respectively.

A trigger cycle began by synchronizing the hodoscope signals to the accelerator rf signal for input to the Fast Triggers. Outputs from the Fast Triggers were used to strobe the DC Logic. The Trigger Processor made the final trigger decision when triggered by a DC Logic output. If the event passed the trigger chain, hits in all the detectors and trigger registers were stored in a fast memory. The data from all events in one spill was then written on tape between accelerator spills.

Besides the main dimuon trigger, several other triggers were also implemented to monitor detector efficiencies as well as the trigger efficiencies themselves, since no trigger element was required by all of them.

3.2 Fast Triggers

Scintillation counters were used in the Fast Triggers, Trigger Matrix, and multiplicity units because of their fast response time (rise-time typically on the order of 1 $nsec$). Signals from the phototubes attached to the scintillation counters were brought into the counting room via coax cables to LeCroy 4416 16-channel discriminators. Each discriminator output was synchronized to the accelerator rf signal by the University of Washington pulse stretchers[2] and then fanned out to several places: 1) Each channel was sent via a delay cable to a coincidence register card (CR) to later record which counter fired. 2) Each channel was sent to Trigger Matrix modules or multiplicity units. 3) Each half-bank of counters (L=left and R=right halves of each bank[3]) was sent to a hodoscope terminator module, where the logical OR of the half bank was performed. This OR signal was then fed into LeCroy 365AL Quad Logic Units which generated the output signals $\frac{3}{4}\mu_L$ and $\frac{3}{4}\mu_R$ from the coincidence of any three out of the four (L or R) bank counters: X1, Y2, Y4, and X4. Finally, the signals $\frac{3}{4}\mu_L$ and $\frac{3}{4}\mu_R$ were further combined to produce the Fast Triggers[4]

---

[2] R. Gray and J. P. Rutherfoord, Nucl. Instr. & Meth. **A244** (1986) 440.

[3] Note that in the convention employed in Section 2.5.1, Y counters were called *left* and *right* while X counters were called *up* and *down*. In this chapter, the phrase *the left (right) half of an X bank* is meant to say *the up and down counters on the left (right) side of an X bank*.

[4] Logical operations AND and OR are denoted by $\odot$ and $\oplus$ respectively
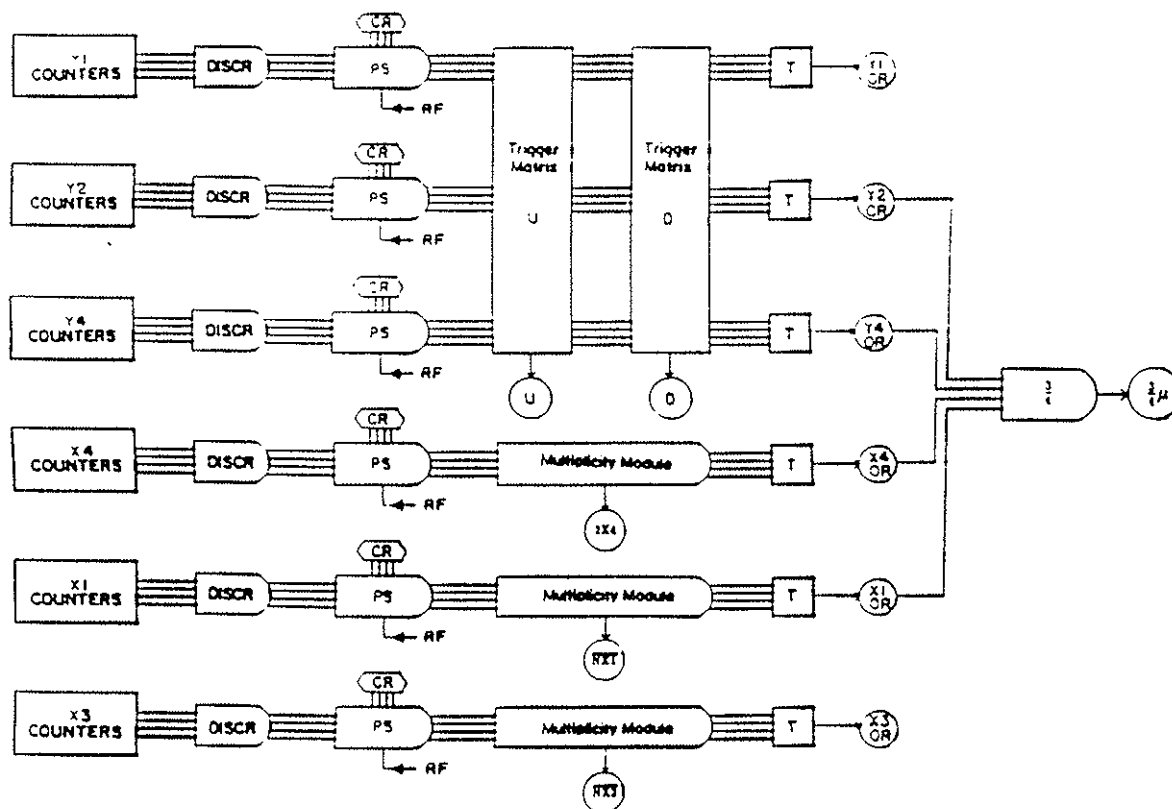
Figure 3.2: Fast Trigger Logic

$$\tfrac{3}{4}\mu_\mathrm{L} \odot \tfrac{3}{4}\mu_\mathrm{R} \; ,$$

$$\tfrac{3}{4}\mu_\mathrm{L}/64\mathrm{K} \; , \text{ and}$$

$$\tfrac{3}{4}\mu_\mathrm{R}/64\mathrm{K} \; ,$$

where the symbol /64K stands for *prescaled by 65536*, *i.e.*, only one out of 2^{16} signals was considered as a trigger. The prescaling factor was very high because the requirement $\tfrac{3}{4}\mu$ (L or R), corresponding to an apparent muon on either side of the the apparatus, was very easily fulfilled. The Fast Triggers were then logically ORed by the Trigger Fan In (TFI) module to start the DC Logic cycle. Basically, $\tfrac{3}{4}\mu_\mathrm{L} \odot \tfrac{3}{4}\mu_\mathrm{R}$ generated the 'go' signal for the DC Logic to look for target dimuons, since it roughly defined two muons traversing the apparatus.

Toward the end of the data taking, a new fast trigger for neutral lepton search was added and the single triggers $\tfrac{3}{4}\mu_\mathrm{L}/64\mathrm{K}$ and $\tfrac{3}{4}\mu_\mathrm{R}/64\mathrm{K}$ were removed from the fast logic.

3.3   Trigger Matrix

The Trigger Matrix was a fast lookup table[5] incorporated in ECL random access memory (RAM) chips. The Trigger Matrix was configured to do a 3-fold coincidence on preset hodoscope counter combinations of Y1, Y2 and Y4. These combinations were identified using a Monte Carlo apparatus simulation, enabling only combinations consistent with a muon track coming from the target. The allowed combinations were then written into a disk file which was loaded into the RAMs by the On-line program before data taking. During data taking, the input address to each RAM was formed from the signals of 4 counters from one hodoscope bank, and 4 counters from a second bank. The output of each RAM (*i.e.*, the stored value) corresponded to the allowed set of counters in the third bank which completed correct matrix combinations. These output signals were then logically ANDed with the actual set of hodoscope hits in the third bank to form the matrix output.

Four large groups of hodoscope combinations (called μ-matrices: μ_UL, μ_UR, μ_DL, and μ_DR) crudely defined muons that went above (U), or below (D), the beam dump and to the left (L), or right (R), side of the apparatus. Finally, the logic signals

---

[5] H. D. Glass, Ph. D. Thesis, SUNY at Stony Brook, 1985.

$$\mu_U = \mu_{UL} \oplus \mu_{UR} , \qquad \mu_D = \mu_{DL} \oplus \mu_{DR} ,$$

$$\mu_L = \mu_{UL} \oplus \mu_{DL} , \text{ and } \mu_R = \mu_{UR} \oplus \mu_{DR}$$

were formed and sent to the DC Logic modules for processing.

3.4 Multiplicity Vetoes

To keep trigger rates low and deadtime small without losing good dimuon events, several multiplicity requirements were used in the DC Logic. A current sum of counter signals in each X hodoscope plane was fed into a LeCroy discriminator to form one multiplicity veto signal per plane, as follows:

Two veto signals, called $\overline{NX1}$ and $\overline{NX3}$, were generated if more than 10 counters had fired in the X1 hodoscope plane, or more than 9 had fired in the X3 hodoscope plane. These vetoes were based on the assumption that good dimuon events should not fire many counters and were checked by comparing multiplicity distributions for dimuon events with those of background events.

A signal called 2X4 required at least two hits in X4, one of them being outside the two central counters. Signals from the middle counters were merged before they arrived at the multiplicity unit to force at least one muon to be at an angle $\theta_x \gtrsim 4\,mrad$. The reason for this was that most of the uninteresting muons (low p_t and/or beamdump origin muons) were concentrated at small angles. To aid in this rejection of the low p_t muons from the beam dump, upper and lower Y4 hodoscope counters were shortened to remove the region $\theta_x < 3mrad$ and $|y| > 62cm$.

3.5 DC Logic

The DC Logic[6] (Figure 3.3) was a flexible general-purpose triggering system capable of generating up to 16 different triggers. Input signals and latched, so that further processing could be done with DC levels without worrying about timing.

Inputs to the DC Logic came to two places: the Trigger Generator Input (TGI) module and the DC Logic Bus. The TGI module received the TFI signal from the Fast Triggers while the DC Logic Bus contained signals

---

[6]Y. B. Hsiung, Ph. D. Thesis, Columbia University, 1986

from the Trigger Matrices and multiplicity modules. The purpose of the TGI module was to generate a start signal for the DC Logic and strobe the DC Logic Bus, and also to generate fast gates for MWPC CR's and Station 2 drift chamber TDC's. Once the DC Logic Bus had been strobed, trigger modules plugged into the Logic Bus could form any logical combination (pin selectable) of the Logic Bus levels. If a selected trigger module criterion was satisfied, it sent a signal to the Trigger Generator Output (TGO) module which, in turn, sent out gates for the numerous TDC's, CR's, and ADC's; latched the hodoscope counter hits; blocked the reset pulse to hold data in MWPC CR's and Station 2 TDC's; and strobed the trigger bit latches. In this way, all the information was available to the Trigger Processor for the final trigger decision. If the event was accepted by the processor, the readout process took place and the TGO module received a system busy (SB) signal to prevent it from generating additional TGO's during readout. Nevertheless, the DC Logic continued to cycle, keeping a tally of the number of triggers missed during readout, to monitor the readout deadtime.

The DC Logic was used to implement

1. our main data acquisition trigger, SINK:

$$\text{SINK} = \mu_\text{L} \odot \mu_\text{R} \odot \mu_\text{U} \odot \mu_\text{D} \odot 2\text{X4} \odot \overline{\text{NX1}} \odot \overline{\text{NX3}} \ ,$$

2. and four study triggers:

(a) $\mu_\text{LR}/\text{PS} = (\mu_\text{L} \odot \mu_\text{R} \odot 2\text{X4})/128$

(b) $\frac{3}{4}\mu_\text{LR}/\text{PS} = (\frac{3}{4}\mu_\text{L} \odot \frac{3}{4}\mu_\text{R})/16\text{K}$

(c) $\frac{3}{4}\mu_\text{L}/\text{PS} = (\frac{3}{4}\mu_\text{L}/64\text{K})/8$

(d) $\frac{3}{4}\mu_\text{R}/\text{PS} = (\frac{3}{4}\mu_\text{R}/64\text{K})/8$

In other words, SINK required, at least, two opposite-sign, left-right, low background multiplicity, high p_t muons. The study triggers were prescaled by factors ranging from 8 to 16384, so that they represented less than 25% of the total number of triggers. The trigger μ_LR/PS was used to monitor hodoscope and chamber efficiencies, as well as the Trigger Matrix efficiencies by constructing software versions of the μ matrices and comparing them with the DC Logic trigger bit results. The trigger μ_LR/PS was used to measure the dimuon efficiencies of the Trigger Processor and of the multiplicity vetoes required by SINK.
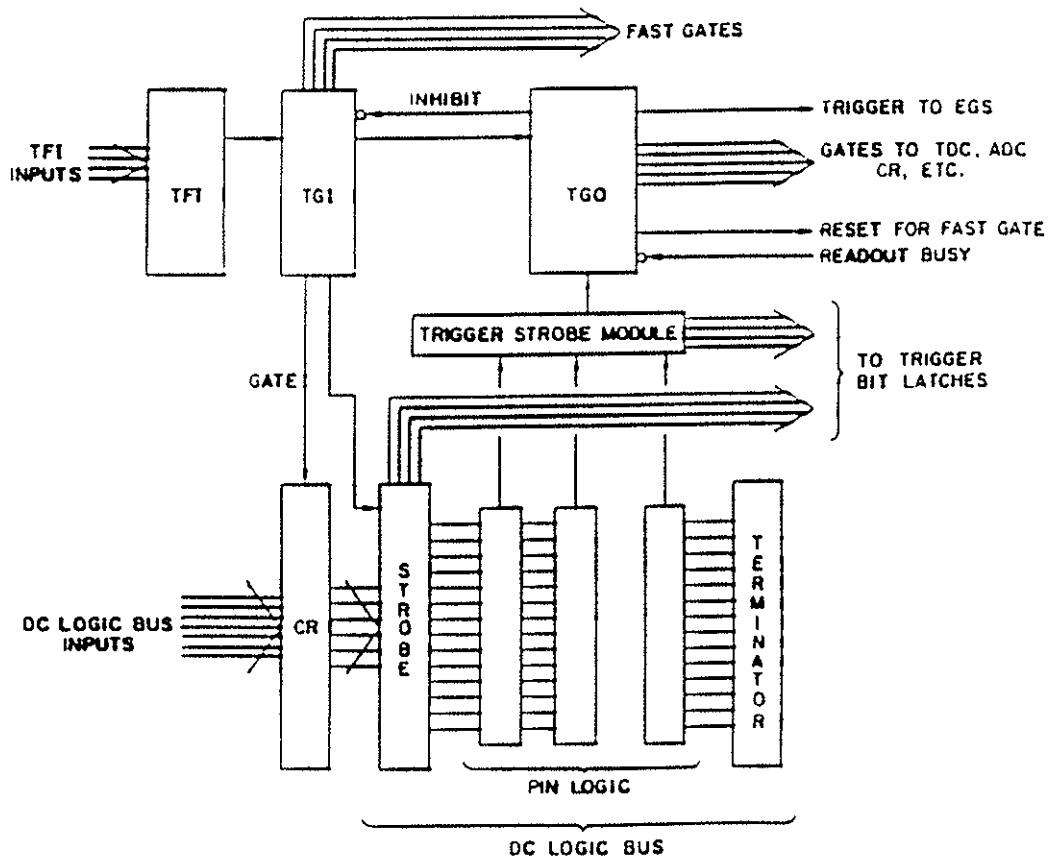
Figure 3.3: DC Logic

3.6 Trigger Processor

The Trigger Processor[7] was a flexible, parallel pipelined, event processor. It used hit information from eight chambers (Y1A, Y1B, Y2, Y2', Y3, Y3', PTY1, and PTY2,) to find tracks in the Y-Z plane (the plane of the magnetic deflection). For each track found, the y-component of momentum at the target (p_y) was calculated, and a pseudo-mass for the event was approximated by the sum of the absolute values of the most positive and most negative values of p_y.

The Trigger Processor used only wire numbers and ignored drift times, except to cut out hits whose drift times were too small (hits from previous rf buckets). To further decrease the sensitivity to out-of-time hits and reduce the number of track hypotheses, chamber hit lists from Stations 2 and 3 were masked with hodoscope hit lists before hypothesis generation, eliminating many of the out-of-time chamber hits.

The trackfinding algorithm formed all possible hypothetical tracks, connecting a hit in Station 2 and a hit in Station 3. These were then projected back to Station 1, demanding a hit in Y1A or Y1B consistent with a track originated in the target. All hypothetical tracks satisfying this requirement were then projected to the proportional tubes, where hits were required in both PTY1 and PTY2 for most of the run. (From time to time throughout the run, PTY1 showed signs of inefficiency because of gas flow problems. During those occasions, the requirement of hits in both proportional tubes was relaxed to a hit in at least one of them.)

The final decision whether to accept or reject the event depended on the trigger type. All study triggers were accepted by the processor, while for SINK triggers, the pseudo-mass value was compared to programmable thresholds in order to accept or reject the event. The pseudo-mass threshold was set slightly below the mass threshold of the spectrometer acceptance. Events below the pseudo-mass threshold were prescaled by a factor of 64, forming a second type of prescaled event used to study the Trigger Processor threshold.

If the event was accepted, the list of tracks found, their corresponding p_y's, and the pseudo-mass were available to the Readout System. The processor then triggered the Event Generator Source (EGS) module in the Readout System to start the readout process.

---

[7] Y. B. Hsiung et al., Nucl. Instr. & Meth. **A245** (1986) 338.

3.7 Readout System

The Nevis Transport System[8] formed the communication highway between the different pieces of the readout system, namely, the data-storage units, the Trigger Processor, the readout buffer, and the on-line PDP-11/45 computer.

For each EGS signal, Transport read out all non-zero data words from each element (trigger bits, hodoscope hits, chamber hits, processor output), storing the information into the temporary buffer, called the MegaMemory. The MegaMemory[9] had 4 Mega bytes of memory and could store up to 4095 events per spill. At the end of the spill, the PDP transferred the MegaMemory contents via a Unibus interface onto a 6250 BPI magnetic tape.

Counting rate monitors (SEM, AMON, TFI's, TGO's, various detector element and logic unit outputs, etc.) were recorded in Jorway J001 CAMAC scalers, and were also written onto tape at the end the spill. Table 3.1 lists some average counting rates per spill for each target.

3.8 Summary of Collected Data

The data was separated into two large sets for analysis purposes, corresponding to the two different SM12 current settings, 4000 *Amps* and 2750 *Amps*. Most of the 4000-*Amp* data was taken with the 10-*mil* target, while most of the 2750-*Amp* data was taken with the 17-*mil* target. Table 3.2 lists the total number of protons on target for each set.

---

[8]J. A. Crittenden *et al.*, IEEE Trans. Nucl. Sci. Ns 31 (1984) 1028.

[9]R. E. Plaag, Ph. D. Thesis, University of Washington, 1986; R. E. Plaag and J. P. Rutherfoord, Nucl. Instr. & Meth. A273 (1988) 177.

Scaler	Target	
	10-*mil*	17-*mil*
SEM	2.4×10^4	1.9×10^4
AMON	2.5×10^6	2.0×10^6
AMON $\odot$ SB	2.2×10^6	1.7×10^6
$\frac{3}{4}\mu_L$	1.6×10^7	1.7×10^7
$\frac{3}{4}\mu_R$	1.6×10^7	1.7×10^7
$\frac{3}{4}\mu_L \odot \frac{3}{4}\mu_R$	1.0×10^6	9.3×10^5
SINK	2.0×10^3	3.8×10^3
SINK $\odot$ SB	1.7×10^3	3.2×10^3
$\frac{3}{4}\mu_{LR}$	9.5×10^5	—
$\frac{3}{4}\mu_{LR} \odot$ SB	8.5×10^5	—
NX3	4.5×10^3	1.5×10^3
S3ref	4.2×10^5	3.8×10^5
Y1R3	8.6×10^6	6.7×10^7
Y2R10	5.5×10^6	4.6×10^6
X3L7	5.6×10^6	4.7×10^6
Y4L	6.7×10^6	1.0×10^7
X4L	4.6×10^6	6.5×10^6

Table 3.1: Average counting rates per spill.

	Data Set			
	4000-*Amp*		2750-*Amp*	
	10-*mil*	17-*mil*	10-*mil*	17-*mil*
MegaSEM	1056	39	160	394
Number of protons	8.5×10^{16}	3.1×10^{15}	1.3×10^{16}	3.2×10^{16}
Number of triggers	3.2×10^7	1.2×10^6	2.6×10^6	6.3×10^6
Number of events:				
with loose cuts	70440	2600	11310	27850
final sample	42108	1555	5623	13847

Table 3.2: Summary of collected data.

Chapter 4

Data Analysis

The steps needed to analyze the data are described in the first section. Corrections and integrated luminosities are presented in the last section.

4.1 Data Reduction

Data reduction was divided into four stages. At each stage, except for the last one, all raw information on the data tape was passed together with software information (positions, momenta, etc.) to an output disk file for events which appeared to contain two good muon tracks at that stage of the analysis. The first stage, FAST, read raw data tapes and did track reconstruction without Station 0. The second stage, DIMUON, searched for 2 opposite-sign muon tracks and passed them to the following stage, FITST0. In FITST0, a complete track reconstruction was done, using all 22 chambers. Finally, MICRO traced tracks back to the target and made tight cuts on the locations of the muon trajectories inside SM12.

4.1.1 FAST

The first requirement for an event to be analyzed was that its length should be shorter than 1776 words. Events longer than that could have been lost due to memory and time limitations on the Fermilab Cyber computers. Secondly, FAST selected only SINK triggers. Then, it made several general cuts before tracking, since track reconstruction was a very time-consuming process. After tracking, it cross-checked the muon identity of the track and traced it back to the downstream end of the beam dump, where it made

34

a loose trajectory cut. Table 4.1 shows the event selection summary for a typical run (run number 3812, taken on 19-May-85). The event selection criteria are given below.

First of all, FAST required the Trigger Processor to have found a target pair. Then, it checked that the event was properly formatted, *i.e.*, checked for Readout System errors. Next, events with a pseudo-mass smaller than 4 *GeV*, or a number of tracks found by the processor greater than 30, were rejected. FAST then made a hodoscope multiplicity cut if the total number of recorded hodoscope hits in all seven planes was greater than 45. After that, trigger matrix roads were formed using counter hits in Y1 and Y2, while considering only those of Y4 that were within ±5.1 *cm* of any extrapolated segment (with a slope smaller than 0.1 *radians*) joining PTY1 and PTY2 hits. If more than 6 or less than 2 matrix roads were found, the event was also rejected. The next step consisted of creating chamber hit windows for Stations 1, 2, and 3, using the matrix roads. Finally, FAST restricted the set of *y*-hits considered by the trackfinder to those found by the Trigger Processor inside the matrix windows. Within the chamber hit windows, the tracking algorithm JACTRACK[1] searched for sets of *y-u-v* triplets in Station 2 and 3 drift chambers. A triplet consisted of at least 3 crossed wire-hits whose intersections were very close together, and contained at least one associated pair of hits (primed and unprimed views) called doublets. After all triplets were found, JACTRACK searched for doublets which were not subsets of the previously found triplets. If no triplets were found or the number of triplet combinations between Stations 2 and 3 exceeded 10000, the event was rejected. It then looped over all combinations of Station 2 and 3 doublets and triplets to form a list of all track segments (called DC track segments) whose *x-z* views were consistent with a track coming from the target. If no DC track segments were found or their number exceeded 150, the event was thrown out. Next, each of the DC track segments was checked to see if it could be matched with a track segment in the Station 1 MWPC's to form a track candidate emerging from the SM12 aperture. Finally, the hits along each of the track candidates were fitted into two straight-line segments (joined at the bend plane of SM3) to determine the trajectory parameters and momentum. (As explained in Section 2.4.3, the momentum is obtained from the bend angle in the *y-z* view at the SM3 bend plane.) JACTRACK

---

[1] J. A. Crittenden, JACTRACK, E605 Internal Report of March 25, 1983;

H. D. Glass, Ph. D. Thesis, SUNY at Stony Brook, 1985.

Requirement	Passed	Failed	Percentage
Before Tracking:			
Ev. length $\leq$ 1776	71334	791	99 %
SINK trigger	52700	18634	74 %
Proc. target pair	47718	4982	91 %
Event format	47717	1	$\sim$ 100 %
Proc. mass $\geq 4\,GeV$	47696	21	$\sim$ 100 %
Proc. tracks $\leq$ 30	37336	10360	78 %
Hodo multipl. $\leq$ 45	35834	1502	96 %
$2 \leq$ matrix roads $\leq$ 6	32658	3176	91 %
During Tracking:			
Triplets found	32212	446	97 %
Triplet comb. $\leq$ 10000	31544	668	98 %
DC segments found	30185	1359	96 %
DC segments $\leq$ 150	29422	763	97 %
Tracks found	21615	7807	73 %
After Tracking:			
At least two ($\pm$) muons	5322	16293	25 %
$2 \leq$ target muons $\leq$ 4	1365	3957	26 %

Table 4.1: Fast selection summary for run 3812. Run 3812 had an average of 26 600 SEM counts per spill (totaling 6.5×10^{14} protons on target in 107 spills), and a grand total of 72125 triggers on tape. Columns *Passed* and *Failed* refer to the number of events (triggers) that passed or failed the requirement to the left, while *Percentage* is the percentage of events that passed with respect to the total in any particular row. Thus, the percentage of events accepted by FAST, from the total number of events in the raw data tape, is approximately 2 %.

made a final cut if no tracks were found, or each of the tracks found contained less than the required number of hits per station. A minimum of three out of six chamber hits at Station 1, and a minimum of four out of six chamber hits in each of the Stations 2 and 3 were required for each track, which is a minimum of 11 out of 18 chamber hits per track.

For each track found, at least three out of five hits at Station 4 were needed for muon identification. Any event with at least two opposite sign muons was considered for traceback, otherwise the event was rejected. Each one of the muons' trajectories was then traced back to the dump using a crude SM12 magnetic field map. The only purpose of such a traceback was to provide a means of rejecting muons which had clearly originated in the beam dump or scattered off the SM12 interior walls. The track was rejected if the absolute value of its y-coordinate at the beam dump ($z = 2.64\,m$) was smaller than $12.70\,cm$. Finally, events with more than one, but less than five, muon tracks were written on an output file to be analyzed in the next stage. As shown in Table 4.1, approximately 2 % of all the events in a raw data tape were accepted for further analysis.

4.1.2 DIMUON

At this stage, events with two, opposite-sign, target muons were selected. As the selection procedure was essentially performed again at the MICRO level, only a description of its basic elements is given and the details are left until then.

Each track found in FAST was traced back to the target through SM12, starting at the SM3 bend plane. SM12 was considered as a series of small submagnets ($45.72\,cm$ long in the z-direction), each with its own p_t-kick and bend plane. Energy loss and multiple scattering at the lead wall were taken into account when defining the muon's position and momentum inside SM12. y position at the beam dump, y_{dump}, was checked at $z = 2.64\,m$ and $z = 7.52\,m$. x and y positions at the target, x_t and y_t, were also checked. Tracks were rejected if they pointed to the beam dump ($|\,y_{dump}\,| \leq 12.7\,cm$), or outside the target ($|\,x_t\,|$ or $|\,y_t\,| \geq 20.32\,cm$). Events with only two, opposite-sign, target muons were passed to the following stage.

From the FAST output sample of 1365 events for run 3812, only 324 events had two opposite-sign target muons. Thus, DIMUON contributed with a factor of about 4 to the data compression, reducing the original data

down to approximately 0.5 %.

4.1.3 FITST0

In order to improve the knowledge of both the track momentum and the position at the lead wall, Station 0 hits were then added to the fit. Tracking was repeated, as in FAST. This time, the complete SM3 field map was used, along with a correction for the SM12 fringe field downstream of Station 0. Then, a 22-plane fit to each trajectory was done and a new momentum was obtained. A minimum of two of the four possible Station 0 chamber hits were required.

Continuing with the event selection for run 3812, FITST0 rejected about 8 % of the DIMUON output sample.

4.1.4 MICRO

At this stage, the new FITST0 momentum measurements plus a fine-grained SM12 field map was used to retrace the potential target-muon pairs already found in DIMUON. Again, SM12 was considered as a series of small submagnets, but this time $10.24\,cm$ long in the z-direction (compared to the $45.72\,cm$ used in DIMUON). After tracing tracks to the target, only quantities relevant to each event (momentum, track parameters, etc), run and spill numbers, and a few scalers (SEM, AMON, etc.) were stored in small disk files.

Besides the target-track requirement (as explained below), tracks were also required to have fired the corresponding elements of the Trigger Matrix to ensure that the event was not triggered by accidental hodoscope hits.

Traceback Procedure

The problem is how to calculate the muon's momentum at the target if the following quantities are given: the SM12 magnetic field $(B_x,0,0)$, the dimensions and locations of the lead and polyethylene absorber walls, the muon's position and momentum at the SM3 bend plane, and the constraint of the target center as the production point. The solution can be separated into two parts: first, solving the problem without the absorbers; and second, incorporating their effects.

For a particle of charge q and momentum (P_{ox}, P_{oy}, P_{oz}) at (x_o, y_o, z_o) that crosses a magnetic field $(B_x, 0, 0)$, its momentum and transverse position at plane z are given by

$$x = x_o + \int_{z_o}^z \frac{P_x}{P_z} dz \approx x_o + \theta_{ox}(z - z_o)$$

$$y = y_o + \int_{z_o}^z \frac{P_y}{P_z} dz \approx y_o + \theta_{oy}(z - z_o) + \frac{q}{P_{oz}c} \int_{z_o}^z dz' \int_{z_o}^{z'} B_x \, dz''$$

$$P_x = P_{ox}$$

$$P_y = P_{oy} + \frac{q}{c} \int_{z_o}^z B_x dz$$

$$P_z = \sqrt{P_{oyz}^2 - P_y^2}$$

where the approximations are made for small deflection angles; and $\theta_i = P_i/P_z$, $P_{oyz}^2 = P_{oy}^2 + P_{oz}^2$, and c is the speed of light.

The effects of the absorbers on a high energy muon are multiple scattering and energy loss[2]. Multiple scattering is mainly due to Coulomb scattering from the atomic nuclei, while energy loss is caused by several processes. The important mechanisms by which a muon (at our energies) loses energy to matter are: 1) Ionization, i.e., transfer of energy to electrons in the medium. 2) Bremsstrahlung, i.e., emission of photons in the electromagnetic field of the nucleus. 3) Pair production, i.e., production of electron-positron pairs also in the electromagnetic field of the nucleus.

Since both energy loss and multiple scattering are random processes, what is usually known is their average values for a given muon momentum and material thickness. Thus, one way to correct for the absorbers is to use the above relations[3] to do the traceback, providing that the path along the absorber is broken into many steps of infinitesimal length dz, and correcting for the energy loss appropriately at each step. Another way is to simply consider the net effect of the material as being produced in a single plane, so that the energy loss is corrected for at one point only.

We decided to do the correction using the later technique. We chose the correction plane to be the most probable place for the scattering to occur,

[2] J. P. Rutherfoord, Muon Energy Loss..., E605 Report of July 24, 1986.

D. H. Perkins, Introduction to High Energy Physics, Addison-Wesley, 1987.

[3] The magnetic field (measured without absorbers) inside the absorbers does not change since the absorbers are not ferromagnetic.

which is usually called the effective scattering plane[4]. The net effect of the absorbers was parametrized as an energy loss ΔE and two components for the scattering angle: ϕ_x and ϕ_y (one for each of the x-z and y-z planes). Energy loss distributions were calculated[5] by integrating the mean energy loss distributions in an infinitesimal piece of material. Figure 4.1 shows the energy loss distributions (at different incident energies) for muons in $1.22\,m$ of lead. The median values of those distributions were fitted as a function of the incident muon energy E to obtain the energy loss correction due to the lead wall. The fit gave

$$\Delta E_{Pb}\,(GeV) = 2.031435 + 0.0105134\,E\,(GeV)\,.$$

The Bethe-Block formula[6] was used to correct for the mean ionization energy loss due to the polyethylene wall. It gave

$$\Delta E_{CH_2}\,(GeV) = 0.166085 + 0.000197\,E\,(GeV)\,.$$

The energy loss correction ΔE is just the sum $\Delta E_{CH_2} + \Delta E_{Pb}$. Once ΔE is known, the scattering angle correction can be obtained from the constraint of the target center as the production point.

Figure 4.2 schematically shows how the scattering angle can be deduced from the target constraint. First, the track is traced from the SM3 bend plane z_{SM3} to the scattering plane z_{sc}. Then, at z_{sc} the momentum magnitude $P = \sqrt{P_x + P_y + P_z}$ is incremented by ΔE, and the track is projected back toward the target center[7] $(0,0,z_t)$. If the track misses the target by x_t and y_t, the scattering angles ϕ_x and ϕ_y are given by

$$\phi_x = \frac{x_t}{z_{sc} - z_t} \quad \text{and} \quad \phi_y = \frac{y_t}{z_{sc} - z_t}\;,$$

as can be shown using the bend plane approximation. Next, the angles θ_x and θ_y at z_{sc} are changed to $\theta_x + \phi_x$ and $\theta_y + \phi_y$ respectively, and the traceback repeated. This procedure is iterated until the track converges to the target.

---

[4]It can be shown, neglecting energy loss, that the effective scattering plane is $\frac{1}{3}$ of the distance through the absorber. See for example B. Rossi, High Energy Particles, Prentice-Hall, 1952.

[5]J. P. Rutherfoord, Muon Energy Loss..., E605 Report of July 24, 1986.

[6]Particle Data Group, Review of Particle Properties, Phys. Lett. 170B (1986) 44.

[7]The actual target center was at $(0, -3.6\,mm, -3.3\,m)$.
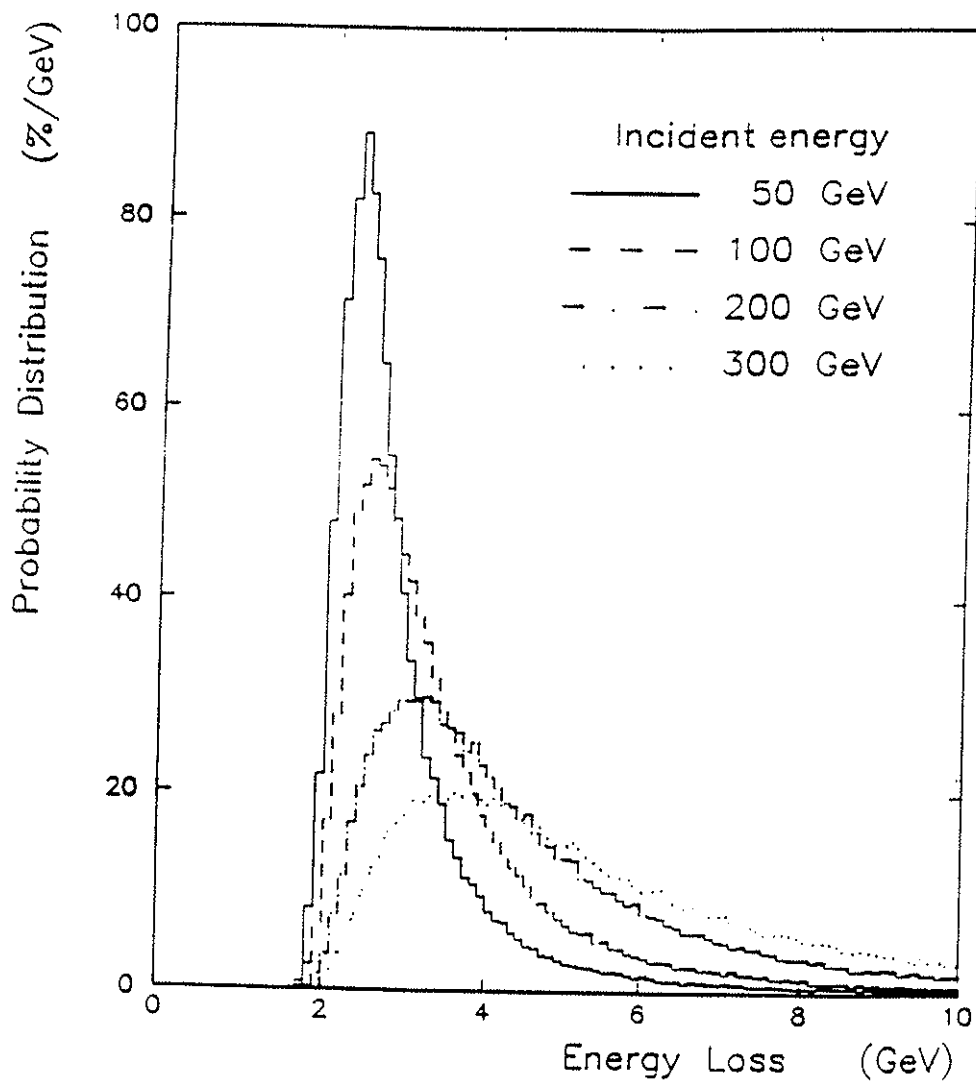
Figure 4.1: Energy loss distributions for muons traversing 122 *cm* of lead.
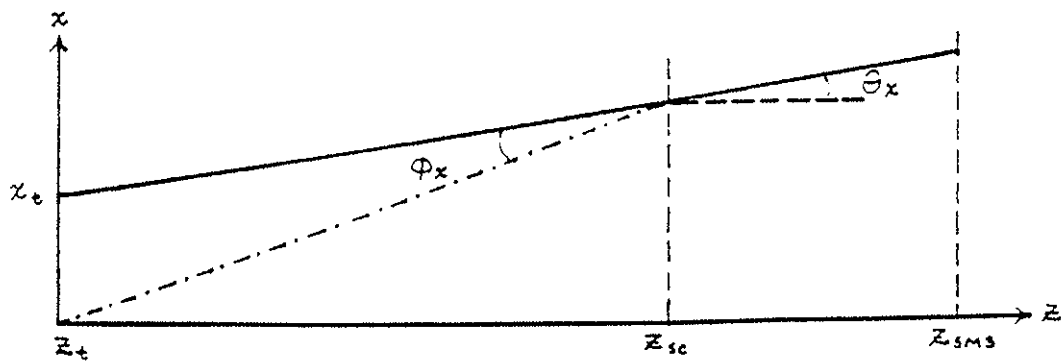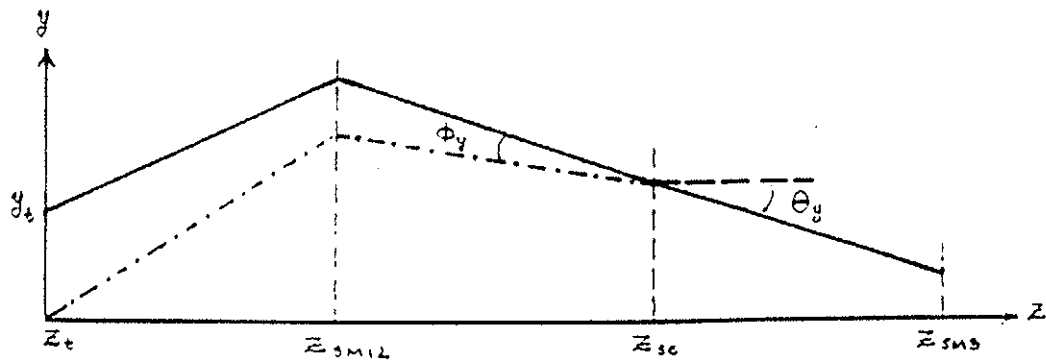
Figure 4.2: The target constraint is used to determine the scattering angles ϕ_x and ϕ_y as explained in the text.

In our experiment, usually two or three iterations were sufficient to achieve a traceback residual miss distance at the target center of less than $25\,\mu m$.

The above iteration procedure is only accurate for the statistical average of all the tracks, individual muon trajectories upstream of the absorber wall might differ significantly from the trajectory iterated to the target center. In order to rid the data set of muons which had scattered off the beam dump and walls of the magnet, trajectories from the last iteration were required to be inside an apparent SM12 fiducial volume smaller than the actual clear aperture. The dump cut was extended to $\pm 15.75\,cm$, $5.4\,mm$ outside the physical dump; and the angular aperture in the xz-plane was reduced from $2.7°$ to $2.5°$, rejecting tracks whose x-coordinate at $z_{sc} = 13.17\,m$ was larger than $35.6\,cm$ in absolute value. It is possible that some muons might have suffered a much larger than the average energy loss or multiple scattering in the absorbers, resulting in a very large miss distance at the target center when traced without the scattering angle correction. To avoid this, non-iterated tracks were required to hit the target spot defined by $\mid x_t \mid\leq 12.7\,cm$ and $\mid y_t \mid\leq 12.7\,cm$ at $z_t = -3.30\,m$.

4.2 Cut Summary

The complete set of cuts applied to the final sample of events can be summarized as follows:

1. Trigger Selection. Only SINK triggers were considered by FAST for further analysis.

2. Multiplicity cuts. FAST rejected events with more than 45 hodoscope hits, or events with more than 30 processor tracks, or events with more than 6 matrix roads.

3. Tracking Requirements. The tracker in FAST required a minimum of 11 out of 18 chamber hits along each track. Later, when Station 0 was included in the tracking, a minimum of 13 out of 22 chamber hits along each track were required.

4. Muon Selection. A muon was defined in FAST if at least 3 (out of X4, Y4, PTX, PTY1, and PTY2) muon counters had fired along the track.

5. Only muon pairs. DIMUON selected only events with two opposite-sign muons, most of them originated in the target. MICRO then corroborated the target origin using a better SM12 field map and a more precise momentum measurement.

6. Geometrical Cuts. To make sure that tracks went through regions of high detection efficiency, a cut (of $2.54\,cm$) was made on the projected track inside the edges of both X4 and Y4. A second cut (of $\pm 2.54\,cm$) in the central region at X4 defined clearly the left and right sides of the apparatus. The SM12 fiducial volume was defined by the following cuts:

   • The horizontal aperture was determined by $|\ x_{at\ z_{sc}}\ | \le 35.56\,cm$, where $z_{sc} = 13.17\,m$.

   • The dump cut on the iterated track was $|\ y_{at\ z_{dump}}\ | \le 15.86\,cm$, where $z_{dump} = 2.64\,m$.

   • The target cut on the non-iterated track was
   $|\ x_t\ |$ and $|\ y_t\ | \ge 12.7\,cm$, at $z_t = -3.30\,m$.

7. Trigger Requirements. Since our dimuon trigger required the Matrix and 2X4 triggers to be set, only dimuon tracks which passed through trigger elements that satisfy these requirements were retained.

8. Spill Quality Selection. Good spills were defined as those which had good targeting (greater than 70%) and intensity (SEM > 5000).

4.3   Normalization

The production of a particle $\mathcal{C}$ and *anything else*, $\mathcal{X}$, from the interaction of particles $\mathcal{A}$ and $\mathcal{B}$ is represented by

$$\mathcal{A} + \mathcal{B} \longrightarrow \mathcal{C} + \mathcal{X}\ ,$$

and the *cross-section* for such process is defined as

$$\sigma = \frac{\text{number of times that } \mathcal{C} \text{ appears per unit time}}{\text{incident flux of particles } \mathcal{A} \times \text{number of target particles } \mathcal{B}}$$

where the *incident flux of particles* is the number of particles that cross a unit area, perpendicular to the incident direction, per unit time. The numerator is usually called *event rate* and the denominator *luminosity*. The task of the experimenter is then to measure both the event rate and luminosity. Since the period of time is the same in both quantities, what is measured is their time integrals, *i.e.*, *number of events* and *integrated luminosity*.

Our experiment used a proton beam incident on a Cu target and detected only a small fraction of the total number of produced dimuons. Not all of them could be detected for two reasons. First, the detector did not cover the complete dimuon phase space, and second, it was not fully efficient. Therefore the detected number of events must be corrected for efficiency and acceptance (the fraction of the dimuon phase space that was actually covered). Also the measured number of incident protons had to be corrected for targeting and live-time. Targeting is the fraction of incident beam that hit the target, and live-time is the fraction of time that the electronics was able to record events. The following paragraphs describe the methods used to calculate each one of these correction factors. Cross-section calculations will be presented in the next chapter.

4.3.1 Efficiencies

The detection efficiency ϵ_{det} can be expressed as

$$\epsilon_{det} = \epsilon_{SINK} \cdot \epsilon_{proc} \cdot \epsilon_{rec}$$

where the different factors are the SINK trigger efficiency, the Trigger Processor efficiency, and the reconstruction efficiency, respectively.

The trigger efficiency depended strongly on the efficiency of the hodoscope counters. Care was taken to keep each counter highly efficient during the run. The hodoscope efficiency of plane i was measured using muon tracks in which at most plane i did not participate in the reconstructed track, and is given by

$$\epsilon_i = \frac{n_1}{n_1 + n_2} \, ,$$

were n_1 (n_2) is the number of tracks with all the planes (all but plane i) participating in the reconstructed track. Figure 4.3 shows the hodoscope efficiency as a function of time (run number) and indicates the regions in
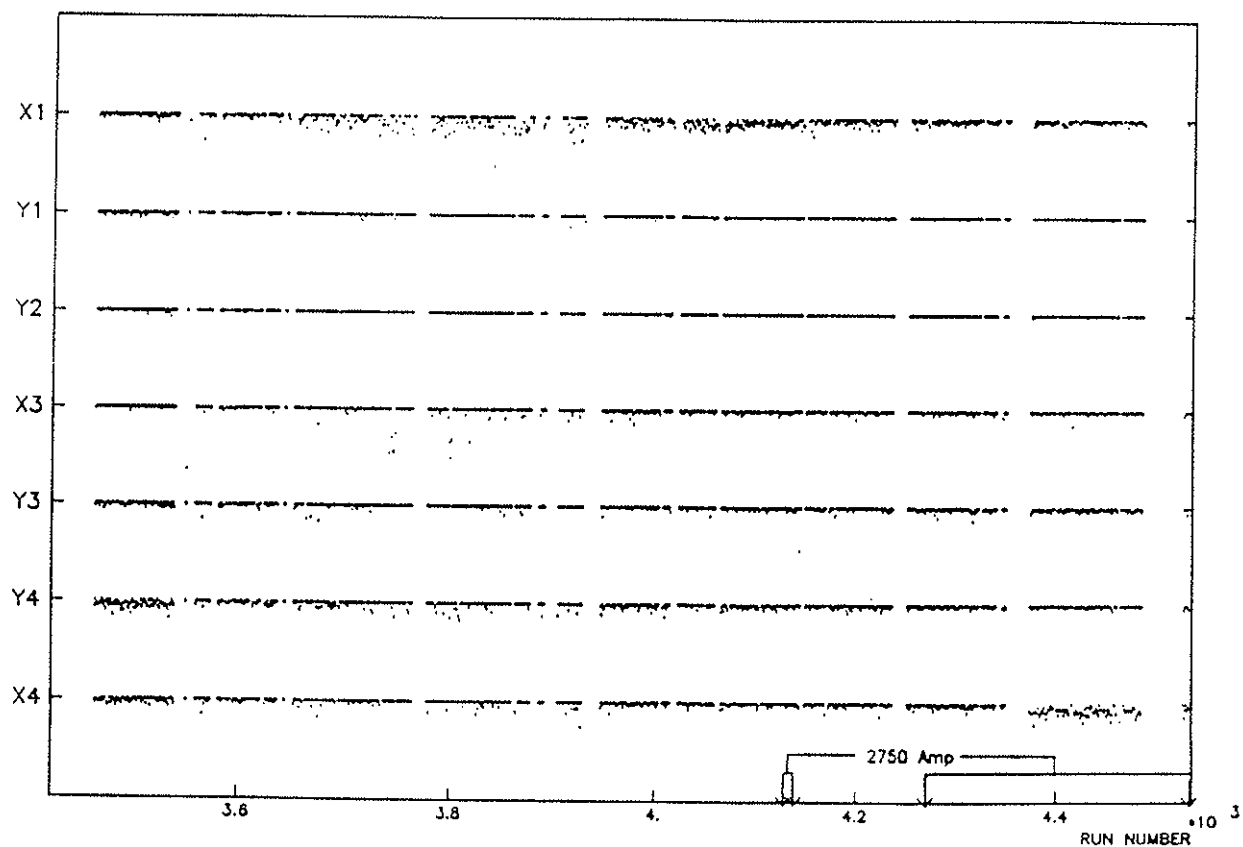
Figure 4.3: Average hodoscope efficiency per plane *versus* run number. The marks on the vertical axis correspond to an efficiency of 100%. The separation between adjacent marks corresponds to the range 0% to 100%.

which the data was divided. Table 4.2 lists the average efficiency of each plane.

The trigger efficiency was divided into four elements: one corresponding to the efficiency of the $\mu_U \odot \mu_D \odot \mu_L \odot \mu_R$ signal (which was a combination

Plane	4000-Amp	2750-Amp
X1	.973 ± .001	.982 ± .001
Y1	.997 ± .000	.999 ± .000
Y2	.999 ± .000	.999 ± .000
X3	.991 ± .001	.995 ± .001
Y3	.993 ± .001	.988 ± .001
X4	.984 ± .001	.996 ± .001
Y4	.990 ± .000	.958 ± .002

Table 4.2: Average hodoscope efficiencies for the two sets of data.

of the trigger matrices), and the remaining corresponding to the multiplicity vetoes 2X4, $\overline{NX1}$, and $\overline{NX3}$. Trigger matrix efficiencies were measured using

Element	4000-Amp	2750-Amp
Matrices	.975 ± .005	-
2X4	.997 ± .002	-
$\overline{NX1}$	.981 ± .004	.987 ± .004
$\overline{NX3}$	.999 ± .001	.999 ± .001
SINK	.954 ± .007	-

Table 4.3: Trigger efficiency.

tracks in events from the study trigger $\frac{3}{4}\mu_{LR}/PS$, in which a software version of the matrices was formed and the results were compared with the corresponding hardware trigger bits. The 2X4 efficiency was calculated using the same sample of events, by comparing the X4 multiplicity and 2X4 trigger bit. The efficiency of the vetoes $\overline{NX1}$ and $\overline{NX3}$ was measured using target pairs from the study trigger μ_{LR}/PS, in which the multiplicity at each plane was compared with the corresponding trigger bit. The results of these calculations are shown in Table 4.3 along with the overall SINK trigger efficiency
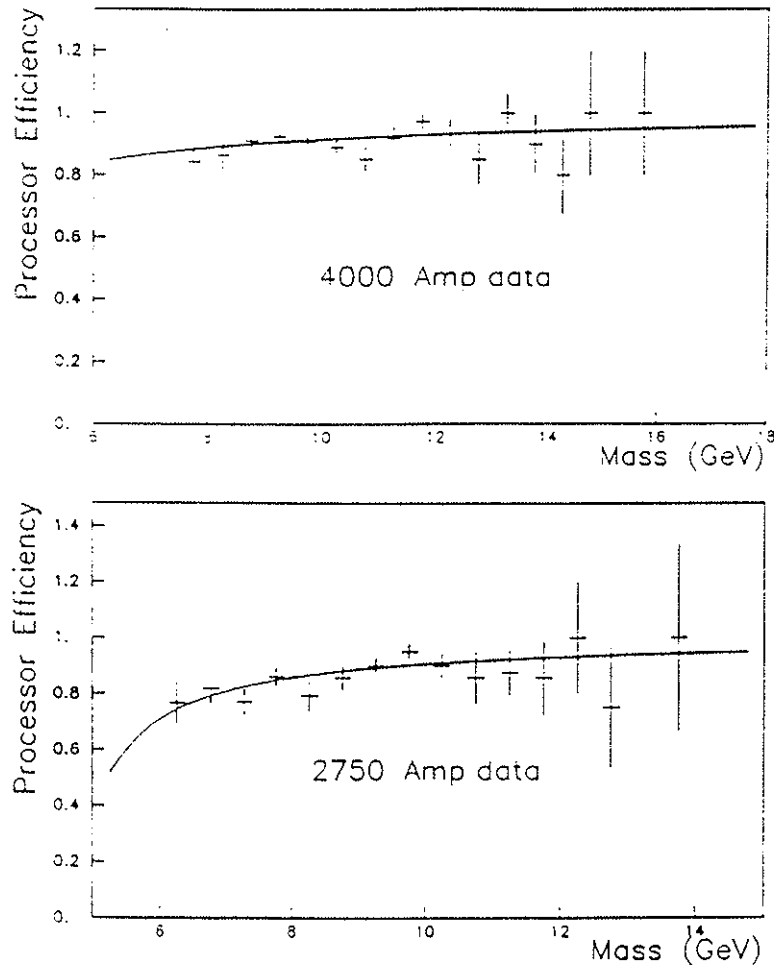
Figure 4.4: Processor efficiency *versus* mass for the two sets of data. The continuous line is the fit function used to correct the data as a function of mass

for the 4000-Amp data. Because the study trigger $\frac{3}{4}\mu_{\text{LR}}/\text{PS}$ was removed during the 2750-Amp running period, we were not able to measure either the matrix efficiency or the 2X4 efficiency for that data set. But, because the hodoscope efficiencies remained almost constant during the whole run, as can be seen in Figure 4.3, we assumed that those efficiencies for the 2750-Amp data were the same as for the 4000-Amp data, giving $\epsilon_{\text{SINK}} = .958 \pm .007$. The Trigger Processor efficiency was measured by finding pairs in events from the prescaled trigger $\mu_{\text{LR}}/\text{PS}$, using a version of the analysis which did not require the Trigger Processor information. Due to the processor mass threshold, the processor efficiency had a slight mass dependence at low mass, as shown in Figure 4.4. The mass dependence was parametrized by fitting a hyperbola to the data points. The data was then corrected as a function of mass with the value of the fit function. Averaged over mass, the Trigger

	4000-Amp	2750-Amp
JACTRACK	$.992 \pm .001$	$.991 \pm .001$
Station 0	$.949 \pm .002$	$.960 \pm .003$
Muon Selection	$1.000 \pm .000$	$1.000 \pm .000$
Matrix Roads	$.999 \pm .001$	$.999 \pm .001$
Processor Tracks	$.999 \pm .001$	$.999 \pm .001$
Hodo Multiplicity	$.997 \pm .002$	$.999 \pm .001$

Table 4.4: Reconstruction efficiencies for the two sets of data.

Processor efficiency was $.905 \pm .008$ for the 4000-Amp data, and $.855 \pm .013$ for the 2750-Amp data.

The reconstruction efficiency (listed in Table 4.4) included the chamber efficiencies for track finding and muon selection, as well as the efficiency of the software cuts that were not included in the geometrical cuts. The tracking efficiency was determined from the data itself. JACTRACK calculated the efficiency of each chamber, excluding Station 0, and then folded them together as in the track-definition requirements. The overall Station 0 efficiency was calculated by looking at the fraction of JACTRACK-found tracks which had at least two Station 0 hits. The muon selection efficiency was defined as the probability of firing at least three out of five Station 4 elements along the track. The software cut efficiencies were calculated using the prescaled events $\mu_{\text{LR}}/\text{PS}$ for which these cuts were relaxed. The main

contribution to the reconstruction inefficiency came from the Station 0 ineffi-
ciency, which accounted for about 5 % per track. The overall reconstruction
efficiencies for two target muons were .882 ± .004 and .905 ± .005 for the
4000-*Amp* data and 2750-*Amp* data, respectively.

4.3.2 Acceptance

The acceptance as a function of any kinematic variable x is propor-
tional to the integral of the production cross-section over all the other vari-
ables, with the limits of integration determined by the placement of detectors;
more precisely,

$$a(x) = \frac{\int_{\Delta\Omega} \sigma d\Omega}{\int_{\Omega} \sigma d\Omega} ,$$

where Ω represents the phase space excluding x and $\Delta\Omega$ is the fraction of Ω
to which the spectrometer is sensitive. The acceptance was evaluated by a
random sampling technique (usually called the Monte Carlo method) based
on a software simulation of the apparatus and the use of a trial functional
form for the cross-section. The simulation[8] included all multiple scattering

Variable	Range	Drell-Yan	Upsilon
m	$(6, 18.5)$	$e^{-\alpha m}$	$\delta(m - m_\Upsilon)$
x'_F	$(-1, 1)$	$(1 - x'_F)^a(1 + x'_F)^b$	$(1 + \tau - \epsilon)^2/\epsilon$
p_t	$(0, p_t^{max})$	$p_t/(1 + (p_t/p_0)^2)^6$	same
ϕ	$(0, 2\pi)$	uniform	uniform
$\cos\theta_{CS}$	$(-1, 1)$	$1 + \cos^2\theta_{CS}$	uniform
ϕ_{CS}	$(0, \pi)$	uniform	uniform

Table 4.5: Distributions used for Drell-Yan and Upsilon event simulation,
where $x_F = (1 - \tau)x'_F$, $\epsilon = \sqrt{4\tau + x_F^2}$, $p_t^{max} = (\sqrt{s}/2)\sqrt{(1 - \tau)^2 - x_F^2}$,
$\alpha = .77$, $a \sim 4$, $b \sim 5$, and $p_0 = 3$ (3.7) for Drell-Yan (Upsilon) dimuons.

and energy loss effects, as well as an accurate geometrical survey of the
apparatus, although it did not include either the Trigger Processor simulation

---

[8]Our Monte Carlo program was written by John P. Rutherfoord of the University of
Washington.
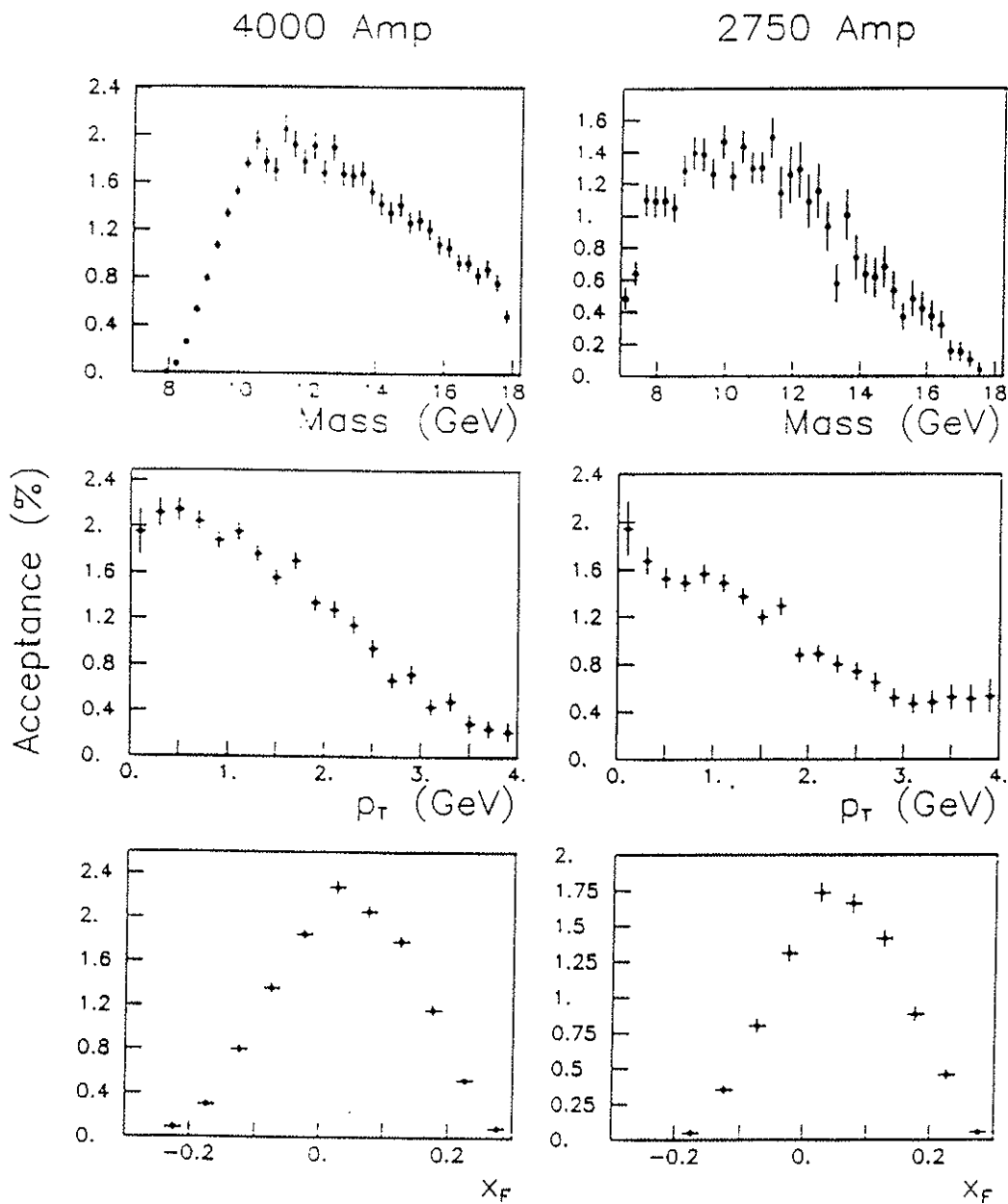
Figure 4.5: Drell-Yan acceptance functions.
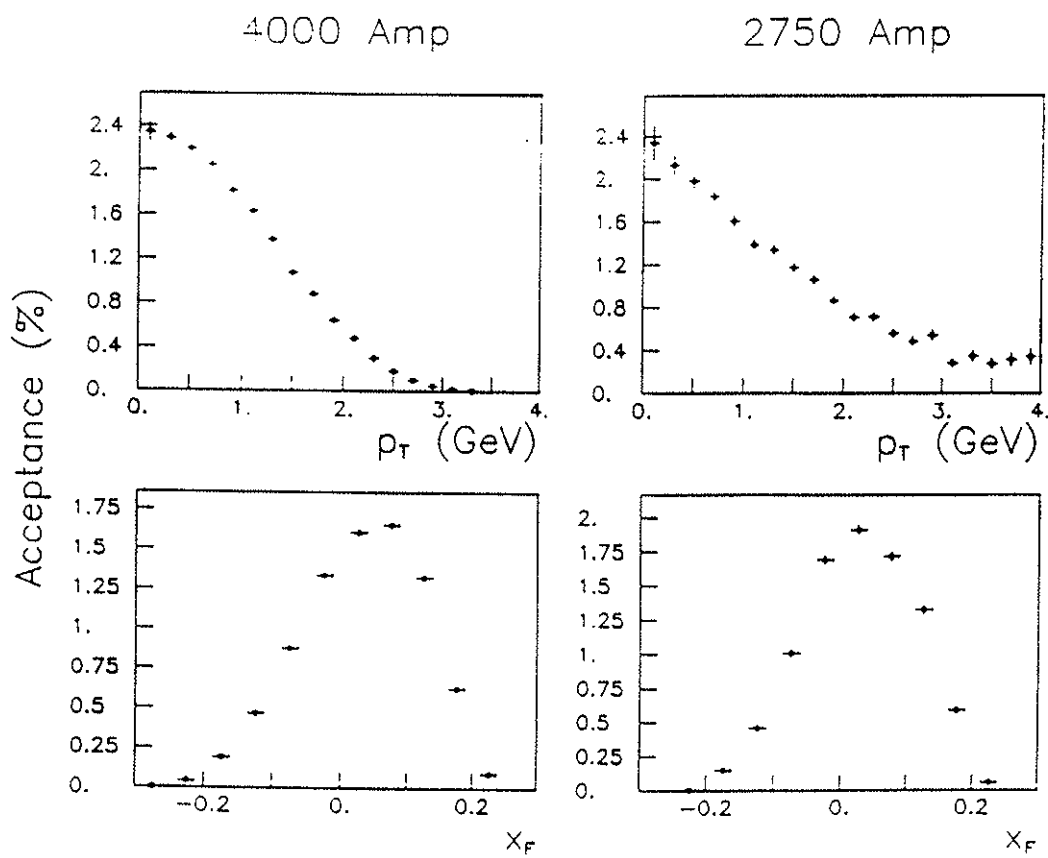
Figure 4.6: Upsilon acceptance functions.

or efficiency corrections. Since the acceptance is calculated as the ratio of two functionals of the assumed cross-section,

$$a[\sigma_{hypothetical}] = \frac{\int_{\Delta\Omega} \sigma_{hypothetical}\, d\Omega}{\int_{\Omega} \sigma_{hypothetical}\, d\Omega}\ ,$$

it is important that the shape of the assumed cross-section closely represents that of the real cross-section. This was achieved by fitting distributions of reconstructed Monte Carlo events to those of real data events in an iterative procedure which converged once self-consistent results were obtained. The assumed cross-section for Drell-Yan pairs $\sigma_{hypothetical}^{DY}$, along with the one for Upsilon pairs $\sigma_{hypothetical}^{\Upsilon}$, are summarized in Table 4.5.

Muon pairs were generated over all the phase space defined in Table 4.5, according to the hypothetical cross-section. Those pairs that traced through the spectrometer successfully were recorded and an emulation of a raw data tape was produced. This fake data was then analyzed as if it were real data (except for the cuts corresponding to the Trigger Processor) since the integral of the assumed cross-section is proportional to the 'observed' number of events. Later, the number of Monte Carlo events that passed the analysis chain was divided by twice[9] the number of generated events to obtain the acceptance in a given region of phase space. For example, Figure 4.5 shows the Drell-Yan acceptance *versus* mass, transverse momentum, and Feynman x, for the two sets of data. The mass acceptance was calculated at equally spaced mass intervals $\Delta m = .283 \mathrm{GeV}$ in order to match the bins of other experiments (see Chapter 5). The longitudinal momentum of the dimuon was generated in the range $0 < x_F < .05$ while the full range of the p_t and angular variables was generated. For the p_t (x_F) acceptance, the phase space considered was $10.5 < m < 11.5\,(GeV)$, $-.1 < x_F < .2$ ($0 < p_t < p_t^{max}$), $0 < \phi < 2\pi$, $0 < \theta_{CS} < \pi$, and $0 < \phi_{CS} < 2\pi$.

The procedure outlined above could give meaningless results when considering the mass acceptance for Upsilons (or any resonance narrower than the experimental resolution). One effect produced by the resolution is to spread out events from the peak to regions where none were generated. Therefore, the Upsilon acceptances were calculated integrating from $m = 8\,GeV$ to the maximum reconstructed mass. Figure 4.6 shows the p_t and x_F acceptance for Upsilons. In all cases, an integration over the angular

---

[9]This factor of two compensates for the fact that ϕ_{CS} was generated over half the allowed range.

variables was performed, and the x_F (p_t) interval for the p_t (x_F) acceptance was $-.1 < x_F < .2$ ($0 < p_t < p_t^{max}$).

4.3.3 Integrated Luminosity

The time integrated beam flux is just the number of incident protons N_{inc} per unit area a. It is given by

$$\int (beam\ flux)\, dt = N_{inc}\, P(x, y) \ ,$$

where $P(x, y)$ is a normalized density function that describes the transverse beam profile at the target. The number of nucleons dN_{tgt} in a small volume $dV = dx\,dy\,dz$ of the target is

$$dN_{tgt} = N_o\, \rho\, dx\, dy\, dz \ ,$$

where N_o is Avogadro's number, ρ is the density of the material, and a linear atomic number dependence of the cross-section is assumed. Since the beam has a probability e^{-z/λ_I} of not-interacting in the target after traversing a distance z, the integrated luminosity is given by

$$L = N_o\, N_{inc}\, \rho \int_{target\ volume} P(x, y)\, dx\, dy\, e^{-z/\lambda_I}\, dz \ ,$$

or, integrating over the target length l

$$L = N_o\, N_{inc}\, \rho \left\{ \int_{transverse\ area} P(x, y)\, dx\, dy \right\} \lambda(1 - e^{-l/\lambda_I}) \ .$$

In this expression, N_{inc} is measure by SEM, the term in curly braces, called targeting, is obtained through target-scans (as explained in Section 2.3), and the remaining factors come from target properties. The average targeting fraction per spill was $86 \pm 3\%$ for the $10\,mil$ target, and $95 \pm 3\%$ for the $17\,mil$ target.

The integrated luminosity also had to be corrected for the protons that interacted while the readout process had prevented (gated) the electronics from recording more events. This correction, called live-time, was measured as the fraction of the number of gated SINK triggers to the number of ungated ones. The average live-time per spill was $89 \pm 3\%$ for the 4000-Amp data, and $82 \pm 4\%$ for the 2750-Amp data.

Because both targeting and live-time depended on the detailed time structure of the accelerator's spill, the integrated luminosity was evaluated as the sum of the integrated luminosities per spill, obtaining

$$11.3 \times 10^{41} \ nucleon/cm^2 \ \text{and} \ 2.5 \times 10^{41} \ nucleon/cm^2$$

for the 4000-Amp data and the 2750-Amp data, respectively.

Chapter 5

Results and Conclusions

5.1 Introduction

Results are presented as functions of one or two of the kinematical variables m, p_t, x_f, or y (which were defined in Chapter 1 in connection with the Drell-Yan description of dimuon production). An integration over the angular variables was performed either because they are trivial or the range measured is too narrow to distinguish among different shapes. The errors quoted throughout are statistical only (unless otherwise stated) and an overall normalization systematic error of about 10% (5% due to the SEM calibration and 5% due to the various efficiencies, see Tables 4.2 to 4.4) should be added.

Figure 5.1 (5.2) shows the raw distributions in the various kinematical variables for the 4000-Amp (2750-Amp) data set. Three peaks are clearly seen in the mass spectrum (also shown in Figure 5.3), corresponding to the Υ, Υ', and Υ'', in order of increasing mass. No obvious resonances are observed in the other distributions. The sinusoidal shape of both ϕ and ϕ_{CS} is partly due to the exclusion of muons from the central X4 and Y4 counters (the 2X4 requirement of the SINK trigger and the wedge missing from the Y4 hodoscope plane).

To convert these distributions to differential cross-sections, the definition given in the previous chapter is used. For example, if Ω represents any
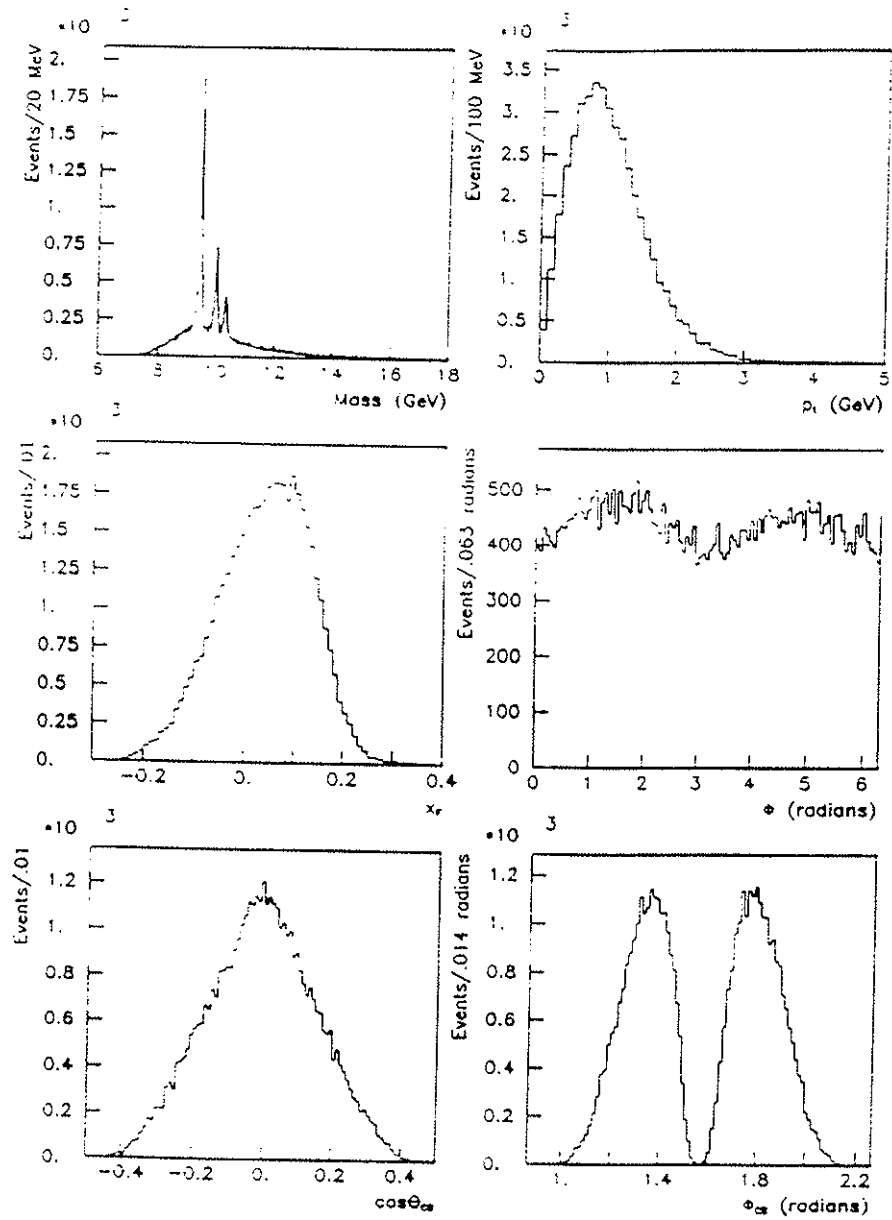
Figure 5.1: Raw distributions of the 4000-*Amp* data set.
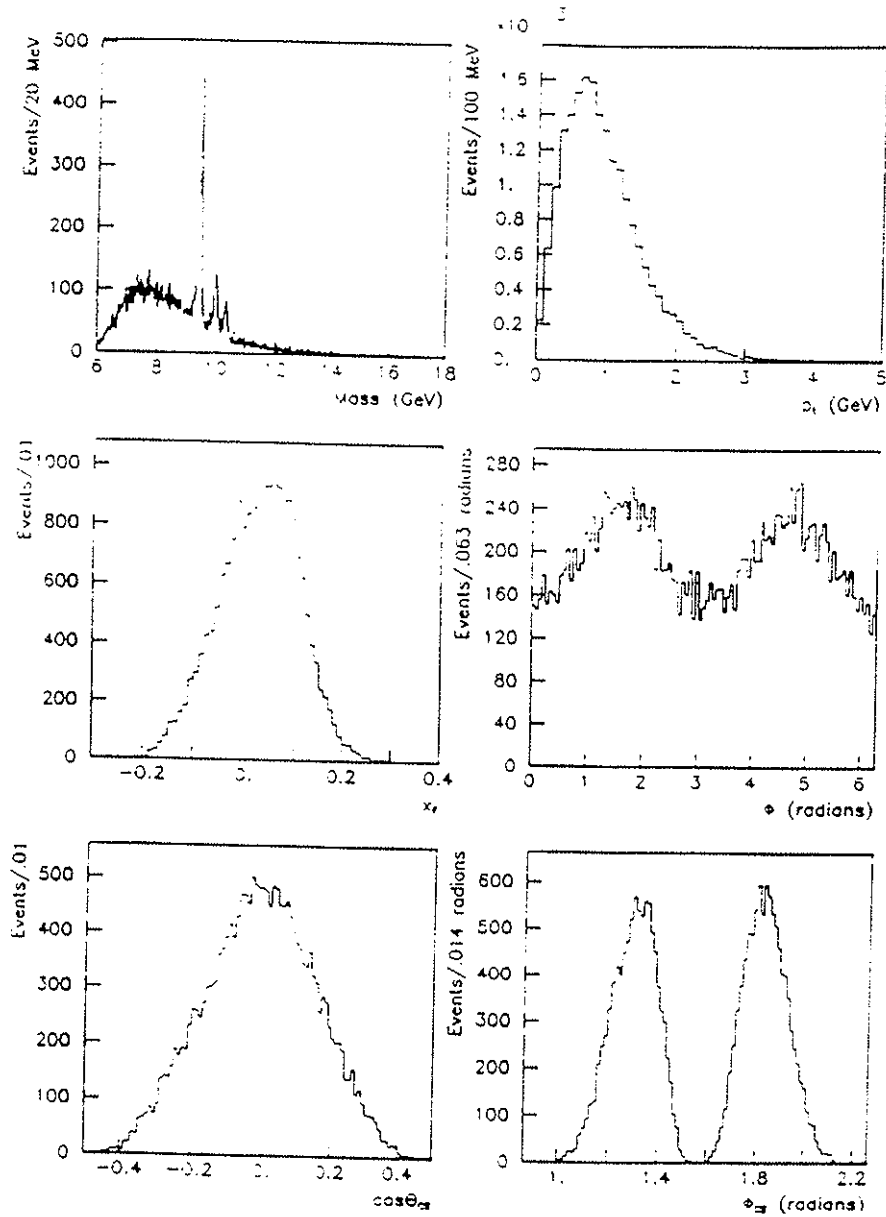
Figure 5.2: Raw distributions of the 2750-*Amp* data set.
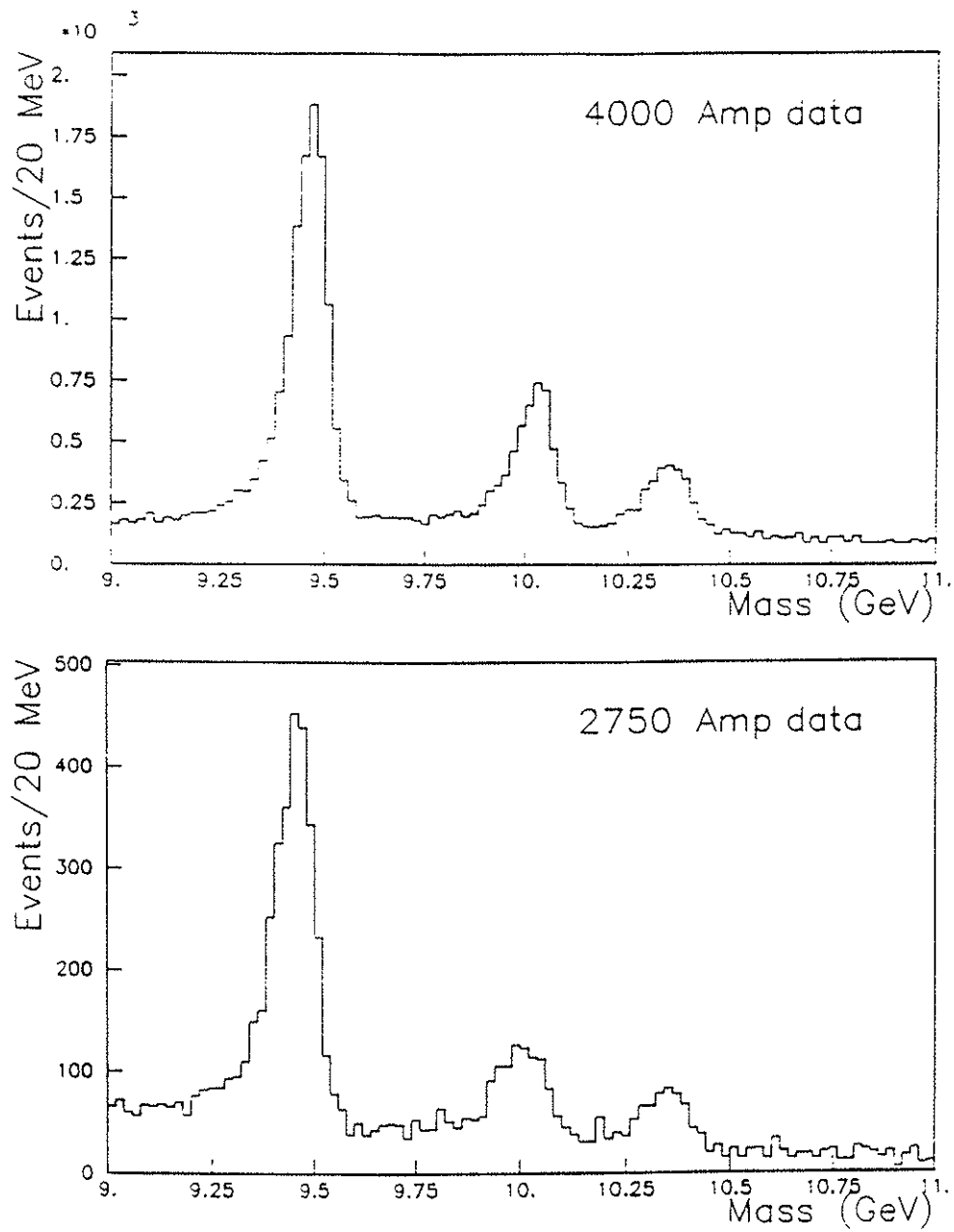
Figure 5.3: Upsilons.
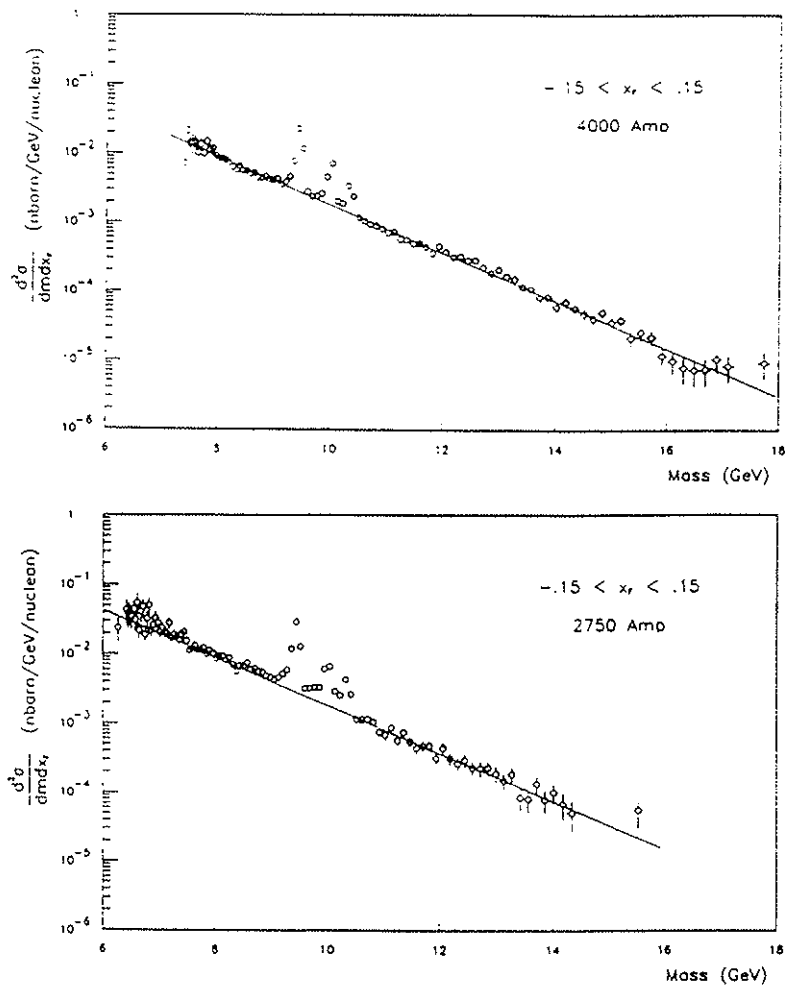
Figure 5.4: $\frac{d^2\sigma}{dmdx_F}$ *versus m*. The continuous line is a simultaneous fit to both sets of data.

kinematical variable, $\langle \Omega \rangle$ its mean value in the interval $\Delta \Omega$, then

$$\left. \frac{d\sigma}{d\Omega} \right|_{\Omega = \langle \Omega \rangle} \equiv \left\langle \frac{d\sigma}{d\Omega} \right\rangle ,$$

where the right hand side is the measured *average cross section*:

$$\left\langle \frac{d\sigma}{d\Omega} \right\rangle = \frac{1}{L_{\mathrm{corr}}} \cdot \frac{N_{ev}}{a\epsilon} \cdot \frac{1}{\Delta \Omega},$$

N_{ev} being the raw number of events in $\Delta \Omega$, corrected for the processor efficiency as a function of mass; a the acceptance, ϵ the detection efficiency excluding the processor efficiency; and L_{corr} the integrated luminosity corrected for targeting and live time.

Figure 5.4 shows $d^2\sigma/dmdx_F$ *versus* m evaluated at $x_F \simeq 0$ for our two sets of data. The data is presented in variable size mass bins corresponding to a mass resolution [full width at half maximum $\Delta m = .017m - .077$ (GeV)] determined by the 4000-Amp Monte Carlo data. The x_F range considered in this calculation was $(-.15, +.15)$, and the acceptance correction was done for the continuum only. The spectra reveal no statistically significant resonance peaks other than the Upsilons already seen in the raw spectra.

5.2 Drell-Yan Cross-Sections

5.2.1 Scaling Comparisons

Scaling comparisons of our data with results from experiments E288[1] and NA3[2] are presented in several ways. Care was taken to bin our data in the same bins as reported in the other experiments. A possible source of error in doing this could arise if the resolution is drastically different among experiments. But, since bin sizes are (presumably) chosen as to 'smooth out' this effect, we believe that the comparison is meaningful. There is another source of systematic error coming from the uncertainty on the incident flux measurements. NA3 reported an uncertainty of about 12% on their luminosity measurement and E288 assumed their global systematic error to be less than 25%. E288 also reported that for their SEM calibration (similar to the

[1] A. S. Ito *et al.*, Phys. Rev. **D23** (1981) 604.

[2] J. Badier *et al.*, Z. Phys. **C26** (1985) 489.
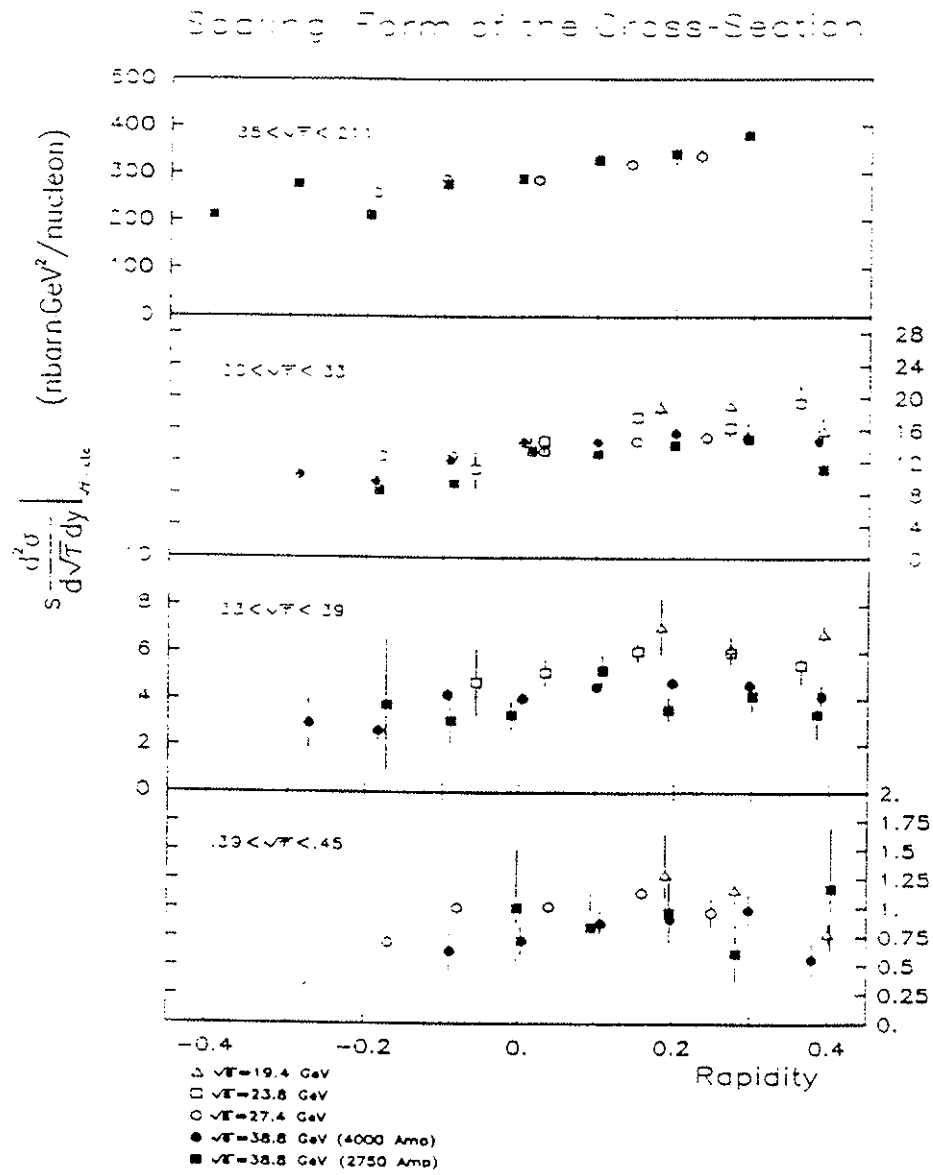
Figure 5.5: Comparison of the measured cross-section *versus* rapidity at constant $\sqrt{\tau}$ with the data of E288 (A. S. Ito *et al.*[1]).
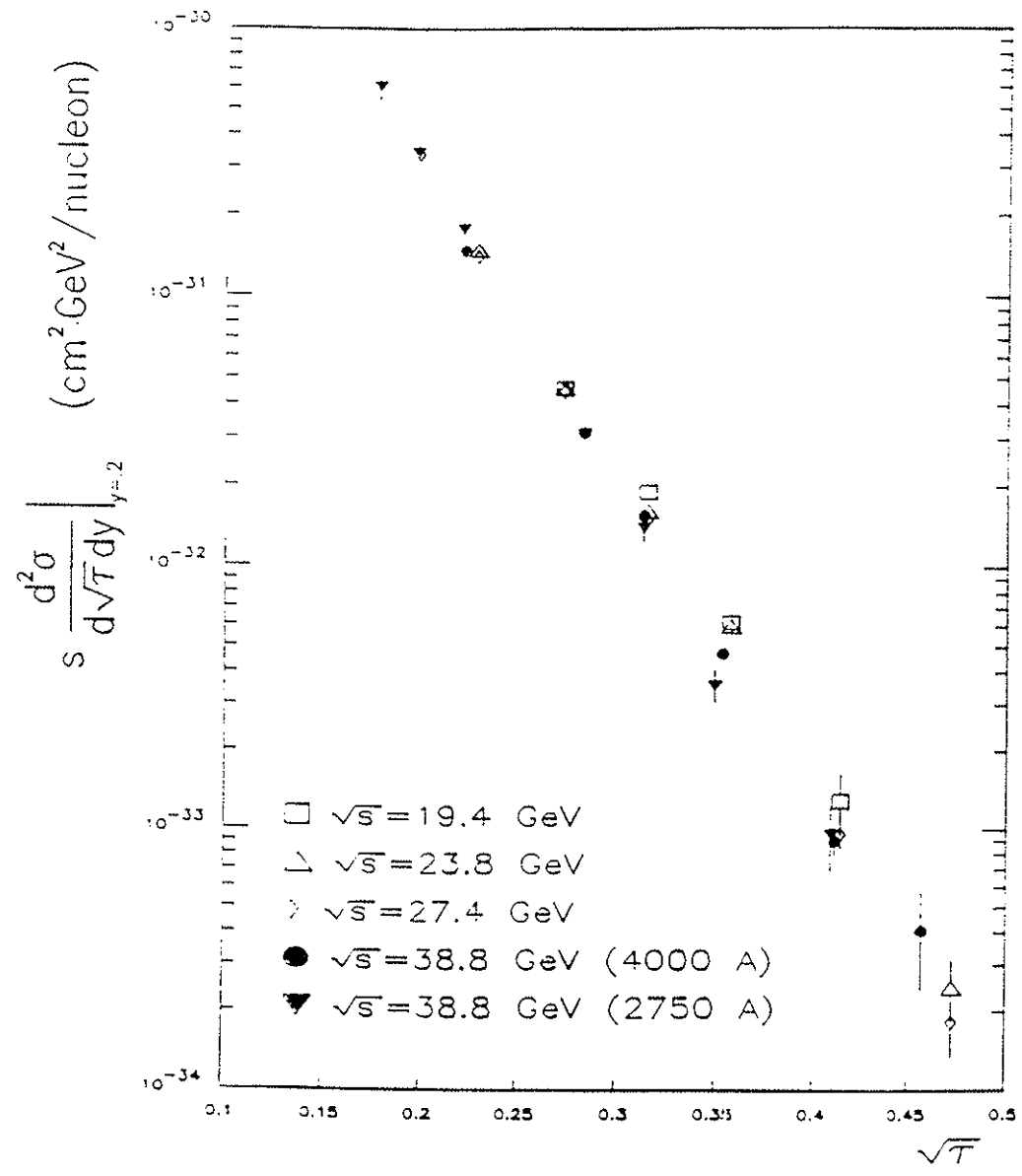
Figure 5.6: Comparison of the measured cross-section *versus* $\sqrt{\tau}$ at $y = .2$ with the data of E288.

Scaling Form of the Cross-Section
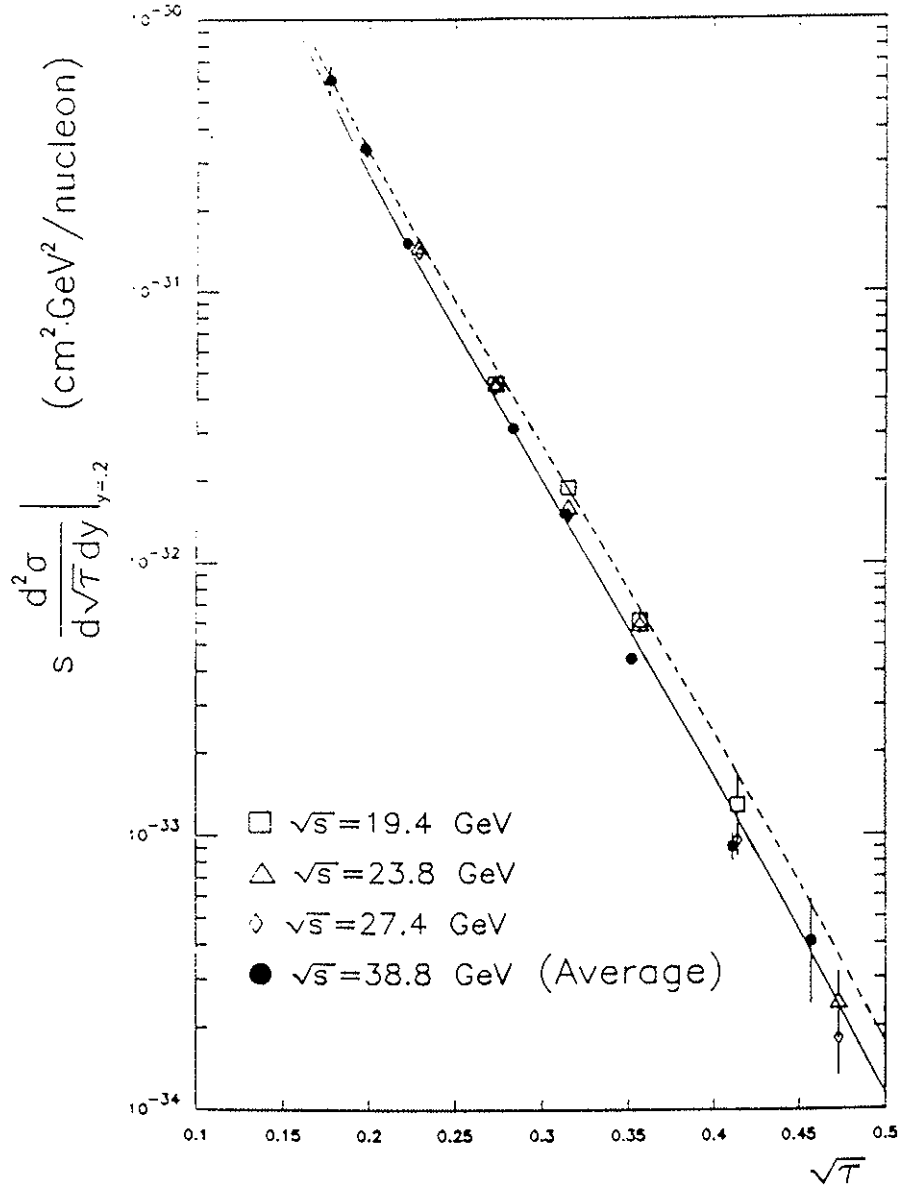
Figure 5.7: Comparison of our averaged data with E288 data. The lines are the $O(\alpha_s)$ QCD predictions of Martin et al[5]. The dashed line corresponds to $\sqrt{s} = 19.4\,GeV$ and the continuous line corresponds to $\sqrt{s} = 38.8\,GeV$.

one described in Section 2.2.2), the value of the cross-section for ^{24}Na production by protons on Copper used was $3.5\,mbarn$, in contrast to the value used in our analysis of $3.9\,mbarn$. If $3.9\,mbarn$ were used to modify the E288 results, their cross-sections would increase by 11%. Conversely, had we used $3.5\,mbarn$, our cross-sections would decrease by 10%.

The three experiments assumed a linear dependence of the cross-section on the atomic number of the target. Most of the E288 data was taken with either Platinum or Copper targets. They also used a Beryllium target. NA3 had a Platinum target and we used a Copper target. While E288 and NA3 corrected their data for nuclear motion in the target, we did not apply that correction to our data. E288 parametrized this correction (averaged over the y acceptance) as

$$\frac{\left(\frac{d^2\sigma}{d\sqrt{\tau}dy}\right)_{corr}}{\left(\frac{d^2\sigma}{d\sqrt{\tau}dy}\right)_{uncorr}} = 0.901 + 0.827\sqrt{\tau} - 2.54\tau \ ,$$

which results in a 4% decrease of the corrected cross-section at $\sqrt{\tau} = .2$, and 17% decrease at $\sqrt{\tau} = .4$. In these comparisons we have used the values, corrected for nuclear motion, that were reported by E288 and NA3 and compared them with our uncorrected values.

The scaling form of the cross section, $s\,d^2\sigma/d\sqrt{\tau}dy$ versus y for different $\sqrt{\tau}$ bins, is compared to that of E288[3] in Figure 5.5 and tabulated in Table 5.4. The figure shows two interesting features: 1) there is a positive slope in the cross section at $y = 0$ for fixed $\sqrt{\tau}$; and 2) our data is lower than theirs as $\sqrt{\tau}$ increases (this difference would increase if we had removed the correction for nuclear motion in their data). The Drell-Yan model predicts a positive slope in y for pn collisions due to the e_i^2 term in the cross-section even if the anti-quark sea in nucleons is symmetric. Note, our copper target has 1.19 neutrons per proton (1.06 d valance quark per u valance quark).

The first observation, a positive slope at $y = 0$, appears to be larger than that predicted by the Drell-Yan model using a symmetric anti-quark sea. Ito et al.[1] and Kaplan[4] noted that the increased slope might derive from an unequal $\bar{u}$ and $\bar{d}$ content in a nucleon.

---

[3] We think that there is a typographic error in Table XI, of Ito et al., ibid, page 623, where they claim the cross-section versus y, at $\sqrt{\tau} = .414$ for their $400\,GeV$ data, to be an order of magnitude higher than the value plotted on Figure 14A, page 621. For this comparison, we assumed that the values plotted are correct.

[4] D. M. Kaplan, Ph. D. Thesis, SUNY at Stony Brook, 1979.
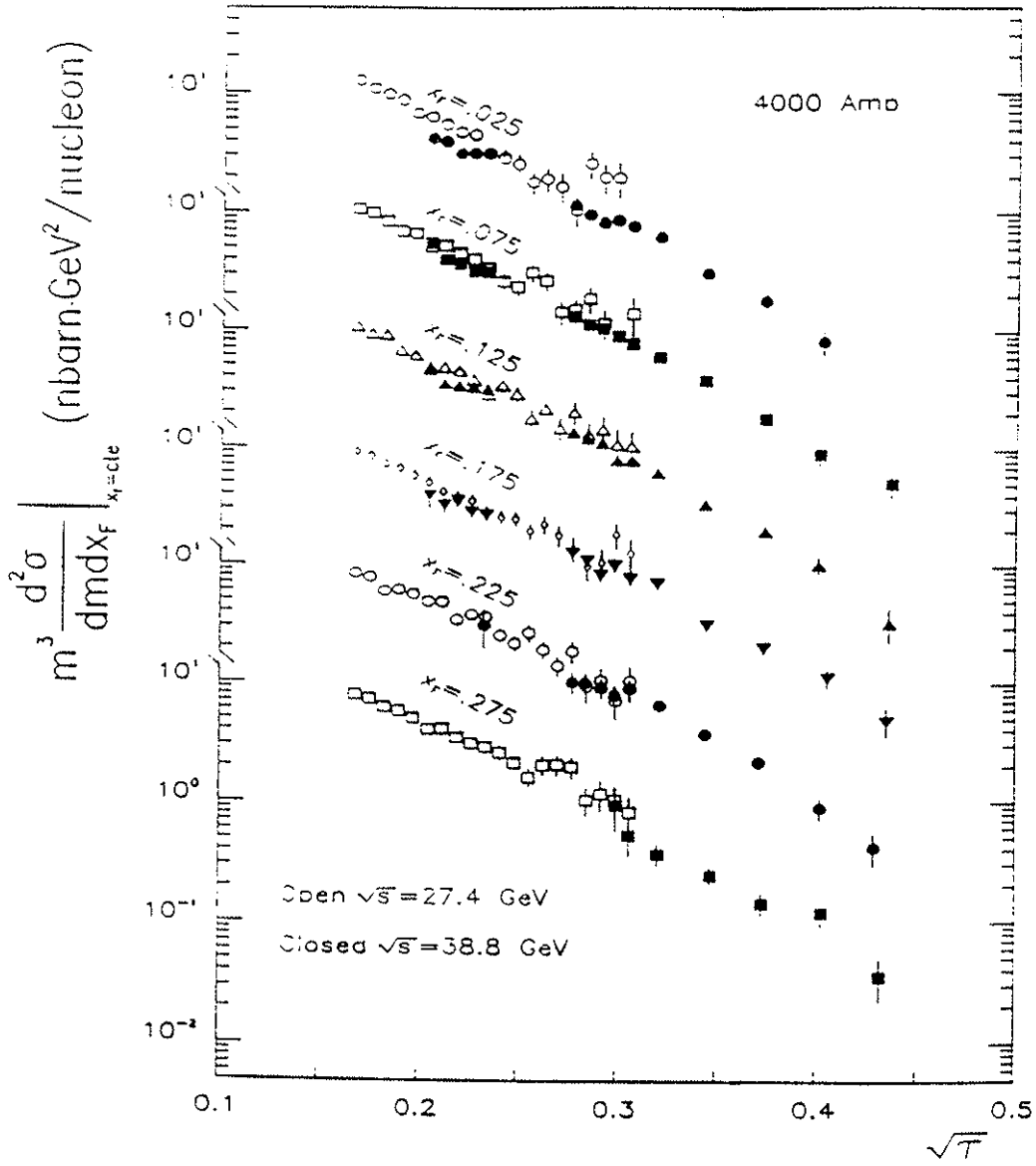
Figure 5.8: Comparison of the cross-section *versus* $\sqrt{\tau}$ at constant x_F for our 4000-*Amp* data and the data of NA3 (J. Badier *et al.*[2]).
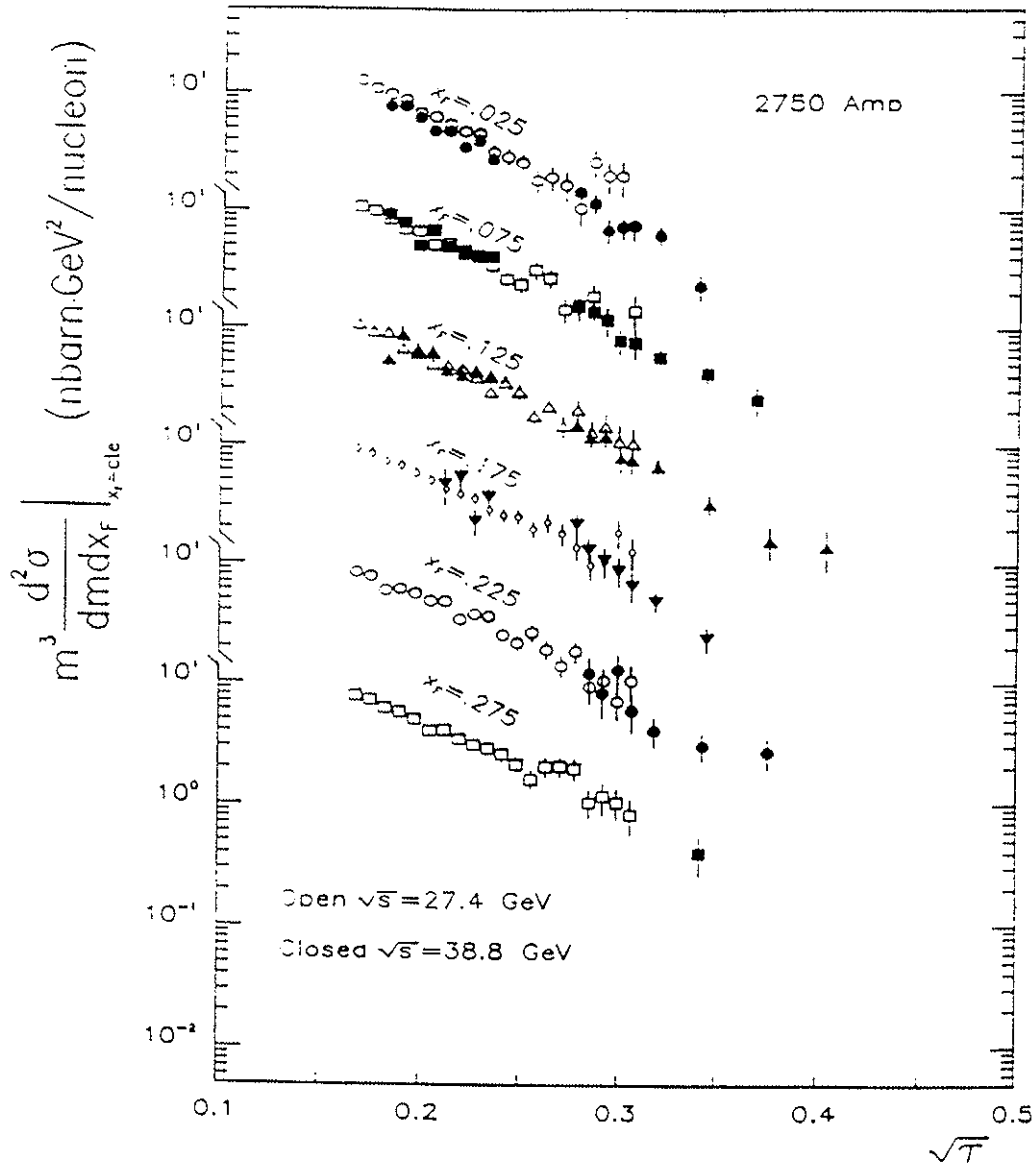
Figure 5.9: Comparison of the cross-section *versus* $\sqrt{\tau}$ at constant x_F for our 2750-*Amp* data and the data of NA3.
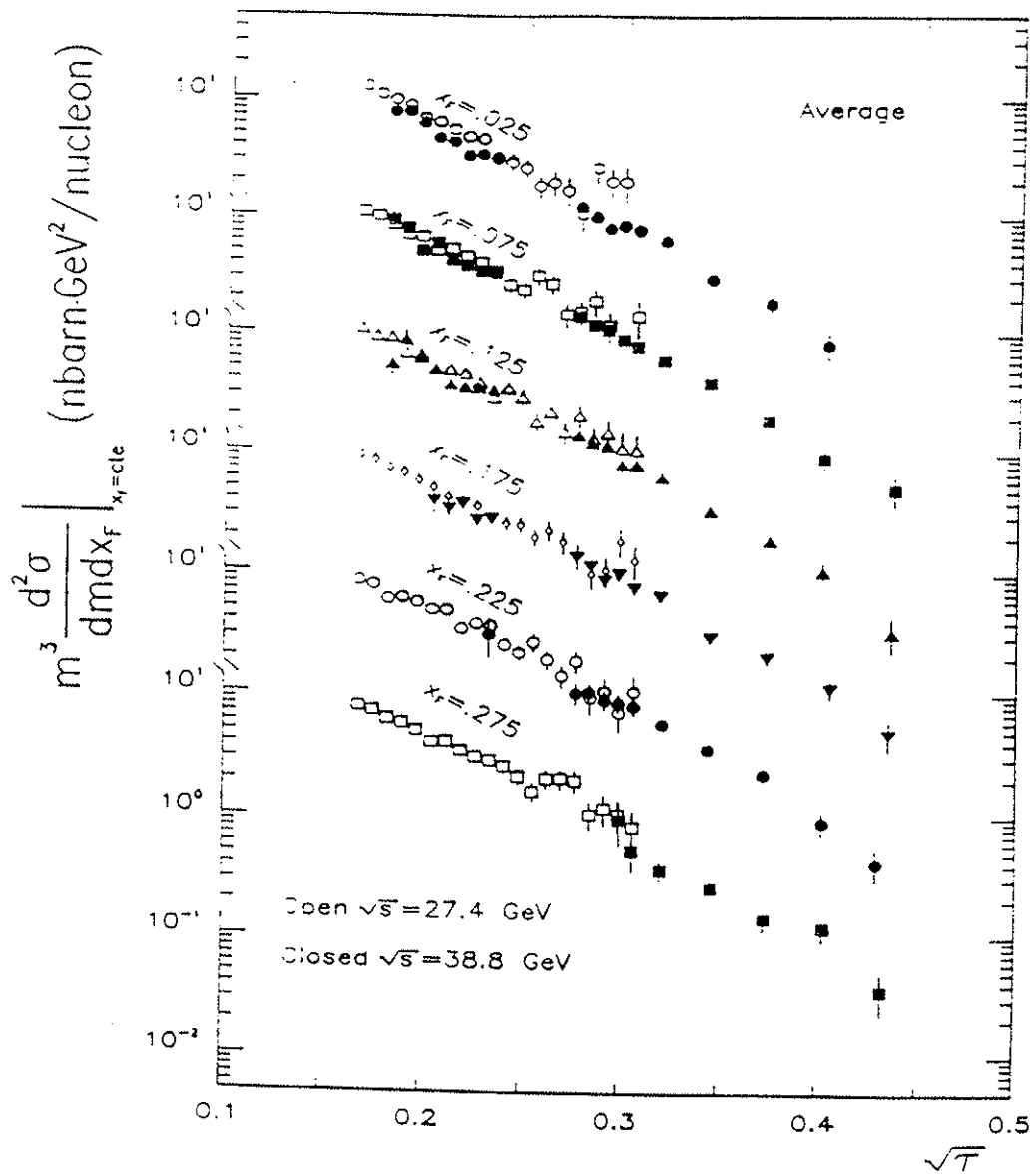
Figure 5.10: Comparison of our averaged data and the data of NA3 for the cross-section *versus* $\sqrt{\tau}$ at constant x_F.

The second observation could be a manifestation of QCD scale violation effects at high $\sqrt{\tau}$. $s\,d^2\sigma/d\sqrt{\tau}dy$ versus $\sqrt{\tau}$ at $y = .2$ is presented in Figure 5.6 and Table 5.3. The average of our two data sets is plotted in Figure 5.7 along with the predicted behavior of the cross-section at two different values of $\sqrt{s}$. The prediction is the next-to-leading order (order α_s) QCD calculation of Martin et al[5]. The dashed line should match the squares (E288 data at $\sqrt{s} = 19.4\,GeV$) and the continuous line the circles (our averaged data at $\sqrt{s} = 38.8\,GeV$). It is apparent that the data falls off more rapidly than the prediction at high $\sqrt{\tau}$, although the systematic error in the data could account for the slight variations observed.

Table 5.4 presents the comparison of our data to that of NA3 in the scaling form $m^3\,d^2\sigma/dmdx_F$ versus $\sqrt{\tau}$ for different x_F bins. This comparison is also shown in Figure 5.8 for the 4000-Amp data, Figure 5.9 for the 2750-Amp data, and Figure 5.10 for the average of the two sets. The NA3 data values quoted here are not the same as the values reported in their paper, because they give $d^2\sigma/dmdx_F$. We took their data and multiplied by the central value of their mass bins to get the above scaling form. There is good agreement between both experiments in the region where the acceptances overlap, except near $\sqrt{\tau} \simeq .3$ where their data is higher than ours (the difference would increase if the nuclear motion correction were removed). Due to the lack of NA3 data at high $\sqrt{\tau}$, the apparent deviation from scaling seen in the E288 comparison is not observed.

Figure 5 of Martin et al.[5] shows a direct comparison of E288 and NA3 in which the NA3 data is above E288 by almost 30%. This is in disagreement with the comparisons presented in this thesis, since our data was independently compared with both experiments and an agreement better than 30% is observed.

Note, not all of our data is used in the above comparisons, only the data that overlaps the bins of E288 and NA3. For the complete set of data from this experiment, see Tables 5.1 to 5.7 in this Chapter.

5.2.2 p_t Distributions

The p_t distributions are usually presented as invariant cross-sections, integrated over a given mass interval, averaged over the azimuthal angle ϕ

[5]A. D. Martin, R. G. Roberts and W. J. Stirling, Phys. Lett. 206B (1988) 327; C. N. Brown, private communication.
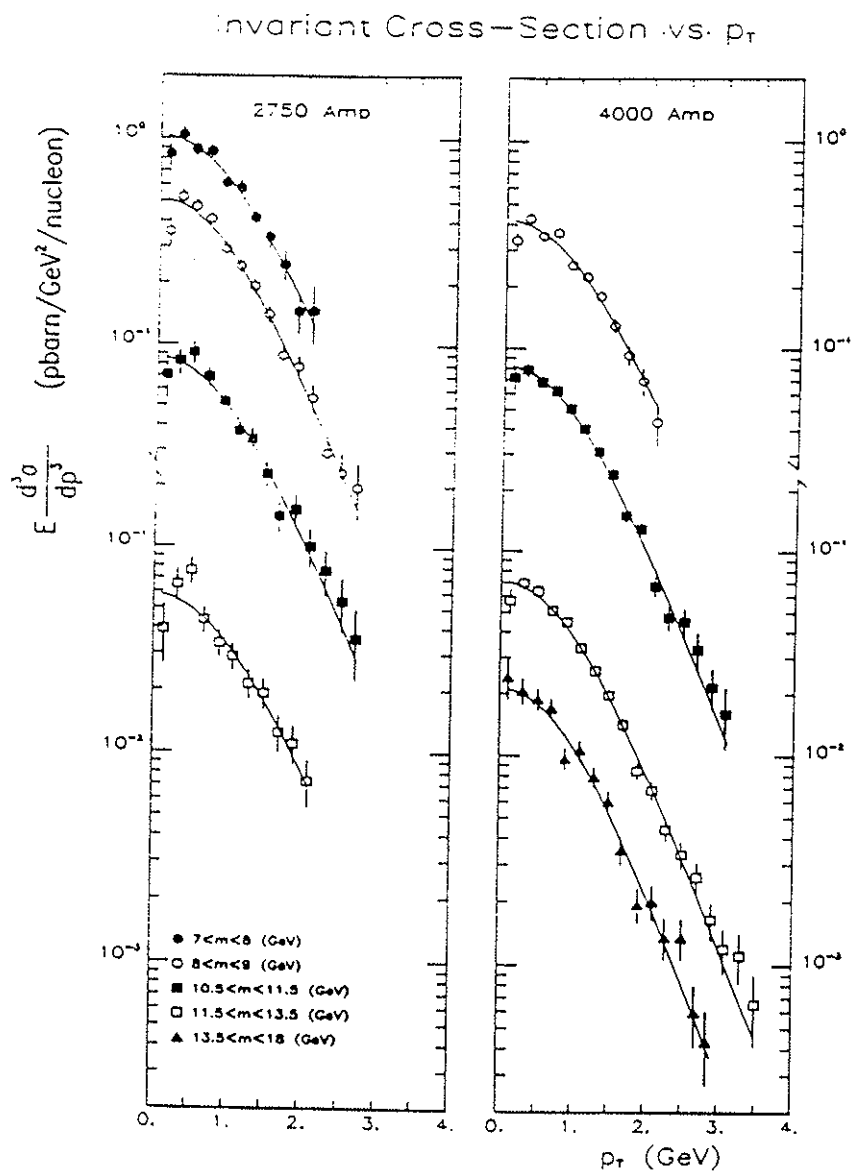
Figure 5.11: Continuum p_t distributions for our two data sets. The lines correspond to the function used to fit the data points.
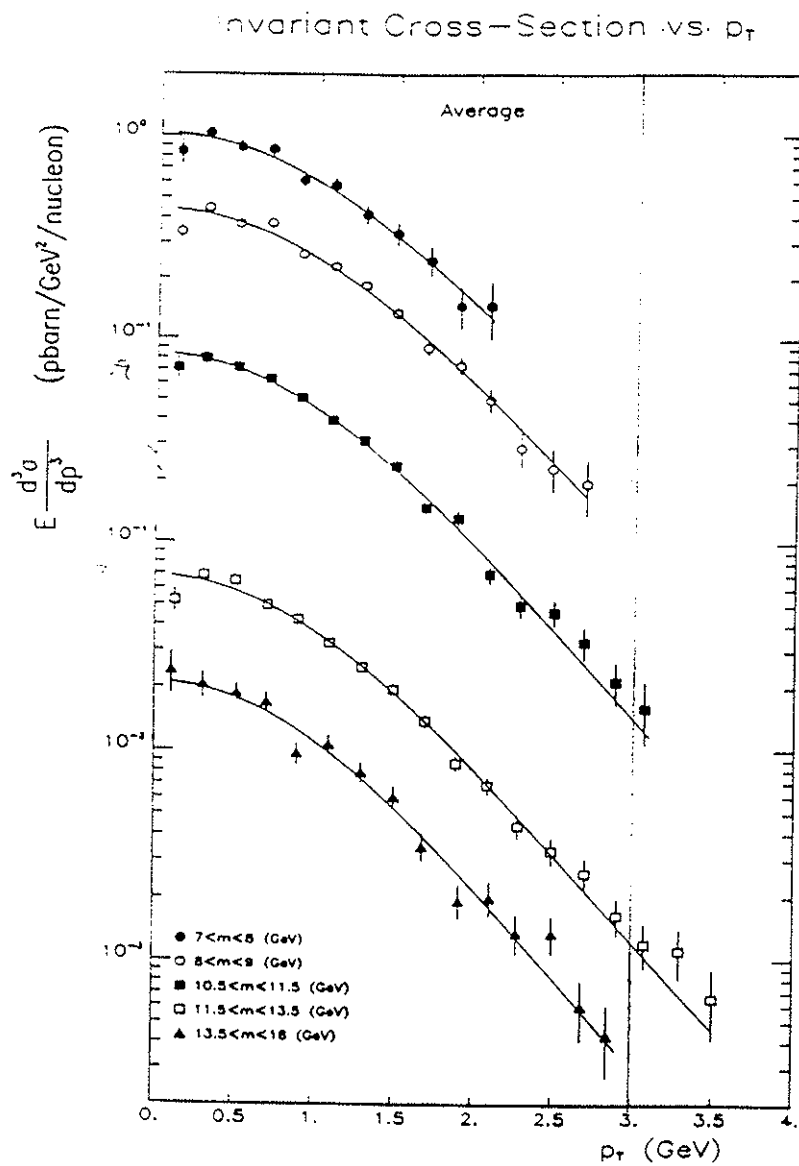
Figure 5.12: Continuum p_t distributions for our averaged data. The lines correspond to the function used to fit the data points.
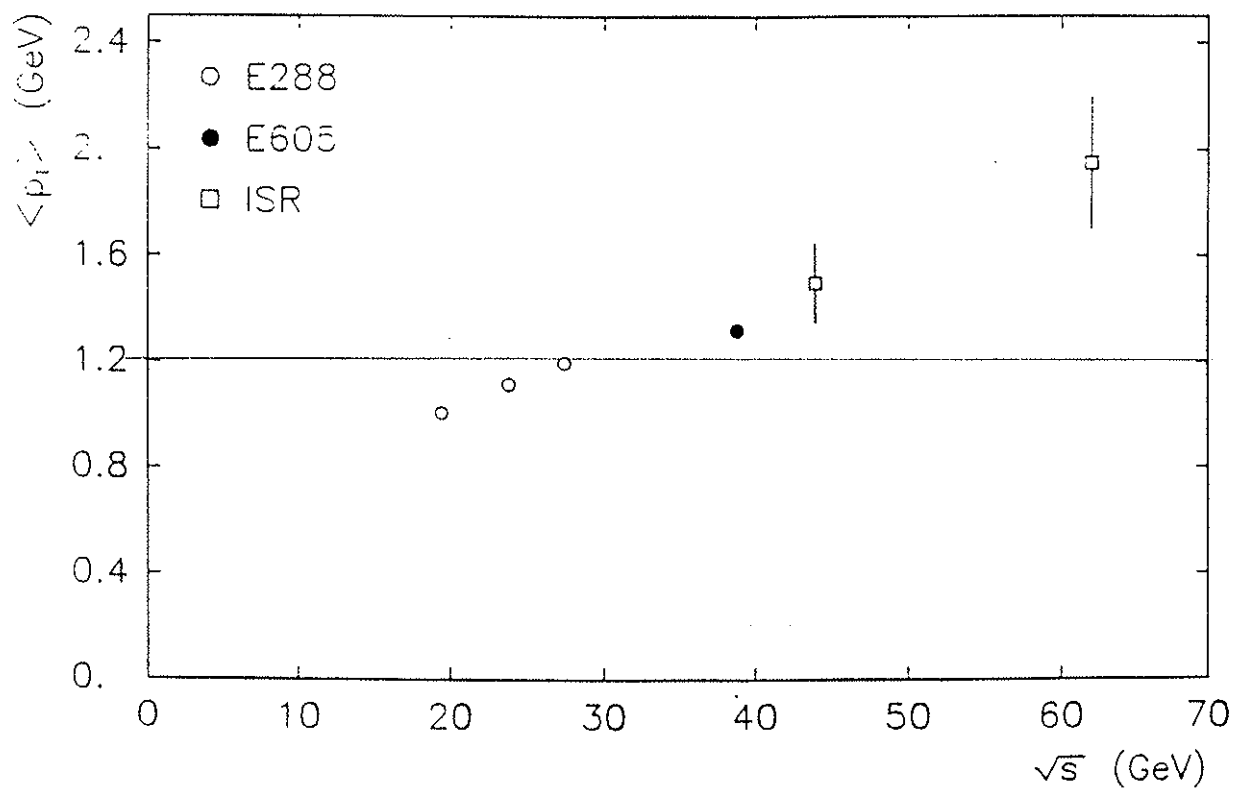
Figure 5.13: Average p_t at $\sqrt{\tau} \simeq .3$ *versus* $\sqrt{s}$ for this experiment. Also shown is E288 and ISR data.

of the dimuon, and integrated over the μ^+ angles in the dimuon CM system; i.e.,

$$\left\langle E\frac{d^3\sigma}{dp^3}\right\rangle \equiv \frac{1}{2\pi}\int_0^{2\pi} d\phi\,(E\frac{d^3\sigma}{dp^3}) = \frac{E}{\pi\sqrt{s}}\frac{d^2\sigma}{p_t\,dp_t\,dx_F} \quad,$$

where the mean values of E and p_t are used to evaluate the last expression.

The x_F bin was defined as the interval $(-.1, .2)$; five mass bins were selected: 7 to 8 GeV, 8 to 9 GeV, 10.5 to 11.5 GeV, 11.5 to 13.5 GeV, and 13.5 to 18 GeV; and equally spaced p_t bins of .2 GeV were chosen. The resulting distributions of the two sets of data are displayed in Table 5.4 and plotted in Figure 5.11. Their average is shown in Figure 5.12. Each of the p_t distributions were fit with the function[6] $A/[1 + (p_t/p_0)^2]^6$, which is superimposed on those figures. The fit parameters and mean p_t ($\langle p_t\rangle$) are given in Table 5.6. Figure 5.13 shows $\langle p_t\rangle$ together with results from other experiments[7] as a function of $\sqrt{s}$ for a constant $\sqrt{\tau} = .3$. The observed increase of $\langle p_t\rangle$ with $\sqrt{s}$ is one of the most celebrated predictions of QCD[8], in which one of the colliding quarks radiates a hard gluon and acquires a large p_t.

5.3 Upsilon Cross-Sections

5.3.1 x_F Dependence

To study the x_F dependence of the Upsilon cross-section, the raw data was divided into several x_F bins, $\Delta x_F = .05$, and the resulting mass spectrum for each bin was then fit with the sum of four functions. One function represented the 'raw' Drell-Yan yield (N_{raw}^{DY}), and the others the corresponding i^{th} Upsilon yield ($U_{raw}^{\Upsilon_i}$). Assuming an exponentially falling function for the Drell-Yan production cross-section, $d^2\sigma/dm\,dx_F \approx e^{-\alpha m}$, its contribution to the yield observed in $\Delta m\Delta x_F$ is

$$N_{raw}^{DY}(m) = (\Delta m\Delta x_F) \times [L_{corr}\epsilon(m)a(m)] \times [De^{-\alpha(m-m_\Upsilon)}] \quad.$$

---

[6]D. M. Kaplan *et al.*, Phys. Rev. Lett. **40** (1978) 435.

[7]The data points below ours correspond to E288 as reported by J. K. Yoh *et al.*, Phys. Rev. Lett. **41** (1978) 684; and the ones above ours are ISR data from D. Antreasyan *et al.*, Phys. Rev. Lett. **47** (1981) 12.

[8]H. Fritzsch and P. Minkowski, Phys. Lett. **73B** (1978) 80; G. Altarelli, G. Parisi, and R. Petronzio, Lett. **76B** (1978) 351; **76B** (1978) 356.
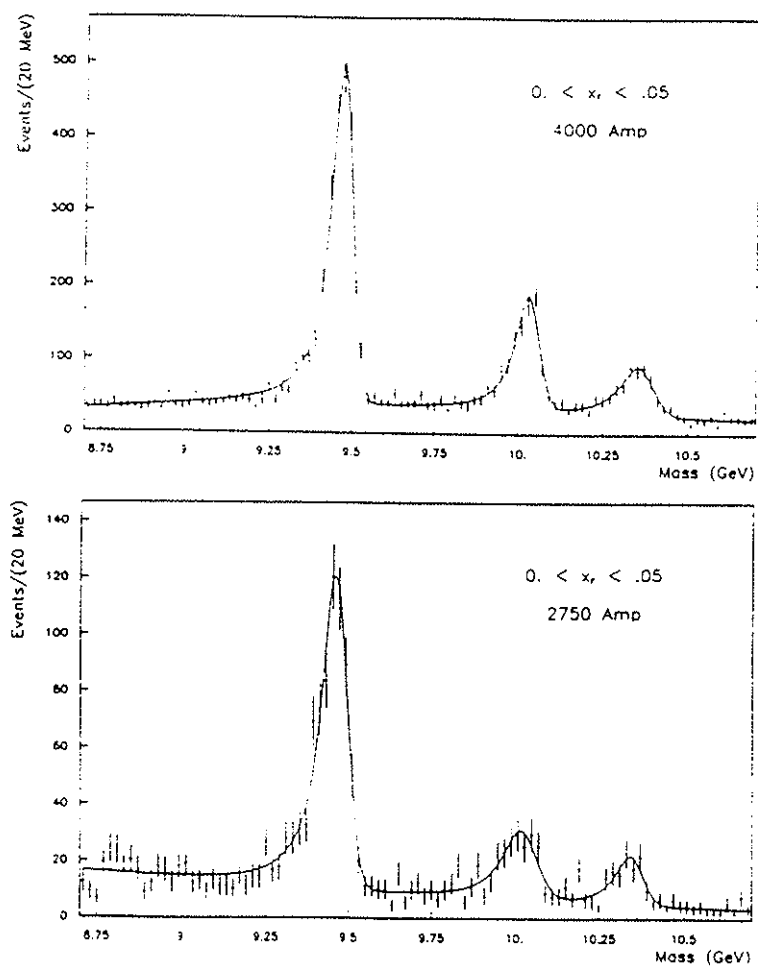
Figure 5.14: The fit function (described in the text) is superimposed on the raw spectrum in the Upsilon region.
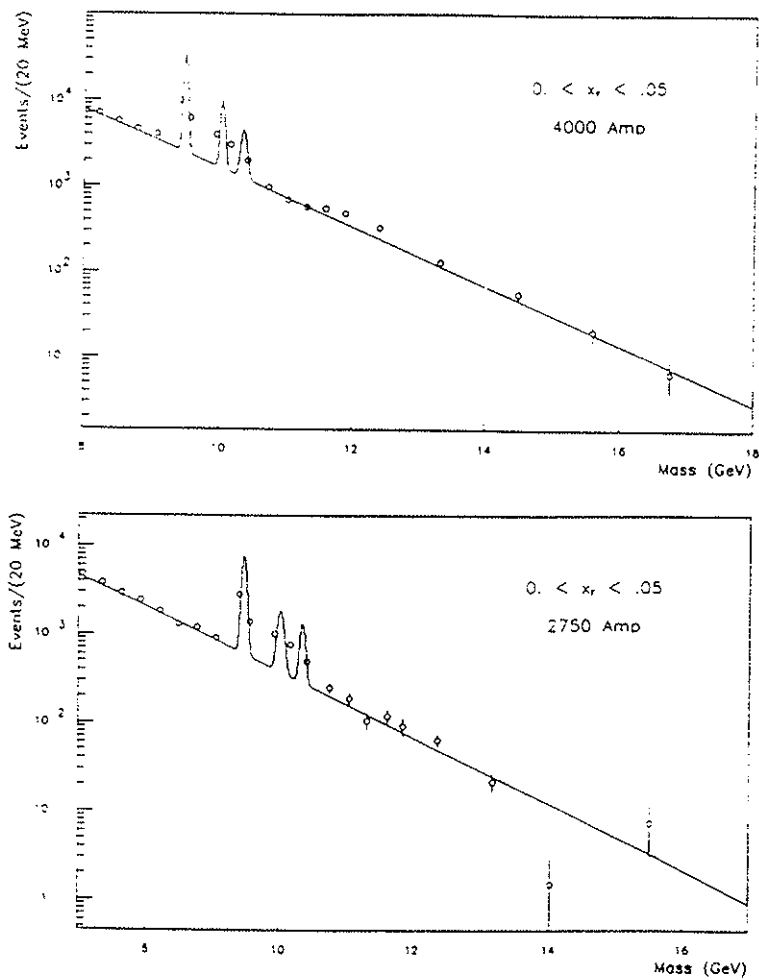
Figure 5.15: The acceptance corrected spectrum along with the fit function described in the text after rebinning the data in the Upsilon region. The acceptance correction is for the continuum only.

where the different factors are: the Drell-Yan acceptance $[a(m)]$, the efficiency $[\epsilon(m)]$, and the luminosity $[L_{corr}]$. The parameter D gives the Drell-Yan cross-section evaluated at the Upsilon mass m_Υ. The 'raw' yield of the ith Upsilon was parametrized as a Gaussian function on one side of the peak, and a Lorentzian function that simulated the asymmetry of the other side:

$$
U_{raw}^{\Upsilon_i}(m) = N_i \begin{cases} \frac{1}{1+[(m-m_i)/(1.5\sigma_i)]^2} & \text{if } m < m_i \\[2mm] e^{-.5[(m-m_i)/(\sigma_i)]^2} & \text{if } m > m_i \end{cases} \quad .
$$

In total, the parameters numbered 11: the exponential slope, α, and the overall normalization, D, of the continuum; and three parameters for each of the three Upsilons, describing the normalization (N_i), position (m_{Υ_i}), and width (σ_i) of the peak. Figure 5.14 shows the fit function in the Upsilon region for $0 < x_F < .05$. The corresponding full spectrum is shown in Figure 5.15, after rebinning the data in the Upsilon region and correcting for the continuum acceptance. The 'raw' number of Upsilons was finally calculated by integrating the functions $U_{raw}^{\Upsilon_i}(m)$ over
$m_{\Upsilon_i} - 1 < m < m_{\Upsilon_i} + 1 \ (GeV)$.

Figure 5.16 and Table 5.7 show the production cross-section times the branching ratio to muon pairs, $Bd\sigma/dx_F$, for each one of the Upsilons near $x_F = 0$. The ratios of the corresponding cross-sections for Υ'/Υ and Υ''/Υ are shown in Figure 5.17 and Table 5.8 together with the Upsilon to continuum ratio defined[9] as

$$
R_\Upsilon = \sum_{V = \Upsilon, \Upsilon', \Upsilon''} \frac{B(V \to l^+l^-)\frac{d\sigma}{dx_F}(pN \to VX)}{\frac{d^2\sigma}{dmdx_F}(pN \to l^+l^-X)\Big|_{m=m_\Upsilon}} \quad .
$$

These quantities have been measured using our 1984 electron[10] and muon[11] data and are also shown in the corresponding plots. Since the electron data was calculated as $d\sigma/dy$, the approximation $x_F \simeq 2\sqrt{\tau}y$ was used to obtain the values plotted at $x_F = 0$. In general, there is good agreement among the different measurements with the same spectrometer, although $Bd\sigma/dx_F$ for the 2750-Amp data is about 20% higher than the value obtained with the

---

[9]S. Childress *et al.*, Phys. Rev. Lett. **55** (1985) 1962.

[10]T. Yoshida, Ph. D. Thesis, Kyoto University, 1986; submitted to PRL.

[11]R. Gray, Ph. D. Thesis, University of Washington, 1988.
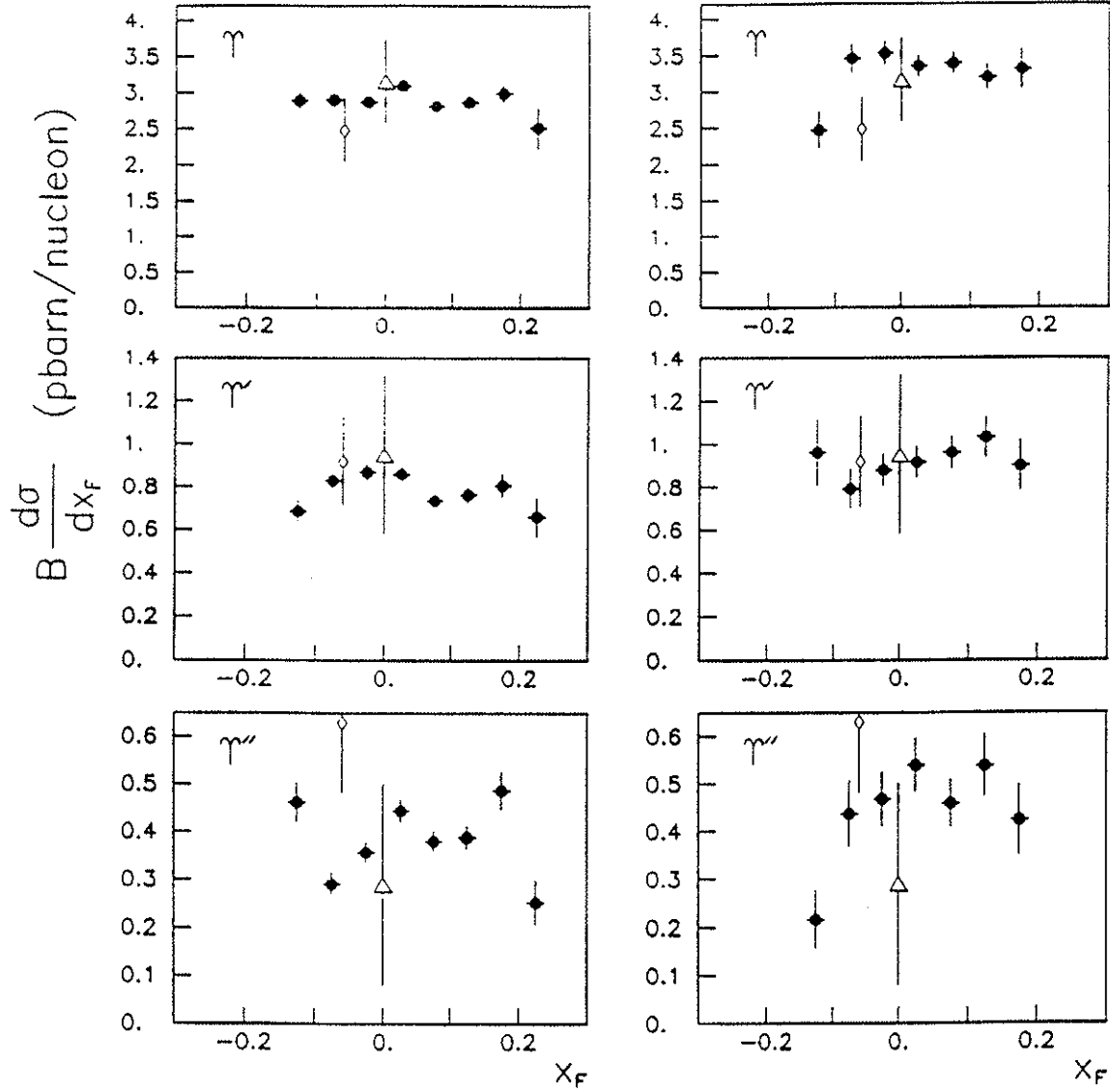
Figure 5.16: The Upsilon production cross-section times the branching ratio to muon pairs *versus* x_F. The diamonds correspond to our 1984 muon data[11] and the triangles are from our 1984 electron data[10].

Figure 5.17: The Upsilon to continuum ratio R_Υ (denoted by R on the upper plots), and the relative ratio to Υ for Υ' and Υ'' as a function of x_F. The diamonds correspond to our 1984 muon data[11] and the triangles are from our 1984 electron data[10].

4000-*Amp* data. This discrepancy could be accounted for by allowing the fit parameters to take the extreme values, as provided by the fit errors, and then repeating the calculation of the cross-section. The difference of both calculations (extreme - normal values) gives an estimate of the systematic error introduced by the fitting procedure itself. This is the second error shown in the cross-sections reported in Table 5.7.

It is interesting to observe that $B d\sigma/dx_F$ seems to be independent of x_F in the range shown, in contrast to the continuum cross-section which has a positive slope near $x_F = 0$ (or $y = 0$), as shown in Figure 5.5. This difference gives support to the idea that Upsilon and Drell-Yan production are realized through different production mechanisms. Assuming that Upsilon production is due to the strong interactions of quarks and gluons and invoking isospin symmetry among nucleons, the Upsilon production cross-section in p-n collisions should be symmetric about $x_F = 0$.

5.3.2 p_t Dependence

The p_t distribution for Upsilons was extracted from data in the mass ranges: $9.36 < m < 9.54\,GeV$ (Υ), $9.92 < m < 10.12\,GeV$ (Υ'), and $10.26 < m < 10.48\,GeV$ (Υ''). The x_F range considered was $-.1 < x_F < .2$, and an appropriate continuum subtraction was carried out. The expected number of Drell-Yan events under the peaks was calculated using the continuum parameters of the fits described above. The continuum subtraction was performed independently for each Upsilon distribution, such that it then allowed each distribution to be corrected for the appropriate acceptance. After the continuum subtraction, the 'raw' number of Upsilons ($\Upsilon + \Upsilon' + \Upsilon''$) in the 4000-*Amp* [2750-*Amp*] data set was found to be 13590 [3376].

The subtraction was done on a bin-to-bin basis using 1) Monte Carlo data, and 2) raw data from the neighboring regions ($8 < m < 9\,GeV$ and $10.6 < m < 11\,GeV$). Both procedures yielded the same result (within .1%) for the 2750-*Amp* data, while they showed a discrepancy of about 2% in the high p_t bins of the 4000-*Amp* data. This discrepancy is due to the difference in acceptance for the data in the neighboring bins, which is not seen in the 2750-*Amp* data. The results presented here correspond to the Monte Carlo subtraction.

Figure 5.18 shows the invariant cross-section *versus* p_t for the two data sets, along with fits similar to the ones done for the continuum data. The fit
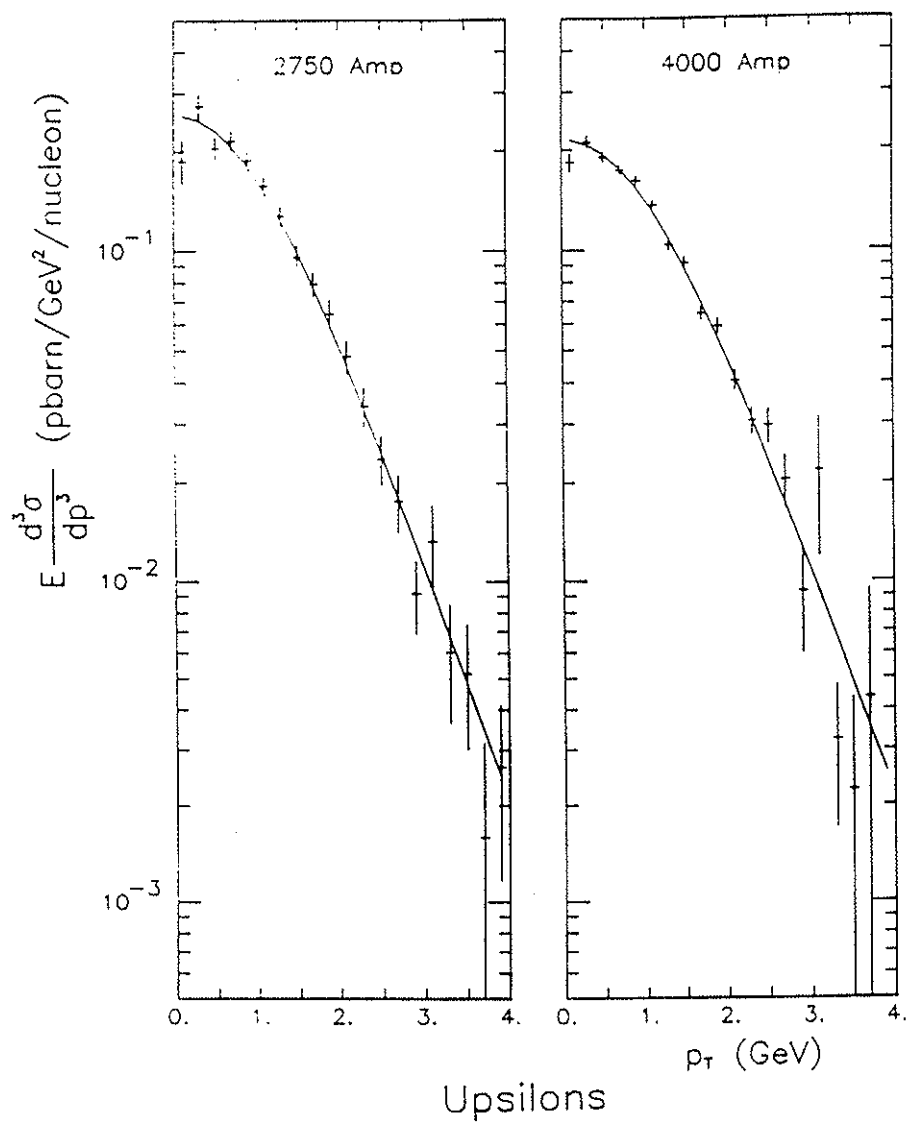
Figure 5.18: Upsilon p_t distributions after continuum subtraction. The lines correspond to the function used to fit the data points.

results and cross-sections are tabulated together with the continuum results in Table 5.6 and Table 5.4, respectively. It is important to remark that the Upsilon $\langle p_t \rangle$ is indeed larger than the continuum $\langle p_t \rangle$. As commented in Section 1.2, if hadronic production of Upsilons is realized through gluon amalgamation (either direct production or radiative χ_b decays), the Upsilons are produced with large p_t due to the recoil against the gluon in the final state. Therefore, this provides more evidence to support the idea of gluon-gluon interactions being responsible for hadroproduction of Upsilons.

5.4   Conclusions

The two measurements of dimuon production in proton-Copper collisions at $\sqrt{s} = 38.8\, GeV$ presented in this thesis have shown the following:

1. The first three Υ states are clearly seen in the mass spectrum with a mass resolution (FWHM) of about $80\, MeV$ at $m = 9.46\, GeV$.

2. No new statistically significant resonances are seen in the mass spectrum from 6.5 to 18 GeV.

3. The scaling prediction of the Drell-Yan model has been tested to about 20% by comparing our results to those of previous experiments, E288 and NA3, at lower energies ($\sqrt{s} = 19.4, 23.8,$ and $24.7\ GeV$).

4. The positive slope of $sd^2\sigma/d\sqrt{\tau}dy$ versus y at $y = 0$ and constant $\sqrt{\tau}$ is due to the presence of neutrons in the target and may yield information on a possible asymmetry of the $\bar{u}$ and $\bar{d}$ sea in protons and neutrons.

5. Our data lies below that of E288 for $\sqrt{\tau} > .3$. This can be explained by QCD corrections to the Drell-Yan model. Furthermore, QCD predictions are in excellent agreement with the measured cross-sections.

6. The p_t distributions for the continuum appear to be mass independent. Comparing with mean p_t values from other experiments, $\langle p_t \rangle$ grows linearly with $\sqrt{s}$, as predicted by QCD.

7. The Upsilon x_F and p_t distributions exhibit strong differences from those of the continuum, indicating a different production mechanism.

Table 5.1: Comparison of the cross-section $s\frac{d^2\sigma}{d\sqrt{\tau}dy}$ *versus* rapidity at constant $\sqrt{\tau}$ with the data of E288. The format is: rapidity, cross-section, and error. Units are $nbarn \cdot GeV^2/nucleon$. (Note, the data of E288 have been corrected for Fermi motion).

$.185 < \sqrt{\tau} < .211$		
E288 ($\sqrt{s} = 27.4\,GeV$)		
-0.189	.259E+03	.280E+02
-0.099	.288E+03	.110E+02
0.021	.286E+03	.800E+01
0.141	.320E+03	.800E+01
0.231	.337E+03	.170E+02
2750-*Amp* ($\sqrt{s} = 38.8\,GeV$)		
-0.396	.212E+03	.402E+02
-0.291	.278E+03	.351E+02
-0.197	.212E+03	.182E+02
-0.098	.277E+03	.193E+02
0.000	.289E+03	.185E+02
0.100	.329E+03	.209E+02
0.198	.341E+03	.234E+02
0.292	.380E+03	.361E+02
$.30 < \sqrt{\tau} < .33$		
E288 ($\sqrt{s} = 19.4\,GeV$)		
0.180	.189E+02	.900E+00
0.270	.191E+02	.100E+01
0.390	.160E+02	.160E+01
E288 ($\sqrt{s} = 23.8\,GeV$)		
-0.060	.111E+02	.320E+01
0.030	.146E+02	.150E+01
0.150	.176E+02	.120E+01
0.270	.163E+02	.110E+01
0.360	.194E+02	.230E+01
E288 ($\sqrt{s} = 27.4\,GeV$)		
-0.180	.127E+02	.900E+00
-0.090	.127E+02	.400E+00
0.030	.133E+02	.300E+00
0.150	.146E+02	.400E+00
0.240	.151E+02	.800E+00

Table 5.1 (continued)

2750-$Amp(\sqrt{s} = 38.8\,GeV)$		
-0.184	.845E+01	.378E+01
-0.088	.927E+01	.182E+01
0.013	.134E+02	.173E+01
0.100	.131E+02	.160E+01
0.199	.141E+02	.166E+01
0.294	.149E+02	.197E+01
0.390	.112E+02	.278E+01
4000-$Amp(\sqrt{s} = 38.8\,GeV)$		
-0.288	.103E+02	.196E+01
-0.190	.960E+01	.962E+00
-0.093	.122E+02	.812E+00
0.003	.144E+02	.717E+00
0.100	.145E+02	.684E+00
0.200	.156E+02	.788E+00
0.292	.151E+02	.959E+00
0.383	.146E+02	.161E+01

$.33 < \sqrt{\tau} < .39$

E288 $(\sqrt{s} = 19.4\,GeV)$		
0.183	.712E+01	.119E+01
0.273	.620E+01	.490E+00
0.393	.683E+01	.360E+00
E288 $(\sqrt{s} = 23.8\,GeV)$		
-0.057	.472E+01	.144E+01
0.033	.514E+01	.590E+00
0.153	.607E+01	.460E+00
0.273	.601E+01	.490E+00
0.363	.548E+01	.810E+00
2750-Amp $(\sqrt{s} = 38.8\,GeV)$		
-0.173	.375E+01	.282E+01
-0.090	.305E+01	.955E+00
-0.011	.331E+01	.636E+00
0.109	.525E+01	.657E+00
0.193	.356E+01	.510E+00
0.301	.416E+01	.666E+00
0.384	.335E+01	.104E+01

Table 5.1 (continued)

4000-Amp ($\sqrt{s} = 38.8\,GeV$)		
-0.274	.294E+01	.112E+01
-0.184	.264E+01	.416E+00
-0.094	.420E+01	.340E+00
0.003	.404E+01	.256E+00
0.101	.454E+01	.240E+00
0.198	.472E+01	.264E+00
0.297	.462E+01	.319E+00
0.390	.415E+01	.468E+00

$.39 < \sqrt{\tau} < .45$

E288 ($\sqrt{s} = 19.4\,GeV$)		
0.190	.129E+01	.350E+00
0.280	.116E+01	.140E+00
0.600	.780E+00	.900E−01
E288 ($\sqrt{s} = 27.4\,GeV$)		
-0.170	.700E+00	.100E+00
-0.080	.100E+01	.600E−01
0.040	.101E+01	.500E−01
0.160	.113E+01	.600E−01
0.250	.960E+00	.120E+00
2750-Amp ($\sqrt{s} = 38.8\,GeV$)		
-0.002	.100E+01	.505E+00
0.095	.832E+00	.296E+00
0.195	.960E+00	.268E+00
0.281	.607E+00	.249E+00
0.604	.117E+01	.529E+00
4000-Amp ($\sqrt{s} = 38.8\,GeV$)		
-0.090	.627E+00	.175E+00
0.004	.712E+00	.121E+00
0.107	.866E+00	.107E+00
0.196	.902E+00	.109E+00
0.298	.983E+00	.134E+00
0.379	.556E+00	.155E+00

Table 5.2: $s\frac{d^2\sigma}{d\sqrt{\tau}dy}$ versus $\sqrt{\tau}$ at $y = .2$. The first number is the cross-section and the second is the error. The data with the lower $\sqrt{s}$ correspond to the data of E288. Units are $nbarn \cdot GeV^2/nucleon$. (Note, the data of E288 have been corrected for Fermi motion).

$\sqrt{\tau}$	2750-Amp		4000-Amp		Average	
.177	.603E+03	.707E+02			.603E+03	.707E+02
.197	.341E+03	.234E+02			.341E+03	.234E+02
.222	.177E+03	.117E+02	.147E+03	.554E+01	.152E+03	.501E+01
.283	.313E+02	.257E+01	.315E+02	.133E+01	.314E+02	.118E+01
.313	.141E+02	.166E+01	.156E+02	.788E+00	.153E+02	.712E+00
.352	.356E+01	.510E+00	.472E+01	.264E+00	.447E+01	.234E+00
.411	.960E+00	.268E+00	.902E+00	.109E+00	.910E+00	.101E+00
.457			.409E+00	.167E+00	.409E+00	.167E+00
	$\sqrt{s} = 19.4\,GeV$		$\sqrt{s} = 23.8\,GeV$		$\sqrt{s} = 27.4\,GeV$	
.198					.337E+03	.170E+02
.229			.148E+03	.600E+01	.140E+03	.700E+01
.273	.458E+02	.260E+01	.464E+02	.170E+01	.445E+02	.130E+01
.315	.191E+02	.400E+00	.163E+02	.110E+01	.151E+02	.800E+00
.357	.620E+01	.490E+00	.601E+01	.490E+00		
.414	.129E+01	.350E+00			.960E+00	.120E+00
.473			.247E+00	.670E-01	.182E+00	.490E-01

Table 5.3: $m^3 \frac{d^2\sigma}{dmdx_F}$ versus x_F and $\sqrt{\tau}$ for this experiment and the NA3 experiment. The first number is the cross-section and the second is the error. Units are $nbarn \cdot GeV^2/nucleon$. (Note, the data of NA3 have been corrected for Fermi motion).

$x_F = -.125$						
$\sqrt{\tau}$	4000-Amp		2750-Amp		Average	
.183			.938E+01	.346E+01	.938E+01	.346E+01
.190			.536E+01	.130E+01	.536E+01	.130E+01
.197			.472E+01	.109E+01	.472E+01	.109E+01
.204			.429E+01	.901E+00	.429E+01	.901E+00
.212			.342E+01	.607E+00	.342E+01	.607E+00
.219			.448E+01	.843E+00	.448E+01	.843E+00
.226	.186E+01	.367E+00	.368E+01	.634E+00	.232E+01	.318E+00
.234	.267E+01	.360E+00	.355E+01	.675E+00	.287E+01	.318E+00
.277	.940E+00	.140E+00			.940E+00	.140E+00
.285	.106E+01	.163E+00			.106E+01	.163E+00
.292	.804E+00	.144E+00			.804E+00	.144E+00
.299	.392E+00	.827E-01			.392E+00	.827E-01
.307	.462E+00	.102E+00			.462E+00	.102E+00
.320	.411E+00	.587E-01			.411E+00	.587E-01
.343	.232E+00	.446E-01			.232E+00	.446E-01
.374	.187E+00	.485E-01			.187E+00	.485E-01

$x_F = -.075$						
$\sqrt{\tau}$	4000-Amp		2750-Amp		Average	
.182			.607E+01	.127E+01	.607E+01	.127E+01
.190			.427E+01	.655E+00	.427E+01	.655E+00
.197			.519E+01	.706E+00	.519E+01	.706E+00
.204			.309E+01	.395E+00	.309E+01	.395E+00
.212	.258E+01	.993E+00	.441E+01	.558E+00	.397E+01	.487E+00
.219	.233E+01	.435E+00	.332E+01	.402E+00	.286E+01	.295E+00
.226	.312E+01	.343E+00	.369E+01	.491E+00	.331E+01	.281E+00
.234	.308E+01	.266E+00	.321E+01	.443E+00	.312E+01	.228E+00
.277	.114E+01	.132E+00	.878E+00	.223E+00	.108E+01	.114E+00
.284	.856E+00	.976E-01	.742E+00	.227E+00	.838E+00	.897E-01
.292	.862E+00	.106E+00	.954E+00	.271E+00	.874E+00	.990E-01
.299	.786E+00	.103E+00			.786E+00	.103E+00
.306	.640E+00	.102E+00			.640E+00	.102E+00
.320	.485E+00	.492E-01	.464E+00	.128E+00	.482E+00	.459E-01
.344	.337E+00	.396E-01			.337E+00	.396E-01
.374	.131E+00	.292E-01			.131E+00	.292E-01
.399	.704E-01	.268E-01			.704E-01	.268E-01

Table 5.3 (continued)

$x_F = -.025$						
$\sqrt{\tau}$	4000-Amp		2750-Amp		Average	
.183			.710E+01	.107E+01	.710E+01	.107E+01
.190			.765E+01	.991E+00	.765E+01	.991E+00
.197			.444E+01	.472E+00	.444E+01	.472E+00
.204			.490E+01	.519E+00	.490E+01	.519E+00
.212	.403E+01	.656E+00	.501E+01	.524E+00	.463E+01	.409E+00
.219	.377E+01	.384E+00	.529E+01	.560E+00	.426E+01	.317E+00
.226	.309E+01	.251E+00	.377E+01	.398E+00	.328E+01	.212E+00
.234	.329E+01	.218E+00	.352E+01	.370E+00	.335E+01	.188E+00
.277	.123E+01	.113E+00	.156E+01	.259E+00	.128E+01	.104E+00
.284	.124E+01	.117E+00	.106E+01	.213E+00	.120E+01	.103E+00
.292	.753E+00	.782E−01	.107E+01	.212E+00	.791E+00	.734E−01
.299	.798E+00	.860E−01	.962E+00	.254E+00	.815E+00	.815E−01
.306	.780E+00	.900E−01	.467E+00	.162E+00	.706E+00	.786E−01
.320	.626E+00	.468E−01	.491E+00	.105E+00	.603E+00	.428E−01
.343	.357E+00	.337E−01	.334E+00	.973E−01	.355E+00	.318E−01
.376	.141E+00	.254E−01			.141E+00	.254E−01
.404	.764E−01	.222E−01			.764E−01	.222E−01

Table 5.3 (continued)

$x_F = 0.025$						
$\sqrt{\tau}$	4000-Amp		2750-Amp		Average	
.182			.774E+01	.960E+00	.774E+01	.960E+00
.190			.776E+01	.925E+00	.776E+01	.925E+00
.197			.623E+01	.686E+00	.623E+01	.686E+00
.204	.421E+01	.638E+00	.481E+01	.468E+00	.460E+01	.377E+00
.212	.393E+01	.363E+00	.480E+01	.479E+00	.425E+01	.290E+00
.219	.316E+01	.235E+00	.349E+01	.349E+00	.327E+01	.195E+00
.226	.318E+01	.212E+00	.400E+01	.402E+00	.336E+01	.188E+00
.233	.318E+01	.184E+00	.275E+01	.278E+00	.305E+01	.153E+00
.277	.116E+01	.944E−01	.144E+01	.218E+00	.121E+01	.866E−01
.285	.965E+00	.862E−01	.116E+01	.198E+00	.997E+00	.791E−01
.292	.829E+00	.781E−01	.684E+00	.151E+00	.799E+00	.694E−01
.299	.878E+00	.837E−01	.737E+00	.164E+00	.849E+00	.746E−01
.307	.771E+00	.762E−01	.757E+00	.193E+00	.769E+00	.709E−01
.320	.632E+00	.420E−01	.625E+00	.108E+00	.631E+00	.391E−01
.344	.312E+00	.266E−01	.233E+00	.584E−01	.298E+00	.242E−01
.374	.183E+00	.240E−01			.183E+00	.240E−01
.402	.829E−01	.192E−01			.829E−01	.192E−01
$\sqrt{\tau}$	NA3 ($\sqrt{s} = 27.4\,GeV$)					
.168	.127E+02	.662E+00				
.175	.108E+02	.630E+00				
.182	.975E+01	.637E+00				
.190	.872E+01	.633E+00				
.197	.677E+01	.535E+00				
.204	.632E+01	.562E+00				
.212	.546E+01	.546E+00				
.219	.475E+01	.518E+00				
.226	.453E+01	.548E+00				
.234	.315E+01	.446E+00				
.241	.287E+01	.460E+00				
.248	.258E+01	.440E+00				
.255	.182E+01	.377E+00				
.263	.194E+01	.448E+00				
.270	.166E+01	.446E+00				
.277	.105E+01	.303E+00				
.285	.261E+01	.664E+00				
.292	.200E+01	.563E+00				
.299	.198E+01	.662E+00				

Table 5.3 (continued)

$x_F = 0.075$						
$\sqrt{\tau}$	4000-Amp		2750-Amp		Average	
.182			.917E+01	.133E+01	.917E+01	.133E+01
.190			.781E+01	.958E+00	.781E+01	.958E+00
.197			.506E+01	.529E+00	.506E+01	.529E+00
.204	.546E+01	.515E+00	.679E+01	.775E+00	.587E+01	.429E+00
.212	.401E+01	.275E+00	.490E+01	.522E+00	.420E+01	.244E+00
.219	.369E+01	.230E+00	.429E+01	.439E+00	.382E+01	.204E+00
.226	.324E+01	.193E+00	.412E+01	.430E+00	.339E+01	.176E+00
.233	.313E+01	.178E+00	.406E+01	.415E+00	.327E+01	.163E+00
.277	.134E+01	.113E+00	.160E+01	.229E+00	.139E+01	.101E+00
.285	.114E+01	.102E+00	.140E+01	.221E+00	.119E+01	.929E−01
.292	.106E+01	.938E−01	.120E+01	.208E+00	.108E+01	.855E−01
.299	.917E+00	.866E−01	.799E+00	.189E+00	.897E+00	.788E−01
.306	.792E+00	.817E−01	.762E+00	.203E+00	.788E+00	.758E−01
.320	.613E+00	.410E−01	.581E+00	.959E−01	.608E+00	.377E−01
.343	.386E+00	.288E−01	.425E+00	.759E−01	.391E+00	.269E−01
.373	.184E+00	.219E−01	.253E+00	.669E−01	.191E+00	.208E−01
.401	.925E−01	.180E−01			.925E−01	.180E−01
.437	.519E−01	.144E−01			.519E−01	.144E−01
$\sqrt{\tau}$	NA3 ($\sqrt{s} = 27.4\,GeV$)					
.168	.107E+02	.545E+00				
.175	.984E+01	.531E+00				
.182	.838E+01	.500E+00				
.190	.689E+01	.478E+00				
.197	.661E+01	.488E+00				
.204	.509E+01	.439E+00				
.212	.527E+01	.488E+00				
.219	.454E+01	.454E+00				
.226	.405E+01	.453E+00				
.234	.341E+01	.419E+00				
.241	.262E+01	.374E+00				
.248	.236E+01	.377E+00				
.255	.316E+01	.514E+00				
.263	.269E+01	.485E+00				
.270	.146E+01	.328E+00				
.277	.154E+01	.360E+00				
.285	.190E+01	.470E+00				
.292	.118E+01	.317E+00				
.307	.142E+01	.504E+00				

Table 5.3 (continued)

$x_F = 0.125$						
$\sqrt{\tau}$	4000-Amp		2750-Amp		Average	
.182			.543E+01	.109E+01	.543E+01	.109E+01
.190			.867E+01	.173E+01	.867E+01	.173E+01
.197			.653E+01	.108E+01	.653E+01	.108E+01
.204	.469E+01	.427E+00	.617E+01	.928E+00	.495E+01	.388E+00
.212	.356E+01	.260E+00	.441E+01	.614E+00	.369E+01	.240E+00
.219	.339E+01	.242E+00	.402E+01	.523E+00	.350E+01	.219E+00
.226	.330E+01	.221E+00	.428E+01	.546E+00	.344E+01	.205E+00
.233	.315E+01	.197E+00	.388E+01	.483E+00	.326E+01	.182E+00
.277	.139E+01	.121E+00	.152E+01	.246E+00	.141E+01	.109E+00
.284	.123E+01	.114E+00	.119E+01	.210E+00	.122E+01	.100E+00
.292	.114E+01	.113E+00	.122E+01	.227E+00	.115E+01	.101E+00
.299	.815E+00	.849E−01	.812E+00	.212E+00	.815E+00	.788E−01
.307	.820E+00	.897E−01	.773E+00	.191E+00	.811E+00	.812E−01
.320	.641E+00	.456E−01	.677E+00	.105E+00	.647E+00	.418E−01
.344	.344E+00	.287E−01	.332E+00	.655E−01	.342E+00	.263E−01
.375	.202E+00	.234E−01	.162E+00	.495E−01	.195E+00	.212E−01
.401	.105E+00	.179E−01	.144E+00	.552E−01	.108E+00	.170E−01
.436	.333E−01	.106E−01			.333E−01	.106E−01
$\sqrt{\tau}$	NA3 ($\sqrt{s} = 27.4\,GeV$)					
.168	.107E+02	.535E+00				
.175	.929E+01	.487E+00				
.182	.913E+01	.512E+00				
.190	.675E+01	.450E+00				
.197	.614E+01	.441E+00				
.204	.492E+01	.404E+00				
.212	.488E+01	.410E+00				
.219	.454E+01	.432E+00				
.226	.381E+01	.405E+00				
.234	.288E+01	.341E+00				
.241	.345E+01	.431E+00				
.248	.289E+01	.409E+00				
.255	.182E+01	.312E+00				
.263	.220E+01	.411E−01				
.270	.150E+01	.308E+00				
.277	.206E+01	.439E+00				
.285	.133E+01	.318E+00				
.292	.148E+01	.384E+00				
.299	.110E+01	.397E+00				
.307	.107E+01	.344E+00				

Table 5.3 (continued)

$x_F = 0.175$						
$\sqrt{\tau}$	4000-Amp		2750-Amp		Average	
.205	.393E+01	.873E+00			.393E+01	.873E+00
.212	.328E+01	.488E+00	.472E+01	.163E+01	.340E+01	.468E+00
.219	.357E+01	.444E+00	.551E+01	.137E+01	.376E+01	.422E+00
.226	.288E+01	.315E+00	.230E+01	.574E+00	.275E+01	.276E+00
.233	.271E+01	.281E+00	.374E+01	.758E+00	.283E+01	.264E+00
.277	.129E+01	.150E+00	.220E+01	.475E+00	.137E+01	.143E+00
.284	.111E+01	.133E+00	.134E+01	.300E+00	.115E+01	.121E+00
.292	.846E+00	.105E+00	.110E+01	.249E+00	.884E+00	.969E−01
.299	.103E+01	.127E+00	.898E+00	.239E+00	.998E+00	.112E+00
.306	.792E+00	.102E+00	.675E+00	.191E+00	.766E+00	.900E−01
.320	.719E+00	.560E−01	.496E+00	.923E−01	.659E+00	.479E−01
.345	.317E+00	.307E−01	.244E+00	.578E−01	.301E+00	.271E−01
.374	.205E+00	.255E−01			.205E+00	.255E−01
.405	.114E+00	.207E−01			.114E+00	.207E−01
.435	.486E−01	.130E−01			.486E−01	.130E−01
$\sqrt{\tau}$	NA3 ($\sqrt{s} = 27.4\,GeV$)					
.168	.925E+01	.448E+00				
.175	.852E+01	.453E+00				
.182	.725E+01	.413E+00				
.190	.675E+01	.422E+00				
.197	.583E+01	.409E+00				
.204	.509E+01	.386E+00				
.212	.429E+01	.371E+00				
.219	.389E+01	.367E+00				
.226	.357E+01	.381E+00				
.234	.288E+01	.341E+00				
.241	.259E+01	.316E+00				
.248	.252E+01	.346E+00				
.255	.199E+01	.312E+00				
.263	.228E+01	.411E+00				
.270	.182E+01	.369E+00				
.277	.140E+01	.320E+00				
.285	.997E+00	.247E+00				
.292	.108E+01	.292E+00				
.299	.187E+01	.480E+00				
.307	.130E+01	.385E+00				

Table 5.3 (continued)

$x_F = 0.225$						
$\sqrt{\tau}$	4000-Amp		2750-Amp		Average	
.233	.310E+01	.112E+01			.310E+01	.112E+01
.277	.103E+01	.203E+00			.103E+01	.203E+00
.284	.101E+01	.185E+00	.123E+01	.425E+00	.105E+01	.169E+00
.292	.917E+00	.168E+00	.843E+00	.322E+00	.901E+00	.149E+00
.299	.793E+00	.149E+00	.132E+01	.424E+00	.851E+00	.140E+00
.307	.922E+00	.158E+00	.603E+00	.214E+00	.810E+00	.127E+00
.321	.658E+00	.708E−01	.412E+00	.110E+00	.586E+00	.596E−01
.344	.376E+00	.404E−01	.308E+00	.805E−01	.362E+00	.361E−01
.372	.220E+00	.303E−01	.272E+00	.777E−01	.227E+00	.282E−01
.402	.909E−01	.196E−01			.909E−01	.196E−01
.429	.424E−01	.128E−01			.424E−01	.128E−01
$\sqrt{\tau}$	NA3 ($\sqrt{s} = 27.4\,GeV$)					
.168	.847E+01	.438E+00				
.175	.785E+01	.431E+00				
.182	.600E+01	.363E+00				
.190	.619E+01	.408E+00				
.197	.567E+01	.425E+00				
.204	.492E+01	.386E+00				
.212	.488E+01	.410E+00				
.219	.346E+01	.346E+00				
.226	.381E+01	.405E+00				
.234	.367E+01	.419E+00				
.241	.256E+01	.316E+00				
.248	.220E+01	.314E+00				
.255	.271E+01	.446E+00				
.263	.194E+01	.336E+00				
.270	.142E+01	.276E+00				
.277	.189E+01	.382E+00				
.285	.949E+00	.261E+00				
.292	.108E+01	.276E+00				
.299	.717E+00	.215E+00				
.307	.107E+01	.350E+00				

Table 5.3 (continued)

$x_F = 0.275$					
$\sqrt{\tau}$	4000-Amp		2750-Amp		Average
.300	.946E+00	.371E+00			.946E+00 .371E+00
.306	.531E+00	.175E+00			.531E+00 .175E+00
.321	.370E+00	.742E−01			.370E+00 .742E−01
.346	.246E+00	.434E−01	.403E+00	.143E+00	.259E+00 .415E−01
.373	.144E+00	.307E−01			.144E+00 .307E−01
.403	.122E+00	.275E−01			.122E+00 .275E−01
.432	.364E−01	.138E−01			.364E−01 .138E−01
$\sqrt{\tau}$	NA3 ($\sqrt{s} = 27.4\,GeV$)				
.168	.788E+01	.448E+00			
.175	.730E+01	.442E+00			
.182	.625E+01	.413E+00			
.190	.576E+01	.408E+00			
.197	.504E+01	.394E+00			
.204	.404E+01	.351E+00			
.212	.410E+01	.390E+00			
.219	.346E+01	.346E+00			
.226	.310E+01	.334E+00			
.234	.288E+01	.341E+00			
.241	.259E+01	.345E+00			
.248	.214E+01	.314E+00			
.255	.161E+01	.278E+00			
.263	.205E+01	.362E+00			
.270	.207E+01	.405E+00			
.277	.198E+01	.408E+00			
.285	.104E+01	.275E+00			
.292	.118E+01	.343E+00			
.299	.105E+01	.298E+00			
.307	.830E+00	.267E+00			

Table 5.4: $E\frac{d^3\sigma}{dp^3}$ *versus* p_t for different mass bins. The first number is the cross-section and the second is the error. Units are *pbarn/GeV^2/nucleon* for the cross-section, and *GeV* for p_t. A continuum subtraction was made for the Upsilons as explained in the text.

$7 < m < 8\ (GeV)$						
p_t	4000-*Amp*		2750-*Amp*		Average	
0.10			.844E+00	.123E+00	.844E+00	.123E+00
0.30			.105E+01	.925E−01	.105E+01	.925E−01
0.50			.887E+00	.662E−01	.887E+00	.662E−01
0.70			.866E+00	.613E−01	.866E+00	.613E−01
0.90			.612E+00	.453E−01	.612E+00	.453E−01
1.10			.577E+00	.480E−01	.577E+00	.480E−01
1.30			.417E+00	.419E−01	.417E+00	.419E−01
1.50			.335E+00	.409E−01	.335E+00	.409E−01
1.70			.247E+00	.401E−01	.247E+00	.401E−01
1.90			.147E+00	.330E−01	.147E+00	.330E−01
2.10			.147E+00	.466E−01	.147E+00	.466E−01
$8 < m < 9\ (GeV)$						
p_t	4000-*Amp*		2750-*Amp*		Average	
0.10	.334E+00	.285E−01	.356E+00	.524E−01	.339E+00	.250E−01
0.30	.427E+00	.225E−01	.521E+00	.477E−01	.444E+00	.204E−01
0.50	.352E+00	.154E−01	.469E+00	.342E−01	.372E+00	.141E−01
0.70	.365E+00	.158E−01	.410E+00	.288E−01	.376E+00	.138E−01
0.90	.254E+00	.115E−01	.293E+00	.209E−01	.263E+00	.101E−01
1.10	.223E+00	.114E−01	.242E+00	.174E−01	.229E+00	.954E−02
1.30	.180E+00	.113E−01	.194E+00	.158E−01	.185E+00	.918E−02
1.50	.130E+00	.107E−01	.141E+00	.130E−01	.134E+00	.827E−02
1.70	.930E−01	.990E−02	.888E−01	.100E−01	.909E−01	.704E−02
1.90	.692E−01	.109E−01	.782E−01	.986E−02	.742E−01	.732E−02
2.10	.434E−01	.105E−01	.548E−01	.852E−02	.503E−01	.662E−02
2.30			.293E−01	.583E−02	.293E−01	.583E−02
2.50			.234E−01	.553E−02	.234E−01	.553E−02
2.70			.197E−01	.614E−02	.197E−01	.614E−02

Table 5.4 (continued)

Upsilons						
0.10	.184E+00	.127E−01	.187E+00	.286E−01		
0.30	.211E+00	.915E−02	.273E+00	.237E−01		
0.50	.190E+00	.697E−02	.205E+00	.168E−01		
0.70	.174E+00	.574E−02	.215E+00	.145E−01		
0.90	.161E+00	.506E−02	.188E+00	.124E−01		
1.10	.136E+00	.439E−02	.157E+00	.109E−01		
1.30	.103E+00	.373E−02	.127E+00	.883E−02		
1.50	.914E−01	.363E−02	.957E−01	.786E−02		
1.70	.642E−01	.312E−02	.793E−01	.687E−02		
1.90	.588E−01	.321E−02	.646E−01	.652E−02		
2.10	.404E−01	.283E−02	.480E−01	.562E−02		
2.30	.306E−01	.286E−02	.340E−01	.461E−02		
2.50	.297E−01	.346E−02	.237E−01	.402E−02		
2.70	.204E−01	.366E−02	.176E−01	.355E−02		
2.90	.928E−02	.330E−02	.918E−02	.232E−02		
3.10	.217E−01	.986E−02	.133E−01	.376E−02		
3.30	.323E−02	.154E−02	.604E−02	.240E−02		
3.50	.224E−02	.211E−02	.519E−02	.216E−02		
3.70	.437E−02	.503E−02	.159E−02	.157E−02		
3.90			.265E−02	.149E−02		

$10.5 < m < 11.5 \ (GeV)$						
p_t	4000-Amp		2750-Amp		Average	
0.10	.719E−01	.997E−02	.705E−01	.167E−01	.715E−01	.857E−02
0.30	.787E−01	.631E−02	.830E−01	.125E−01	.796E−01	.563E−02
0.50	.684E−01	.451E−02	.914E−01	.109E−01	.718E−01	.417E−02
0.70	.619E−01	.370E−02	.691E−01	.795E−02	.632E−01	.336E−02
0.90	.507E−01	.303E−02	.524E−01	.587E−02	.511E−01	.269E−02
1.10	.403E−01	.237E−02	.374E−01	.456E−02	.397E−01	.210E−02
1.30	.311E−01	.197E−02	.341E−01	.421E−02	.316E−01	.179E−02
1.50	.240E−01	.171E−02	.231E−01	.338E−02	.238E−01	.152E−02
1.70	.151E−01	.117E−02	.143E−01	.241E−02	.149E−01	.105E−02
1.90	.129E−01	.116E−02	.153E−01	.288E−02	.132E−01	.107E−02
2.10	.672E−02	.768E−03	.101E−01	.220E−02	.708E−02	.725E−03
2.30	.472E−02	.645E−03	.765E−02	.192E−02	.502E−02	.612E−03
2.50	.450E−02	.685E−03	.540E−02	.159E−02	.464E−02	.629E−03
2.70	.329E−02	.667E−03	.356E−02	.133E−02	.334E−02	.596E−03
2.90	.215E−02	.493E−03			.215E−02	.493E−03
3.10	.159E−02	.524E−03			.159E−02	.524E−03

Table 5.4 (continued)

$10.5 < m < 11.5\ (GeV)$						
p_t	4000-Amp		2750-Amp		Average	
0.10	.568E—01	.765E—02	.393E—01	.127E—01	.522E—01	.655E—02
0.30	.695E—01	.530E—02	.652E—01	.120E—01	.688E—01	.485E—02
0.50	.635E—01	.416E—02	.762E—01	.112E—01	.651E—01	.390E—02
0.70	.510E—01	.291E—02	.438E—01	.660E—02	.499E—01	.267E—02
0.90	.449E—01	.250E—02	.337E—01	.488E—02	.425E—01	.223E—02
1.10	.335E—01	.195E—02	.291E—01	.437E—02	.328E—01	.178E—02
1.30	.260E—01	.164E—02	.214E—01	.343E—02	.251E—01	.148E—02
1.50	.197E—01	.130E—02	.193E—01	.316E—02	.196E—01	.120E—02
1.70	.141E—01	.108E—02	.125E—01	.246E—02	.139E—01	.988E—03
1.90	.846E—02	.776E—03	.110E—01	.235E—02	.871E—02	.737E—03
2.10	.680E—02	.685E—03	.723E—02	.183E—02	.685E—02	.642E—03
2.30	.440E—02	.550E—03			.440E—02	.550E—03
2.50	.334E—02	.483E—03			.334E—02	.483E—03
2.70	.262E—02	.420E—03			.262E—02	.420E—03
2.90	.164E—02	.330E—03			.164E—02	.330E—03
3.10	.120E—02	.284E—03			.120E—02	.284E—03
3.30	.111E—02	.298E—03			.111E—02	.298E—03
3.50	.654E—03	.243E—03			.654E—03	.243E—03

$10.5 < m < 11.5\ (GeV)$						
p_t	4000-Amp		2750-Amp		Average	
0.10	.240E—01	.546E—02			.240E—01	.546E—02
0.30	.206E—01	.290E—02			.206E—01	.290E—02
0.50	.188E—01	.213E—02			.188E—01	.213E—02
0.70	.171E—01	.172E—02			.171E—01	.172E—02
0.90	.972E—02	.116E—02			.972E—02	.116E—02
1.10	.107E—01	.109E—02			.107E—01	.109E—02
1.30	.791E—02	.879E—03			.791E—02	.879E—03
1.50	.605E—02	.697E—03			.605E—02	.697E—03
1.70	.350E—02	.509E—03			.350E—02	.509E—03
1.90	.194E—02	.359E—03			.194E—02	.359E—03
2.10	.200E—02	.366E—03			.200E—02	.366E—03
2.30	.136E—02	.294E—03			.136E—02	.294E—03
2.50	.136E—02	.288E—03			.136E—02	.288E—03
2.70	.600E—03	.191E—03			.600E—03	.191E—03
2.90	.435E—03	.166E—03			.435E—03	.166E—03

Table 5.5: Fit parameters of the p_t distributions. Note that the mean p_t is almost mass independent (excluding the Upsilons). A continuum subtraction was made in the Upsilon region as explained in the text.

Data set	Mass Range (GeV)	A (pbarn/GeV²)	p_0 (GeV)	$\langle p_t \rangle$ (GeV)
4000-Amp	7-8			
	8-9	.421 ± .012	3.22 ± .08	1.38 ± .03
	Upsilons	.216 ± .003	3.73 ± .04	1.60 ± .02
	10.5-11.5	.083 ± .003	3.04 ± .05	1.31 ± .02
	11.5-13.5	.071 ± .002	3.04 ± .04	1.31 ± .02
	13.5-18	.021 ± .001	2.95 ± .08	1.27 ± .03
2750-Amp	7-8	1.04 ± .05	3.22 ± .12	1.38 ± .05
	8-9	.510 ± .021	3.03 ± .07	1.30 ± .03
	Upsilons	.258 ± .006	3.61 ± .05	1.55 ± .02
	10.5-11.5	.087 ± .006	3.10 ± .11	1.33 ± .05
	11.5-13.5	.058 ± .005	3.21 ± .17	1.38 ± .08
	13.5-18			
Average	7-8	1.04 ± .05	3.22 ± .12	1.38 ± .05
	8-9	.440 ± .010	3.17 ± .05	1.36 ± .02
	Upsilons			
	10.5-11.5	.084 ± .003	3.04 ± .04	1.31 ± .02
	11.5-13.5	.069 ± .002	3.07 ± .04	1.32 ± .02
	13.5-18	.021 ± .001	2.95 ± .08	1.27 ± .03

~ 1.33

Table 5.6: Upsilon production cross-section times branching ratio to muon pairs in *pbarn/nucleon*. The first error is statistical and the second error is an estimate of the systematic error due to the fitting procedure.

Resonance	x_F	4000-Amp	2750-Amp
Υ	-.125	$2.89 \pm .13 \pm .53$	$2.47 \pm .25 \pm 1.24$
	-.075	$2.90 \pm .10 \pm .36$	$3.46 \pm .20 \pm .81$
	-.025	$2.87 \pm .08 \pm .28$	$3.53 \pm .16 \pm .52$
	.025	$3.10 \pm .07 \pm .27$	$3.35 \pm .14 \pm .55$
	.075	$2.82 \pm .07 \pm .27$	$3.39 \pm .15 \pm .60$
	.125	$2.87 \pm .08 \pm .32$	$3.20 \pm .17 \pm .69$
	.175	$2.99 \pm .12 \pm .42$	$3.31 \pm .27 \pm 1.11$
	.225	$2.51 \pm .29 \pm 1.24$	
Υ'	-.125	$.685 \pm .050 \pm .232$	$.961 \pm .153 \pm .695$
	-.075	$.829 \pm .043 \pm .143$	$.792 \pm .092 \pm .536$
	-.025	$.869 \pm .036 \pm .153$	$.880 \pm .076 \pm .369$
	.025	$.860 \pm .034 \pm .156$	$.917 \pm .071 \pm .406$
	.075	$.735 \pm .031 \pm .142$	$.961 \pm .076 \pm .376$
	.125	$.765 \pm .036 \pm .165$	$1.033 \pm .092 \pm .560$
	.175	$.808 \pm .052 \pm .210$	$.902 \pm .116 \pm .606$
	.225	$.660 \pm .094 \pm .433$	
Υ''	-.125	$.462 \pm .042 \pm .122$	$.215 \pm .061 \pm .372$
	-.075	$.291 \pm .023 \pm .112$	$.436 \pm .070 \pm .864$
	-.025	$.357 \pm .022 \pm .074$	$.467 \pm .057 \pm .383$
	.025	$.444 \pm .023 \pm .106$	$.539 \pm .056 \pm .243$
	.075	$.380 \pm .021 \pm .111$	$.458 \pm .050 \pm .201$
	.125	$.389 \pm .025 \pm .132$	$.537 \pm .065 \pm .361$
	.175	$.486 \pm .040 \pm .165$	$.423 \pm .074 \pm .332$
	.225	$.253 \pm .045 \pm .225$	

Table 5.7: Relative production ratios of Υ' to Υ and Υ'' to Υ. R_Υ is the Υ to continuum ratio defined in the text. The first error is statistical and the second error is an estimate of the systematic error due to the fitting procedure.

Ratio	x_F	4000-Amp	2750-Amp
$\frac{\Upsilon'}{\Upsilon}$	-.125	$.237 \pm .020 \pm .031$	$.389 \pm .073 \pm .057$
	-.075	$.286 \pm .017 \pm .012$	$.229 \pm .030 \pm .082$
	-.025	$.303 \pm .015 \pm .021$	$.249 \pm .024 \pm .059$
	.025	$.277 \pm .013 \pm .024$	$.273 \pm .024 \pm .065$
	.075	$.261 \pm .013 \pm .023$	$.283 \pm .026 \pm .051$
	.125	$.266 \pm .015 \pm .025$	$.323 \pm .034 \pm .087$
	.175	$.270 \pm .021 \pm .028$	$.273 \pm .042 \pm .069$
	.225	$.263 \pm .048 \pm .029$	
$\frac{\Upsilon''}{\Upsilon}$	-.125	$.160 \pm .016 \pm .011$	$.087 \pm .026 \pm .071$
	-.075	$.100 \pm .009 \pm .023$	$.126 \pm .022 \pm .179$
	-.025	$.124 \pm .008 \pm .012$	$.132 \pm .017 \pm .078$
	.025	$.143 \pm .008 \pm .020$	$.161 \pm .018 \pm .040$
	.075	$.135 \pm .008 \pm .024$	$.135 \pm .016 \pm .030$
	.125	$.135 \pm .009 \pm .028$	$.168 \pm .022 \pm .063$
	.175	$.162 \pm .015 \pm .028$	$.128 \pm .025 \pm .043$
	.225	$.101 \pm .022 \pm .027$	
$R_\Upsilon\,(GeV)$	-.125	$1.81 \pm .45 \pm .64$	$1.05 \pm .44 \pm .85$
	-.075	$1.34 \pm .22 \pm .29$	$1.52 \pm .50 \pm .96$
	-.025	$1.38 \pm .18 \pm .23$	$1.42 \pm .36 \pm .53$
	.025	$1.55 \pm .19 \pm .25$	$1.55 \pm .37 \pm .54$
	.075	$1.35 \pm .16 \pm .24$	$1.27 \pm .29 \pm .43$
	.125	$1.33 \pm .18 \pm .27$	$1.36 \pm .36 \pm .64$
	.175	$1.69 \pm .35 \pm .46$	$1.32 \pm .56 \pm .82$
	.225	$.909 \pm .424 \pm .753$	